Summer 2014

The prediction of airborne and structure-borne noise potential for a tire

Nicholas Sakamoto
Purdue University

Graduate School ETD Form 9
(Revised 01/14)

PURDUE UNIVERSITY
GRADUATE SCHOOL
Thesis/Dissertation Acceptance

This is to certify that the thesis/dissertation prepared

By Nicholas Sakamoto

Entitled

THE PREDICTION OF AIRBORNE AND STRUCTURE-BORNE NOISE POTENTIAL FOR A TIRE

For the degree of Master of Science in Mechanical Engineering

Is approved by the final examining committee:

J. Stuart Bolton

Charles M. Krousgrill

Garrett Jeong

To the best of my knowledge and as understood by the student in the *Thesis/Dissertation Agreement. Publication Delay, and Certification/Disclaimer (Graduate School Form 32)*, this thesis/dissertation adheres to the provisions of Purdue University's "Policy on Integrity in Research" and the use of copyrighted material.

J. Stuart Bolton

Approved by Major Professor(s): _____

Approved by: David Anderson 07/23/2014

Head of the Department Graduate Program Date

THE PREDICTION OF AIRBORNE AND STRUCTURE-BORNE NOISE POTENTIAL FOR A TIRE

A Thesis

Submitted to the Faculty

of

Purdue University

by

Nicholas Y. Sakamoto

In Partial Fulfillment of the

Requirements for the Degree

of

Master of Science in Mechanical Engineering

August 2014

Purdue University

West Lafayette, Indiana

To my wife, Elizabeth.

ACKNOWLEDGMENTS

The completion of my Masters degree was made possible by the support of mentors, colleagues, friends, and family. Thanks to Professor J. Stuart Bolton for his guidance and collaboration concerning my research and for the enjoyable conversations over coffee. Thanks also to Professor Patricia Davies for her signal processing discussions and for providing leadership opportunities at Herrick Laboratories. The staff at Herrick Laboratories, Bob Brown, Frank Lee, Ron Evans, and Donna Cackley, deserve my gratitude for all their technical and clerical support. Special thanks to my wife, Elizabeth Sakamoto, who came across the country for my pursuit of higher education and provided unmatched love and support. Thanks to my parents, Richard and Jennifer Sakamoto, for their encouragement in all my studies. Thanks also to Dale and Luke Sakamoto for being the best brothers I could ask for. Thanks to my in-laws, Daryll and Ceci, for their support. I also would like to thank Professor Masahiro Toyoda for his hospitality and expertise during my fellowship in Japan. Many thanks to my fellow graduate students at Herrick Laboratories for their support and friendship. Thanks especially to Andrew McMullen, Brandon Sobecki, Michael Hayward, Andrew Jessop, and Jelena Paripovic.

TABLE OF CONTENTS

Page

LIST OF TABLES vii

LIST OF FIGURES viii

ABSTRACT xiv

1. INTRODUCTION 1
   1.1 Tire/Road Interaction Noise 1
      1.1.1 Impact of Tire Noise 1
      1.1.2 Tire/Road Interaction Noise Generation 1
   1.2 Problem Statement 3
   1.3 Overview 3

2. NOISE RADIATION AND VIBRATION OF A RADIAL TIRE 5
   2.1 Introduction 5
   2.2 Measurement of Noise Radiation 5
      2.2.1 Tire Pavement Test Apparatus 5
         2.2.1.1 Hemi-Anechoic Chamber 6
         2.2.1.2 Pavement Samples 6
         2.2.1.3 Tires Tested 6
         2.2.1.4 Background Noise Reduction 11
      2.2.2 On-Board Sound Intensity 11
      2.2.3 Vibration Testing 14
      2.2.4 Magnetic Triggering System 17
      2.2.5 Speed Variation 20
   2.3 Signal Processing 20
      2.3.1 Trigger Signals 20
      2.3.2 Sound Intensity Data Processing 20
      2.3.3 Accelerometer Data Processing 22
      2.3.4 Pavement Averaging 22
   2.4 Results and Analysis 24
      2.4.1 OBSI Measurements 24
         2.4.1.1 Sample Set, Full Speed 24
         2.4.1.2 Tire 7, Varying Speed 24
      2.4.2 Accelerometer Measurements 27
         2.4.2.1 Sample Set, Full Speed 27
         2.4.2.2 Tire 7, Varying Speed 31
   2.5 Summary of Noise Radiation and Vibration of a Radial Tire 36

Page

3. STRUCTURAL WAVE PROPAGATION ON A RADIAL TIRE 37
3.1 Introduction 37
3.2 Measurement of Structural Wave Propagation 37
3.2.1 Stationary Tire Test 37
3.2.1.1 Laser Vibrometer 38
3.2.1.2 Point Excitation 38
3.2.1.3 Patch Excitation 43
3.3 Signal Processing 44
3.3.1 Wavenumber Decomposition 44
3.3.2 Vibration Potential Data Processing 44
3.3.3 Airborne Potential Data Processing 46
3.4 Results and Analysis 46
3.4.1 Circumferential Spectral Plots 46
3.4.2 Wavenumber Decomposition Plots 48
3.4.3 Vibration Potential 54
3.4.3.1 Spectral Analysis 54
3.4.3.2 Overall Level Analysis 56
3.4.4 Airborne Potential 59
3.4.4.1 Spectral Analysis 59
3.4.5 Overall Level Analysis 61
3.5 Summary of Structural Wave Propagation 63

4. MOVING INPUT FUNCTION 64
4.1 Introduction 64
4.2 Theory 65
4.3 Experimental Analysis 69
4.4 Theoretical Analysis 72
4.5 Summary of Moving Input Function 82

5. RELATIVE TIRE NOISE POTENTIAL MODEL 83
5.1 Introduction 83
5.2 Tires Tested 83
5.3 Procedure 85
5.4 Results and Analysis 88
5.4.1 Airborne Potential 88
5.4.1.1 Spectral Analysis 88
5.4.1.2 Overall Level Analysis 89
5.4.2 Vibration Potential 93
5.4.2.1 Spectral Analysis 93
5.4.2.2 Overall Level Analysis 93
5.5 TPTA Experimental Results 98
5.5.1 On-Board Sound Intensity Results and Analysis 99
5.5.2 Accelerometer Results and Analysis 99

Page
5.5.3 Acoustic Mode Noise Reduction 109
5.6 Summary of Relative Tire Noise Potential Model 110

6. CONCLUSIONS AND RECOMMENDATIONS FOR FUTURE WORK 113
6.1 Conclusions 113
6.2 Future Work 115

LIST OF REFERENCES 116

APPENDICES 118

A. ADDITIONAL PLOTS: NOISE RADIATION AND VIBRATION OF A RADIAL TIRE 118

B. ADDITIONAL PLOTS: STRUCTURAL WAVE PROPAGATION ON A RADIAL TIRE 128

C. ADDITIONAL PLOTS: RELATIVE TIRE NOISE POTENTIAL MODEL 150

VITA 165

LIST OF TABLES

Table		Page
2.1	List of Tires Tested.	10
2.2	Overall sound intensity level of each tire for the defined spectra.	25
2.3	Overall structure-borne noise level of each tire for the defined spectra.	31
3.1	Vibration noise potential level of each tire for the defined spectra from point excitation force.	56
3.2	Vibration noise potential level of each tire for the defined spectra from patch excitation force.	58
3.3	Airborne noise potential level of each tire for the defined spectra from point excitation force.	61
3.4	Airborne noise potential level of each tire for the defined spectra from patch excitation force.	63
4.1	Spatial input values windowed by the contact patch.	67
5.1	List of Tires Tested.	84
C.1	Tire A-weighted Airborne Noise Ranks.	150
C.2	Tire A-weighted Structure-borne Noise Ranks.	150

LIST OF FIGURES

Figure		Page
2.1	Tire pavement test apparatus (TPTA) in hemi-anechoic chamber.	7
2.2	Concrete pavement samples on the TPTA.	8
2.3	OBSI without background noise reducing measures.	12
2.4	Per pavement coherence for all 8 tires.	13
2.5	Intensity spectrum with noise floor measurement.	14
2.6	Triaxial accelerometer at hub without tire installed.	15
2.7	Normal acceleration (Z-axis) averaged over the five pavements for each tire compared with an unloaded tire's measurements.	16
2.8	Magnetic trigger on arm opposite of the OBSI and triaxial accelerometer.	18
2.9	Top: 1 TPTA revolution ($\approx$1 second for 30 mph) time history. Middle: 1 pavement sample time history. Bottom: 80 ms window for averaging. Black = Normal acceleration (1 m/s^2), Red = Trigger Signal (Volts).	19
2.10	Two sections of the trigger signal with a 95% reference line overlaid.	21
2.11	Per pavement normal acceleration (Z-axis) data for one tire.	23
2.12	Averaged sound intensity level for eight tires.	25
2.13	Averaged sound intensity level at different speeds for tire 7.	26
2.14	Overall sound intensity level at different speeds for tire 7.	27
2.15	Acceleration in the tire's direction of travel (X-axis) for eight tires.	28
2.16	Out-of-plane acceleration (Y-axis) for eight tires.	29
2.17	Normal acceleration (Z-axis) for eight tires.	30
2.18	Acceleration in the tire's direction of travel (X-axis) for tire 7 at various speeds.	32
2.19	Out-of-plane acceleration (Y-axis) for tire 7 at various speeds.	33
2.20	Normal acceleration (Z-axis) for 8 tires.	34
2.21	Overall acceleration levels at different speeds for tire 7 (square = X-axis, plus = Y-axis, circle = Z-axis).	35

Figure		Page
3.1	Tire stand without a tire mounted.	39
3.2	Stationary tire test in action.	40
3.3	Tire before adding the Magnaflux Spotcheck Developer SKD-S2 (left half) and after (right half).	41
3.4	Point excitation set-up for the stationary tire test.	42
3.5	Patch excitation set-up for the stationary tire test.	43
3.6	The first four circumferential modes of a tire.	45
3.7	Circumferential spectral plot for Tire 8.	47
3.8	Circumferential spectral plot for Tire 8 from patch excitation.	49
3.9	Frequency-wavenumber plot for Tire 8 (White = Speed of Sound (340 m/s slope), Pink = 60 m/s phase speed).	50
3.10	Frequency-wavenumber plot for Tire 8 from patch excitation.	51
3.11	First acoustic mode for Tire 8 from patch excitation.	52
3.12	Air space duct mode for Tire 8 from patch excitation.	53
3.13	Structure-borne noise potential for the eight tires.	54
3.14	Structure-borne noise potential for the three tires from patch excitation.	55
3.15	Comparison of the ranks between the two experiments.	57
3.16	Airborne noise potential for the eight tires.	59
3.17	Airborne noise potential for three tires from patch excitation.	60
3.18	Comparison of the ranks between the two experiments.	62
4.1	Δx section of tire tread.	65
4.2	Footprint for tire 7 with outline of spatial window.	66
4.3	Spatial point 500 amplitude change through time.	68
4.4	Reconstructed tire tread pattern in MATLAB.	70
4.5	Frequency-wavenumber plot from moving input tread force.	71
4.6	Moving input force vibration potential spectrum.	73
4.7	Moving input force vibration potential spectrum.	74
4.8	Moving input force airborne noise potential spectrum.	75
4.9	Airborne spectrum level vs. speed for Tire 7 using the moving input.	76

Figure Page

4.10 Periodic tread pattern (top) and random tread pattern (bottom). . . . 77

4.11 Frequency-wavenumber plot for the periodic tread pattern. 78

4.12 Frequency-wavenumber plot for the random tread pattern. 79

4.13 Moving input force vibration potential spectra for two theoretical tread patterns. 80

4.14 Moving input force airborne potential spectra for two theoretical tread patterns. 81

5.1 Full spectrum third-octave noise measurements from the interior of a car of 5 tires. 85

5.2 Structure-borne narrow band noise measurements from the interior of a car of 5 tires. 86

5.3 New test stand for conducting laser vibrometer measurements with the patch excitation method. 87

5.4 Airborne noise potential for five tires from patch excitation. 89

5.5 Airborne noise potential for five tires from patch excitation modified by the moving input function at 80 kph. 90

5.6 Overall airborne noise level comparison between experimental data and prediction (without moving input). 91

5.7 Overall airborne noise level comparison between experimental data and prediction (with moving input). 91

5.8 Overall airborne noise level comparison between experimental data and prediction. 92

5.9 Structure-borne noise potential for five tires from patch excitation. . . 94

5.10 Acoustic mode analysis from the structure-borne noise results from the automobile OEM (left) and structure-borne noise potential for five tires from patch excitation (right). 95

5.11 Structure-borne noise potential for five tires from patch excitation modified by the moving input function at 80 kph. 96

5.12 Structure-borne narrow band noise measurements from the interior of a car of 5 tires. 97

5.13 Overall structure-borne noise level comparison between experimental data and prediction without moving input method. 98

Figure Page

5.14 Overall structure-borne noise level comparison between experimental data and prediction with moving input method. 98

5.15 The coherence per pavement for the five tires tested. 100

5.16 Averaged sound intensity level for the five tires. 101

5.17 Overall airborne noise level comparison between automobile OEM experimental data and TPTA results. 101

5.18 Airborne noise potential for five tires from patch excitation modified by the moving input function at 30 mph. 102

5.19 Overall airborne noise level comparison between TPTA results and prediction with the moving input method. 102

5.20 Acceleration in the tire's direction of travel (X-axis) for the five tires. 103

5.21 Out-of-plane acceleration (Y-axis) for the five tires. 104

5.22 Normal acceleration (Z-axis) for the five tires. 105

5.23 Overall airborne noise level comparison between automobile OEM experimental data and TPTA results. 106

5.24 Overall airborne noise level comparison between automobile OEM experimental data and TPTA results. 106

5.25 Structure-borne noise potential for five tires from patch excitation modified by the moving input function at 30 mph. 107

5.26 Overall airborne noise level comparison between TPTA results and prediction with the moving input method. 108

5.27 Tire 5 with glass fiber chemically attached to the inside diameter of the carcass. 109

5.28 Averaged sound intensity level for tire 5 with and without the glass fiber. 110

5.29 Normal acceleration (Z-axis) for tire 5 with and without the glass fiber. 111

A.1 Acceleration in the tire's direction of travel (X-axis) averaged over the 5 pavements for each tire compared with an unloaded tire's measurements. 118

A.2 Out-of-plane acceleration (Y-axis) averaged over the 5 pavements for each tire compared with an unloaded tire's measurements. 119

A.3 Sound intensity level for each tire per pavement sample. 120

A.4 Sound intensity level for Tire 7 per pavement sample for a range of speeds. 121

Figure Page

A.5 Acceleration in the tire's direction of travel (X-axis) recorded for each tire per pavement. 122

A.6 Out-of-plane acceleration (Y-axis) recorded for each tire per pavement. 123

A.7 Normal acceleration (Z-axis) recorded for each tire per pavement. . . 124

A.8 Acceleration in the tire's direction of travel (X-axis) for Tire 7 per pavement sample for a range of speeds. 125

A.9 Out of plane acceleration (Y-axis) for Tire 7 per pavement sample for a range of speeds. 126

A.10 Normal acceleration (Z-axis) for Tire 7 per pavement sample for a range of speeds. 127

B.1 Circumferential spectral plot for Tire 1. 128

B.2 Circumferential spectral plot for Tire 2. 129

B.3 Circumferential spectral plot for Tire 3. 130

B.4 Circumferential spectral plot for Tire 4. 131

B.5 Circumferential spectral plot for Tire 5. 132

B.6 Circumferential spectral plot for Tire 6. 133

B.7 Circumferential spectral plot for Tire 7. 134

B.8 Circumferential spectral plot for Tire 8. 135

B.9 Circumferential spectral plot for Tire 5 from patch excitation. 136

B.10 Circumferential spectral plot for Tire 7 from patch excitation. 137

B.11 Circumferential spectral plot for Tire 8 from patch excitation. 138

B.12 Frequency-wavenumber plot for Tire 1. 139

B.13 Frequency-wavenumber plot for Tire 2. 140

B.14 Frequency-wavenumber plot for Tire 3. 141

B.15 Frequency-wavenumber plot for Tire 4. 142

B.16 Frequency-wavenumber plot for Tire 5. 143

B.17 Frequency-wavenumber plot for Tire 6. 144

B.18 Frequency-wavenumber plot for Tire 7. 145

B.19 Frequency-wavenumber plot for Tire 8. 146

Figure Page

B.20 Frequency-wavenumber plot for Tire 5 from patch excitation. 147

B.21 Frequency-wavenumber plot for Tire 7 from patch excitation. 148

B.22 Frequency-wavenumber plot for Tire 8 from patch excitation. 149

C.1 Circumferential spectral plot for Tire 9. 151

C.2 Circumferential spectral plot for Tire 10. 152

C.3 Circumferential spectral plot for Tire 11. 153

C.4 Circumferential spectral plot for Tire 12. 154

C.5 Circumferential spectral plot for Tire 13. 155

C.6 Frequency-wavenumber plot for Tire 9. 156

C.7 Frequency-wavenumber plot for Tire 10. 157

C.8 Frequency-wavenumber plot for Tire 11. 158

C.9 Frequency-wavenumber plot for Tire 12. 159

C.10 Frequency-wavenumber plot for Tire 13. 160

C.11 Sound intensity level for each tire per pavement sample. 161

C.12 Acceleration in the tire's direction of travel (X-axis) recorded for each tire per pavement. 162

C.13 Out-of-plane acceleration (Y-axis) recorded for each tire per pavement. 163

C.14 Normal acceleration (Z-axis) recorded for each tire per pavement. . . 164

ABSTRACT

Sakamoto, Nicholas Y. MSME, Purdue University, August 2014. The Prediction of Airborne and Structure-borne Noise Potential for a Tire. Major Professor: J. Stuart Bolton, School of Mechanical Engineering.

Tire/pavement interaction noise is a major component of both exterior pass-by noise and vehicle interior noise. The current testing methods for ranking tires from loud to quiet require expensive equipment, multiple tires, and/or long experimental set-up and run times. If a laboratory based off-vehicle test could be used to identify the airborne and structure-borne potential of a tire from its dynamic characteristics, a relative ranking of a large group of tires could be performed at relatively modest expense. This would provide a smaller sample set of tires for follow-up testing and thus save expense for automobile OEMs. The focus of this research was identifying key noise features from a tire/pavement experiment. These results were compared against a stationary tire test in which the natural response of the tire to a forced input was measured. Since speed was identified as having some effect on the noise, an input function was also developed to allow the tires to be ranked at an appropriate speed. A relative noise model was used on a second sample set of tires to verify if the ranking could be used against interior vehicle measurements. While overall level analysis of the specified spectrum had mixed success, important noise generating features were identified, and the methods used could be improved to develop a standard off-vehicle test to predict a tire's noise potential.

1. INTRODUCTION

1.1 Tire/Road Interaction Noise

1.1.1 Impact of Tire Noise

Road traffic noise contributes significantly to modern day noise pollution. Proximity to major roads can impair a person's daily activities and disrupt restful sleep [1]. Adverse health effects, such as hypertension, have been shown to correlate to noise exposure [2]. Advances in reducing noise propagation from an automobile's engine and exhaust systems have made the tire/road interaction noise a more noticeable source. The contribution of tire/road noise affects both pass-by noise levels and automobile occupants' comfort. An understanding of the noise generating mechanisms of the tire/road interaction would provide insight for tire selection to reduce the structure-borne and airborne noise. Thus, the exterior and interior levels could be lowered to satisfy pass-by regulations and decrease the noise floor for a driver and passengers.

1.1.2 Tire/Road Interaction Noise Generation

Tire/road noise generation has been researched with a variety of methods for many years. Experimental studies with hundreds of tires of all shapes and sizes that were tested for different factors have been compiled into a book by Sandberg and Ejsmont [3]. Topics ranging from contribution of pavement surfaces to speed variations as well as statistical analysis of physical attributes all help to identify characteristics of tire/road interaction road noise. The experiments referenced were conducted over many years and differentiate noise between tires but still do not identify unequivocally the key attributes that accurately predict a tire's noise.

Since a majority of noise from the interaction is considered to be linked to the tire vibration, models have been developed to identify dynamic characteristics that contribute to noise levels. By using a ring model for a tire, Heckl identified key dispersion relations linked to phase velocities of multiple wave types on tires that reduced the model to a tensioned beam on springs [4]. Kropp built on this model and identified cut-on frequencies of various waves [5]. He found that the model degrades above approximately 400 Hz due to the model having one-dimensional limitations and suggested that two-dimensional waveguide behavior exists. By using a sixth-order differential equation, Pinnington conducted an in-depth theoretical analysis of the vibrations on the tire's belt including a side-wall model and identified the frequency ranges of various behaviors and linked them to specific tire attributes [6]. He found good correlation to responses in experimental analysis [7]; however, the identification of higher order transverse modes was not accomplished.

Bolton et al. developed an experimental solution to more accurately obtain waveguide information to model tire vibration [8]. By combining tire vibration measurements with a wave number decomposition, multiple wave types below 1000 Hz could be identified with an off-vehicle experiment. Slower modes, associated with flexural waves, cut-on at the first circumferential mode and subsequent second, third, and fourth modes converged towards an overall group speed. Faster modes cutting-on at zero wave number suggest a longitudinal wave or extension of the tire carcass. The higher wave speed associated with this wave type could relate to high radiation efficiency and thus predict a tire's potential for airborne noise.

Sabiniarz and Kropp developed a waveguide finite element model for a non-rotating tire without contact with the road [9]. They analyzed wave propagation using two different methods. The first method involved solving the eigenproblem for free waves on a curved waveguide, which provided insight for the dispersion of all waves propagating around the tires but lacked damping characteristics. For the second method, a radial point force was applied to the model, and the circumferential response was measured. The damping was included with this method, but only

waves excited by the input force could be analyzed. In the end, they came to a similar conclusion that the high phase speed of extensional waves should be efficient sound radiators.

1.2 Problem Statement

Currently, four major methods are standardized for measuring exterior tire/road interaction noise. The first three methods are the Coast-By, Close-Proximity, and Trailer Coast-By. All require tire(s) to be driven or pulled along a pavement surface. Each experiment has a significant cost associated with testing time, and the Coast-By and Trailer Coast-By methods have the additional cost of requiring four or two tires, respectively. The fourth method is known as the Laboratory Drum method. While having a low testing cost, it has an extremely high initial cost. Developing an off-vehicle laboratory test to predict the structure-borne and airborne noise potential of tires would allow for selection of a small set from a large population of tires for further testing using one of the four major methods. The results could also be used in models for cabin noise prediction.

When analyzing the mechanical vibrations resulting from the tire/road interaction, it has been suggested that: (i) airborne sound radiation is primarily associated with supersonic components and (ii) structure-borne components are primarily associated with the appearance of the $n = 1$ circumferential mode. An off-vehicle point mobility measurement of a tire provides a natural spatial-frequency response. A wave number decomposition analysis of the data can identify the necessary tire dynamic characteristics to allow a comparison of the noise potential of various tires.

1.3 Overview

In Chapter 2, the airborne and structure-borne noise generated from a variety of tires was is analyzed for comparison to the off-vehicle test. The experiment was based on using a unique piece of equipment to gain the benefits of the Close-Proximity

and Laboratory Drum methods. While the method does not account for propagation effects, it excels at testing tires and provides a variety of road surfaces on which to test.

In Chapter 3, the structural wave propagation on the sample set of tires was measured circumferentially. A radial point and patch excitation force were both examined to better understand how varying the input force area affected the response. A wavenumber decomposition was conducted on the various test results to visualize the tire's structural wave propagation characteristics. From the transformed data, the supersonic components were summed and the $n = 1$ circumferential modes were extracted to compare against tire/pavement noise data.

The focus of Chapter 4 is the development of a moving input function. Structural wave propagation varies based on input force. At certain speeds, the tread pattern could have an effect on the structure-borne noise by aligning with the tire's natural response modes. Thus an amplification of noise at certain speeds would occur. Theoretical periodic and random patterns were examined before applying the method to the sample set of tires.

In Chapter 5, a noise and vibration potential model is presented to rank tires relative to each other. The moving input function is combined with the wavenumber decomposition of the stationary tire experiment to predict the airborne and structure-borne noise from the two standard test methods for a second set of tires. The model is analyzed for validity and important noise characteristics are identified

The thesis concludes with Chapter 6 where the main outcomes of the current work are presented and ideas for future work are presented.

2. NOISE RADIATION AND VIBRATION OF A RADIAL TIRE

2.1 Introduction

Tire/road interaction is a major noise source for passenger cars. Thus, the identification of tires with lower airborne and structure-borne noise radiation benefits automobile OEMs, drivers, and communities. To develop an accurate tire-pavement noise prediction model, experimental data from multiple tires was collected.

2.2 Measurement of Noise Radiation

The acquisition of airborne noise and vibration from tire/road interaction in a laboratory environment requires a unique set-up and test procedure. The equipment used and how data was collected is discussed in this section.

2.2.1 Tire Pavement Test Apparatus

The Tire Pavement Test Apparatus (TPTA) was the primary piece of equipment used to collect noise measurements. It combines the controlled environment of the Laboratory Drum method with the Close-Proximity method because of the six different curved pavement samples that create a realistic tire/road interaction. Both methods suffer from not being able to account for propagation effects; however, since the focus of current research concerns predicting airborne and structure-borne noise from the tire's natural response, that disadvantage will not be a hindrance.

To collect noise data, the tire moves over six pavement samples that form a ring outside a 3.7 m diameter steel drum. The loading of the tire is controlled by two steel arms, which are attached to the rotating steel plate above the drum. The arms can apply a normal load to the tire from 0-4400 N (0-1000 lbs) $\pm$ 220 N (50 lbs).

The motor and gear system allow the device to reach a maximum rotational speed of approximately 1 revolution per second. This translates to a maximum speed of 13.4 m/s (30 mph) ± 0.5 m/s (1 mph). Noise measurements are collected per-pavement-sample since a variance in the thickness of the road sections affect the normal loading on the tire. A pre-test run time of 10 minutes at 13.4 m/s (30 mph) was utilized to reach a normal operational temperature for the tire.

2.2.1.1 Hemi-Anechoic Chamber

The TPTA resides inside a hemi-anechoic chamber. The sound-absorbing material on the walls and ceiling help create a low-noise floor for collecting accurate measurements. The concrete floor while undesirable from a noise reduction point of view was necessary to support the TPTA and allows easy access for maintenance or to change out pavement samples. Figure 2.1 shows the TPTA housed in the hemi-anechoic chamber.

2.2.1.2 Pavement Samples

The six different pavement samples were manufactured by previous graduate students at the Herrick Laboratories [10]. The technique used to introduce macrotexture and microtexture onto the concrete samples was longitudinal grinding. Diamond-infused steel blades with various spacers and set to different depths created unique surfaces. Figure 2.2 shows a snapshot of each pavement and lists some of their attributes.

2.2.1.3 Tires Tested

The set of tires selected for this experiment were chosen by the automobile OEM that sponsored this work. They represent a selection that would normally be used on a specific vehicle and were from several different tire manufacturers. Table 2.1 lists

Figure 2.1. Tire pavement test apparatus (TPTA) in hemi-anechoic chamber.

Figure 2.2. Concrete pavement samples on the TPTA.

the tires along with their key characteristics. To eliminate differences from various rims, all the tires had the same rim diameter and were mounted and balanced on a rim with a first free mode at 330 Hz. Tires were loaded to 3200 N (720 lbs) ± 220 N (50 lbs).

Table 2.1. List of Tires Tested.

Tire	Manufacturer	Tire Code	Identifying Type	Inflation Pressure	Tread Plies
1	Michelin	P225/50 R17	Pilot HX MXM4	32 PSI	Tire: 2 Polyester, 1 Polyamide, 2 Steel Sidewall: 2 Polyester
2	Michelin	P225/50 R17	Energy MXV4 S8	35 PSI	Tire: 2 Polyester, 1 Polyamide, 2 Steel Sidewall: 2 Polyester
3	Michelin	P225/50 R17	Energy Saver A/S	35 PSI	Tire: 1 Polyester, 1 Polyamide, 2 Steel Sidewall: 1 Polyester
4	Bridgestone	P215/55 R17	Turanza EL400	33 PSI	Tire: 2 Polyester, 2 Steel, 1 Nylon Sidewall: 2 Polyester
5	Continental	235/45 R17	ContiProContact	33 PSI	Tire: 2 Polyester, 2 Steel, 1 Nylon Sidewall: 2 Polyester
6	Kumho	P215/55 R17	Solus KH25	32 PSI	Tire: 2 Polyester, 2 Steel, 1 Nylon Sidewall: 2 Polyester
7	Firestone	P215/55 R17	FR710	30 PSI	Tire: 1 Polyester, 2 Steel Sidewall: 1 Polyester
8	Michelin	235/50 R17	Energy Saver A/S	32 PSI	Tire: 1 Polyester, 1 Polyamide, 2 Steel Sidewall: 1 Polyester

2.2.1.4 Background Noise Reduction

While the hemi-anechoic chamber provided an ideal recording environment, further modifications were required to ensure accurate data collection.

The TPTA utilizes a large motor and gear system to achieve the necessary speed for data collection. A blower was installed to prevent the motor from overheating. When the tire and microphones pass over certain pavement samples, the noise from the blower interfered with the tire/road noise data. The testing procedure was modified so that the blower was off while recording data and it was turned back on between testing runs.

Because the microphones and preamplifiers were moving with the tire at speeds up to 30 mph, airborne noise was generated by various objects that could interfere with the test. Wires were taped and tied down to the TPTA arm and hub struts. The preamplifiers and struts were wrapped with sound absorbing material. Finally, a wind screen covered the microphones to alleviate the wind noise.

2.2.2 On-Board Sound Intensity

Airborne noise measurements were conducted on the TPTA following procedures for the On-Board Sound Intensity (OBSI) method [11]. Brüel and Kjær Type 4197 phase-matched intensity pair microphones were attached above the leading edge of the tires normal to the tire sidewall and direction of travel. The spacing between the microphones was approximately 16.45 mm. This accounts for a finite difference error of <1 dB up to 3.8 kHz. The microphones were put 4 in. away from the tire sidewall to limit nearfield error from noise generating sources on the tire. The microphones transmitted pressure data through preamplifiers to a Brüel and Kjær Type 3032A Input/Output Module and Type 7533 LAN Interface Module. A wireless router connected to the LAN module sent the data to a laptop running Brüel and Kjær Time Data Recorder. Figure 2.3 displays the OBSI set-up without background noise modifications.

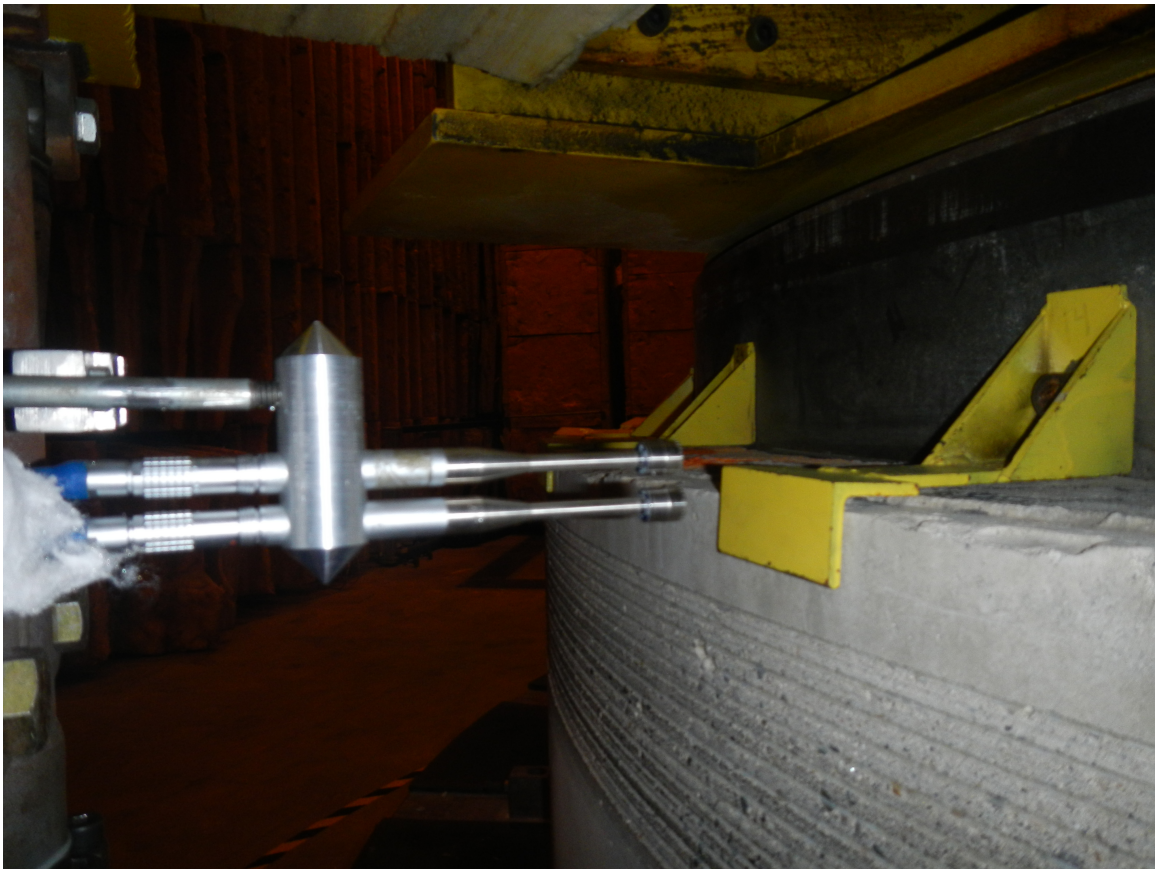

Figure 2.3. OBSI without background noise reducing measures.

The coherence of the two microphone signals derived from the tests is shown in Figure 2.4. The poor coherence across the spectrum for pavement 5 resulted in its removal from the analysis. The results also determined a lower bound third-octave center frequency of 315 Hz and an upper bound of 1250 Hz.

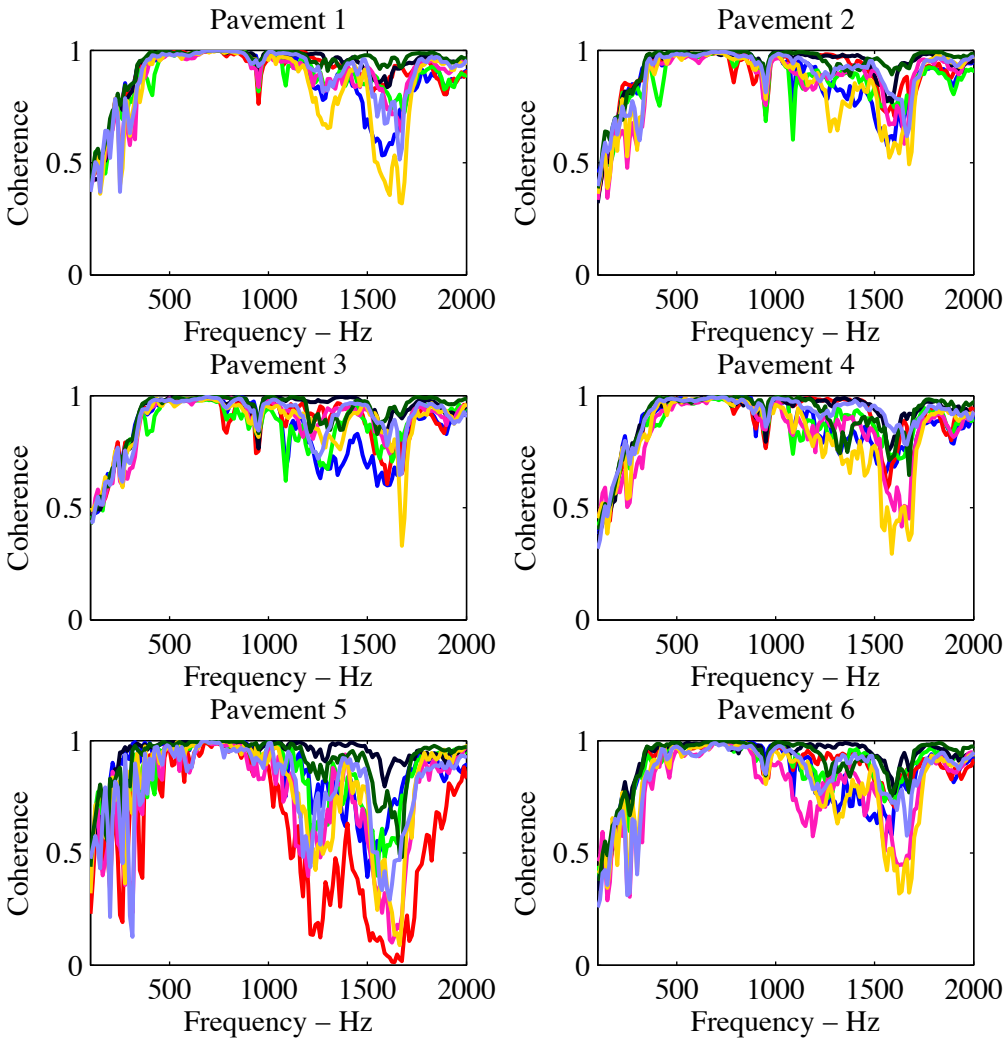

Figure 2.4. Per pavement coherence for all 8 tires.

The validity of the OBSI measurements was confirmed by checking the noise floor results. The noise floor was classified as the OBSI results obtained when running the TPTA without any load on the tire. The data in Figure 2.5 suggests that the noise floor has a significant effect on the 500 Hz third-octave band. This will be taken into consideration when calculating overall levels and when comparing with the stationary tire test.

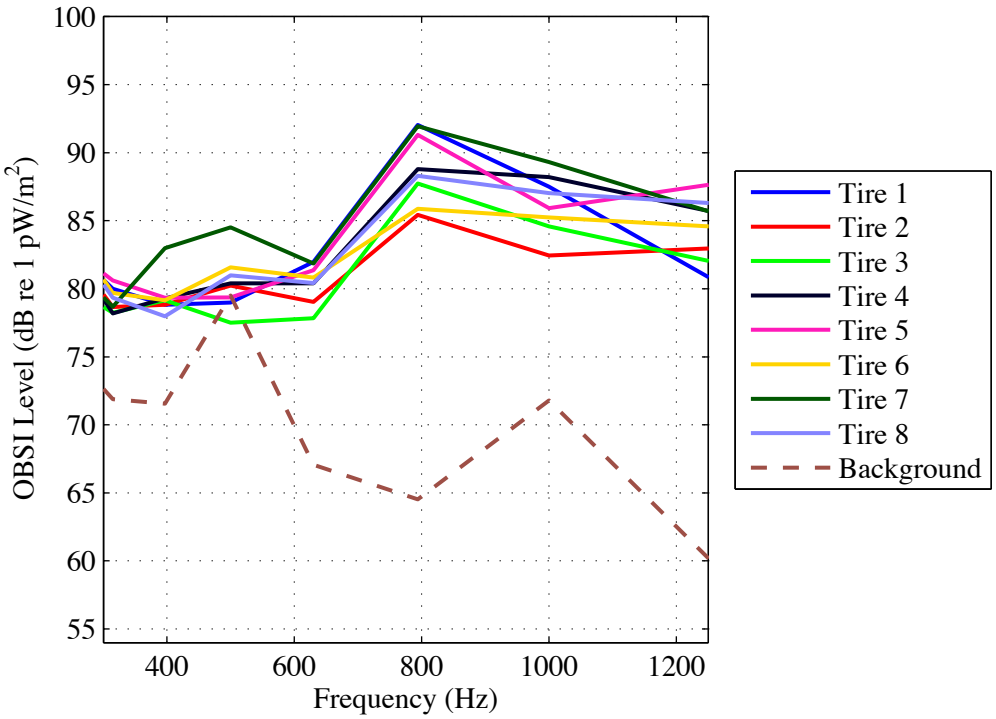

Figure 2.5. Intensity spectrum with noise floor measurement.

2.2.3 Vibration Testing

Structure-borne noise data was collected using a triaxial PCB 356A08 accelerometer. The accelerometer was installed on the hub assembly. This location was chosen to measure structure-borne noise delivered from the tire to the rest of the automobile.

The acceleration in the direction of travel (X-axis), out-of-plane direction (Y-axis), and normal to the pavement (Z-axis) were collected for analysis. Figure 2.6 shows the accelerometer mechanically fastened to the hub. A magnetic trigger system described in the next section was used to extract data from specific pavements in each recording.

Figure 2.6. Triaxial accelerometer at hub without tire installed.

The validity of the vibration test was confirmed by checking the noise floor measurements. The noise floor was classified as the vibrations measured by running the TPTA without any load on the tire.

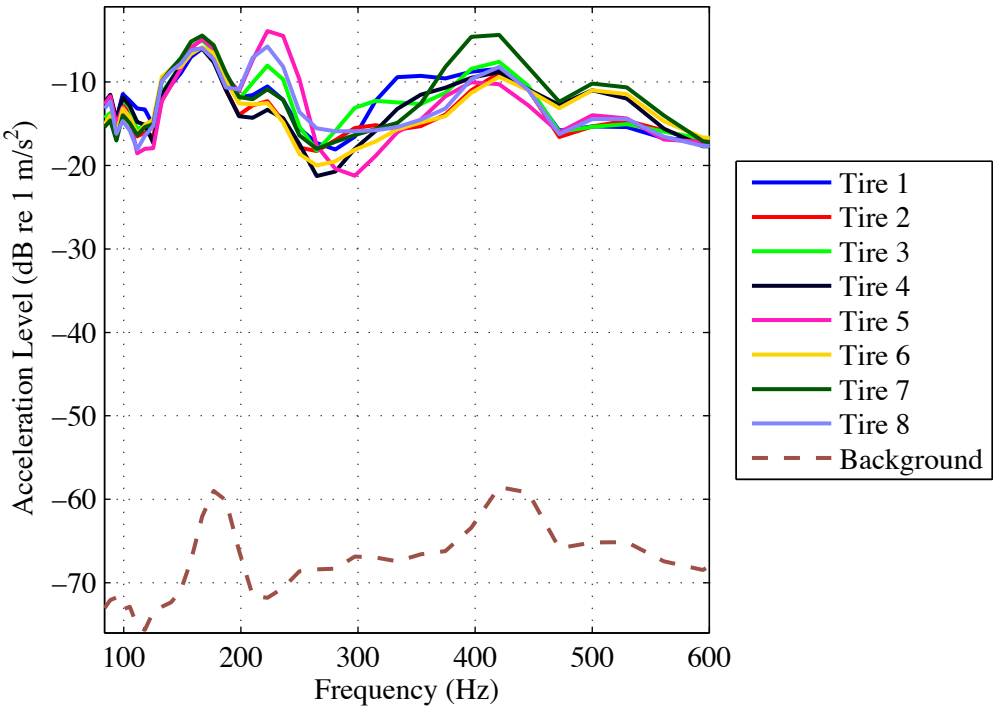

Figure 2.7. Normal acceleration (Z-axis) averaged over the five pavements for each tire compared with an unloaded tire's measurements.

As seen in Figure 2.7, the unloaded tire case exhibits significantly lower vibration measurements. Noise measurements for the X-axis and Y-axis are shown in Figures A.1 - A.2 in Appendix A.

2.2.4 Magnetic Triggering System

Each pavement must be analyzed individually because of the variance in normal force applied. To know the location of the tire as it moved over the different pavement samples, a magnetic trigger system was used. A magnetic pick-up is attached to the arm opposite to the OBSI set-up. When the TPTA rotates and the magnetic pick-up passes over a magnet placed above a pavement sample, a voltage spike is generated. By placing the magnet in the correct location, the airborne and structure-borne noise for each pavement sample can be pulled out of the experiment's total time history. Figure 2.8 shows the magnetic trigger set-up.

The original procedure called for the magnet to be placed where a spike would occur sometime after the tire rolled onto the desired pavement sample. This location was chosen with the idea that the noise generated from the impulse of the tire switching from the previous pavement to the current one would be damped out. This trigger event would signal the start of a data sample. This method has some problems associated with it. The testing of multiple tires across six pavement samples would create repeatability issues without accurate magnet placement. To determine when the impulse decays away, several preliminary tests would need to be conducted. Also, the procedure would leave the end of the pavement sample unknown. Therefore, the magnet location was set-up so that a spike would occur immediately before the tire rolled off the sample and onto the next. This defined the end of the data to be collected and allowed the start point to be adjusted by examining the time history to account for the pavement joint impulse. Figure 2.9 shows the identification of the transient and final window for segment averaging.

Figure 2.8. Magnetic trigger on arm opposite of the OBSI and triaxial accelerometer.

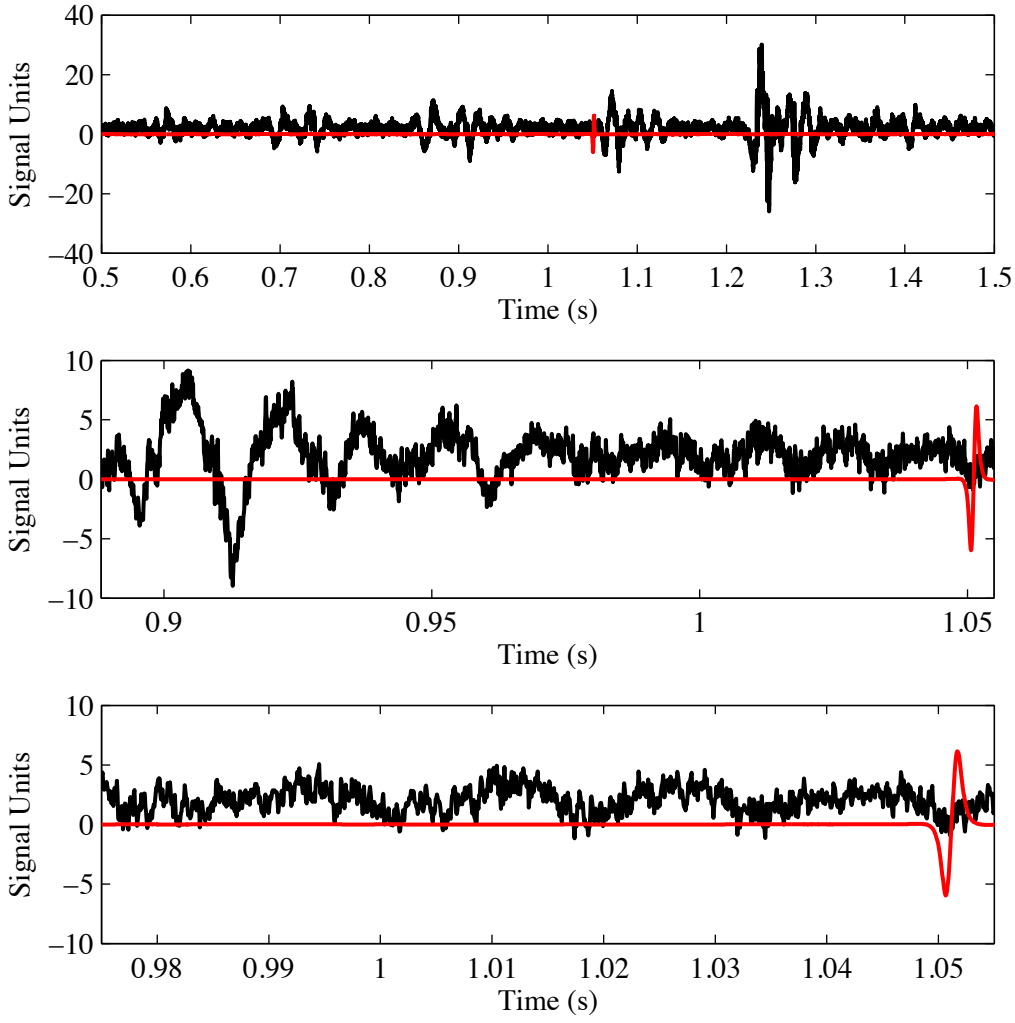

Figure 2.9. Top: 1 TPTA revolution (≈1 second for 30 mph) time history. Middle: 1 pavement sample time history. Bottom: 80 ms window for averaging. Black = Normal acceleration (1 m/s^2), Red = Trigger Signal (Volts).

2.2.5 Speed Variation

The off-vehicle test, discussed in Chapter 3, is based on an examination of the tire's dynamic characteristics. If the velocity of the tire has an effect on noise generation, the prediction model could rank tires incorrectly. Data was collected for the noisiest tire in 5 mph increments from 15 mph to 30 mph across the pavement samples.

2.3 Signal Processing

After collecting the sound pressure and vibration measurements, the data was exported from Brüel and Kjær Time Data Recorder to a .mat file. The files were imported into MATLAB for post-processing and analysis.

2.3.1 Trigger Signals

The recorded signal from the magnetic triggering system provided location data for testing each pavement. Figure 2.10 shows an example of a time history of the trigger voltage.

The signal was collected at a sample rate of 16384 Hz. When the trigger sensor is not over a magnet, the voltage is very low. Passing over a magnet creates a spike in the time history. A function was run to find when the voltage rose to reach 95% of the maximum value for the signal. These time values represented the end data points of the desired pavement sample and were stored in a location vector. A data window length, N, was calculated using $N = T * FS$ where T is the time window and FS is the sampling frequency. In combination with the location vector, data segments of length N were extracted out of the full microphone and accelerometer time histories.

2.3.2 Sound Intensity Data Processing

Sound intensity was calculated from the sound pressure time histories of the phase-matched intensity pair microphones. Airborne noise was recorded at a sample rate

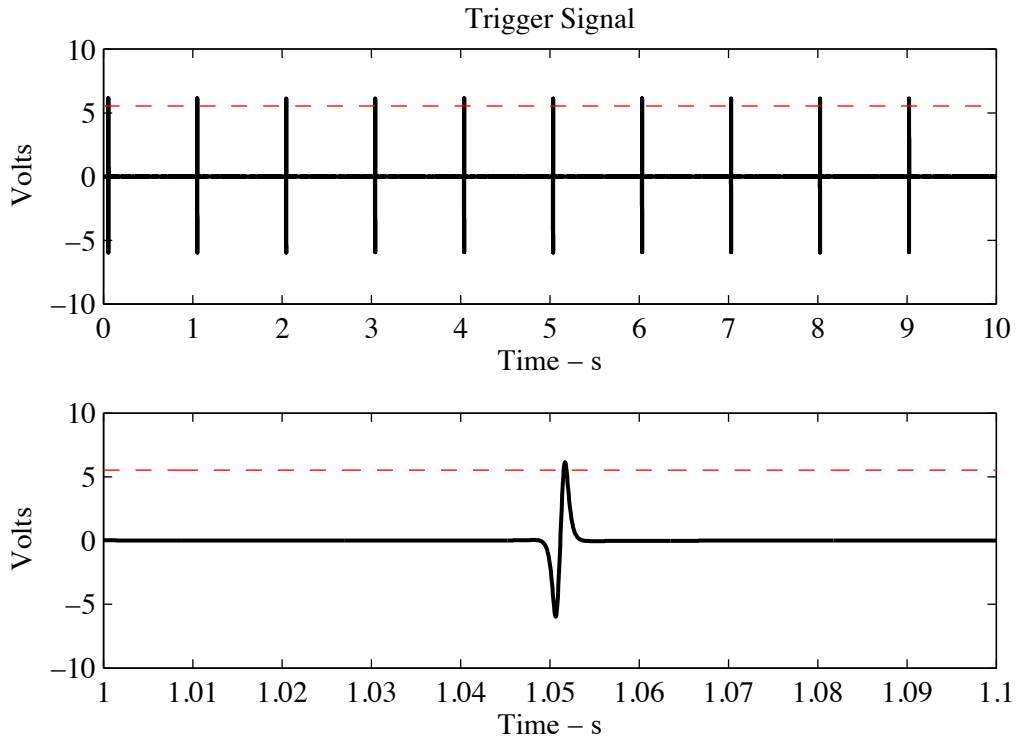

Figure 2.10. Two sections of the trigger signal with a 95% reference line overlaid.

of 16384 Hz to coincide with the trigger signal. By using the location vector, an 80 ms window was gathered from the time history of each microphone. In MATLAB, a Hann window was applied before calculating the discrete Fourier transform of each segment. The two-microphone cross-spectral approach was used to calculate narrow-band sound intensity by using Equation 2.1:

$$I = \frac{-\mathrm{Im}(P_1^* P_2)}{4\pi f \rho_0 \Delta} \tag{2.1}$$

where $\rho_0 = 1.21$ kg/m3 is the density of air, f is frequency in Hz, $\Delta = 16.45$ mm is the spacing between the microphones, and P_1 and P_2 are the complex sound pressure spectra from the respective microphones with the asterisk representing the complex conjugate. Four hundred measurements were made on each pavement sample, and the narrow-band sound intensity was averaged and summed into third-octaves for comparison and analysis.

2.3.3 Accelerometer Data Processing

Structure-borne noise was recorded at a sample rate of 16384 Hz and extracted from the tri-axial accelerometer time histories. As with calculating the sound intensity, 80 ms windows for each pavement sample were found using the triggering location vector. A Hann window was applied to each of the 400 measurements before performing a discrete Fourier transform in MATLAB. The narrow-band spectra were averaged and run through a twelfth-octave filter. The third-octave filter was not used because the maximum frequency of interest was 600 Hz, and a better resolution was desired to examine differences between tires.

2.3.4 Pavement Averaging

The different macrotextures and microtextures of the five usable pavement samples created a fluctuation in the airborne and structure-borne noise level across the

frequency ranges of interest. Figure 2.11 shows the differences across the various pavement surfaces for a single tire.

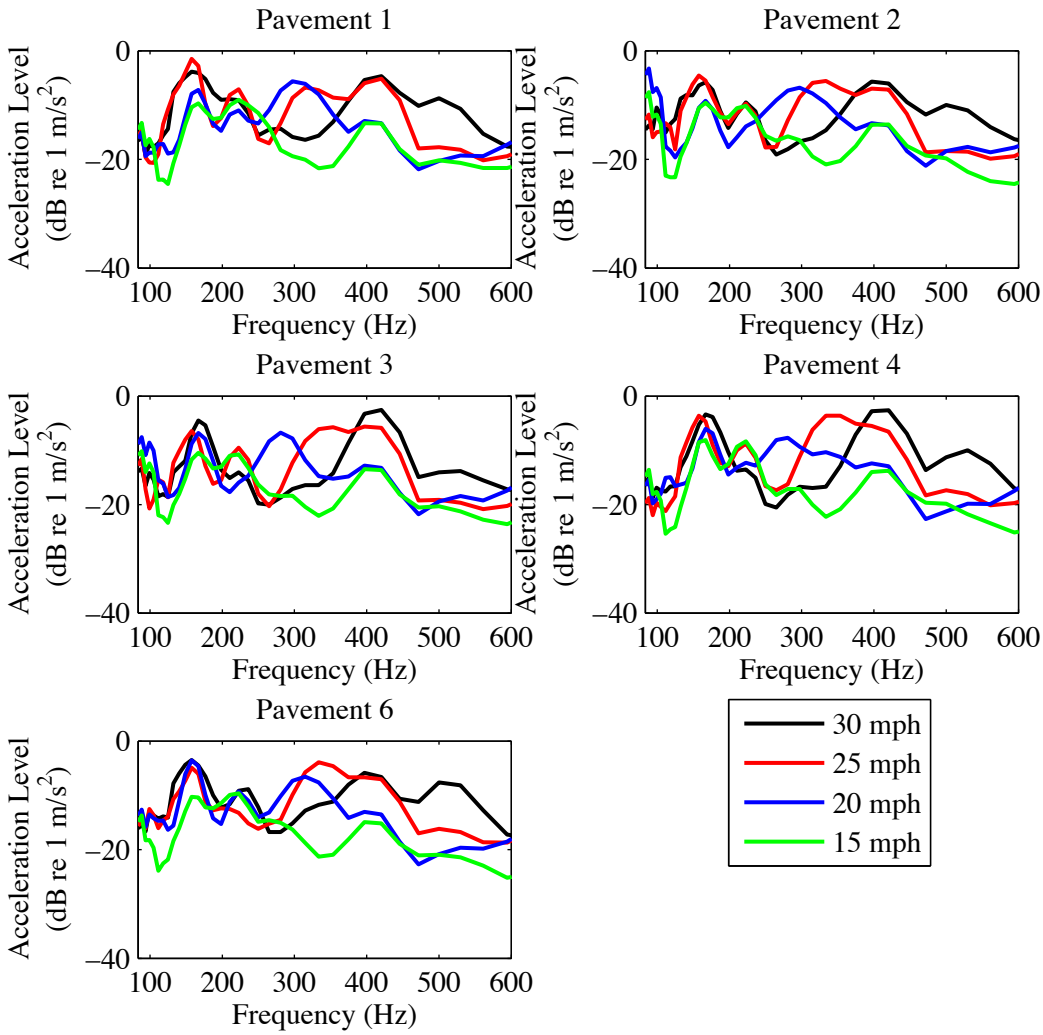

Figure 2.11. Per pavement normal acceleration (Z-axis) data for one tire.

Since the focus of the current research was creating a relative tire noise prediction model, the sound intensity and acceleration spectra were averaged across the five samples to reduce the variation caused by the pavements.

2.4 Results and Analysis

OBSI and accelerometer measurements revealed noise level similarities and differences between the eight sample tires. Spectral content plots were created for comparison with the off-vehicle test. Overall airborne and structure-borne noise levels were calculated to develop a relative ranking of quietest to loudest tires. The OBSI and acceleration levels are not A-weighted.

2.4.1 OBSI Measurements

2.4.1.1 Sample Set, Full Speed

Figure 2.12 is the pavement-averaged sound intensity level spectra for the TPTA operating at 30 mph and with the tires inflated to their recommended pressures. The results for each pavement are plotted in Figure A.3 in Appendix A. With the exception of tire 6, a distinct peak in sound intensity level is observed near 800 Hz. Below 630 Hz, appears to be mainly the noise floor. Above 630 Hz, the rank of loudest to quietest is relatively stationary. The tires stay within roughly two groups except for tire 1, for which the level decreases sharply from 1000 Hz to 1250 Hz. Overall levels in Table 2.2 provide the rankings for comparison. Levels were calculated without the 500 Hz third-octave band.

2.4.1.2 Tire 7, Varying Speed

Figure 2.13 is the pavement-averaged sound intensity level spectra for Tire 7 with it inflated to the recommended pressure and varying in speed from 15 mph to 30 mph in 5 mph increments. The results for each pavement are plotted in Figure A.4 in Appendix A. Above 630 Hz, the sound intensity level spectra maintains the same shape, a consistent peak at 800 Hz, but scales with speed. Below 630 Hz, the start of the linear increase in to the sound intensity level decreases in frequency with lower

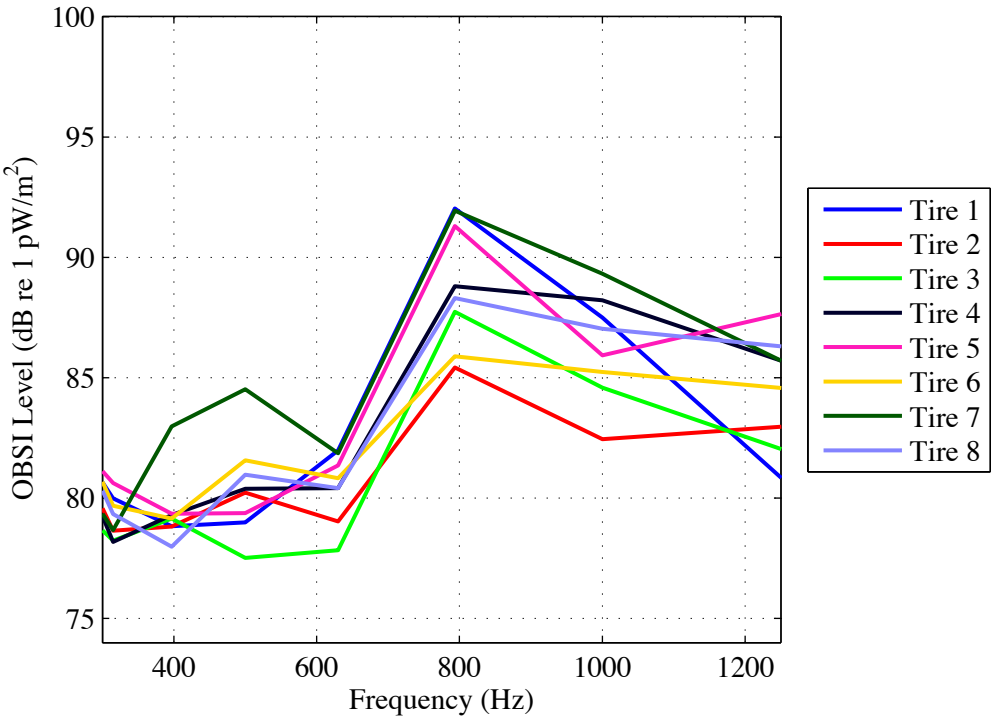

Figure 2.12. Averaged sound intensity level for eight tires.

Table 2.2. Overall sound intensity level of each tire for the defined spectra.

Rank	Tire	OBSI Level (dB re 1 pW/m^2)
1 (Loudest)	7	94.6
2	1	93.9
3	5	93.6
4	4	92.9
5	8	92.1
6	6	90.8
7	3	90.0
8 (Quietest)	2	89.4

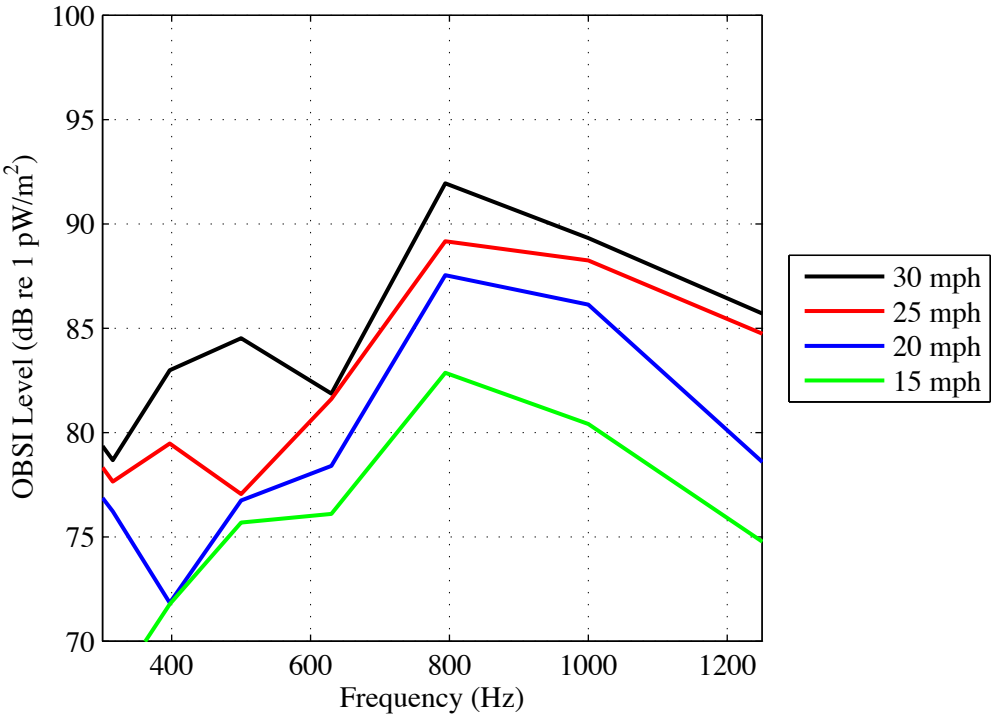

Figure 2.13. Averaged sound intensity level at different speeds for tire 7.

speeds. Overall levels in Figure 2.14 show a linear increase in sound intensity level with respect to a logarithmic speed.

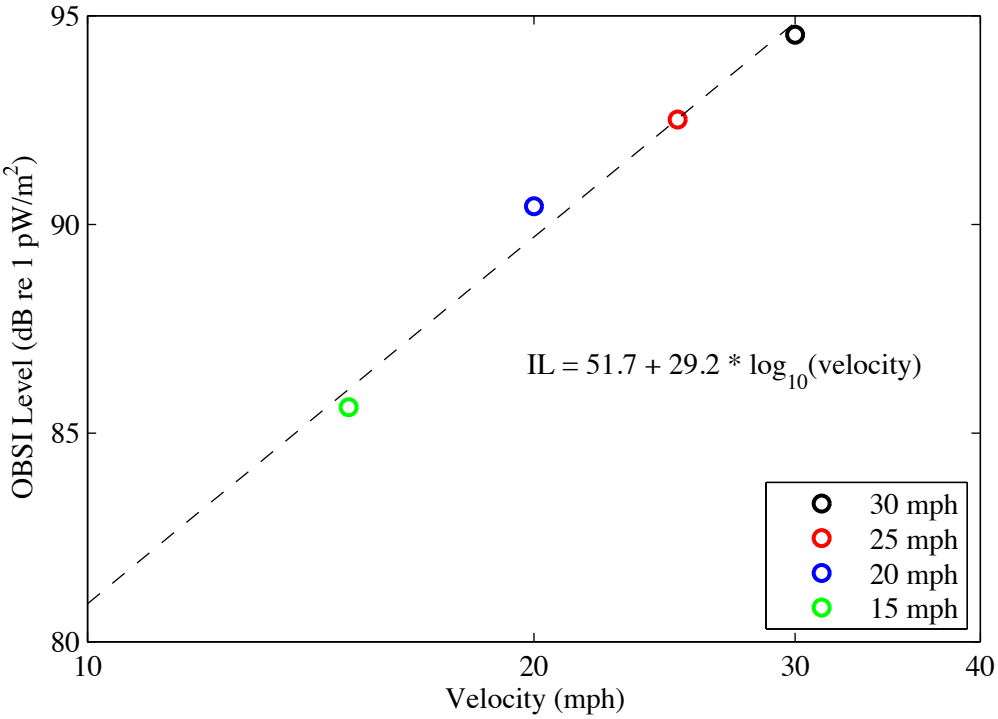

Figure 2.14. Overall sound intensity level at different speeds for tire 7.

2.4.2 Accelerometer Measurements

2.4.2.1 Sample Set, Full Speed

This section presents the pavement-averaged acceleration spectra for the TPTA operating at 30 mph and with the tires filled to their recommended pressures. The results for each pavement are plotted in Figures A.5 - A.7 in Appendix A.

The spectral content for acceleration in the X-axis direction is shown in Figure 2.15. A defined peak exists at approximately 160 Hz but varies in level for each tire.

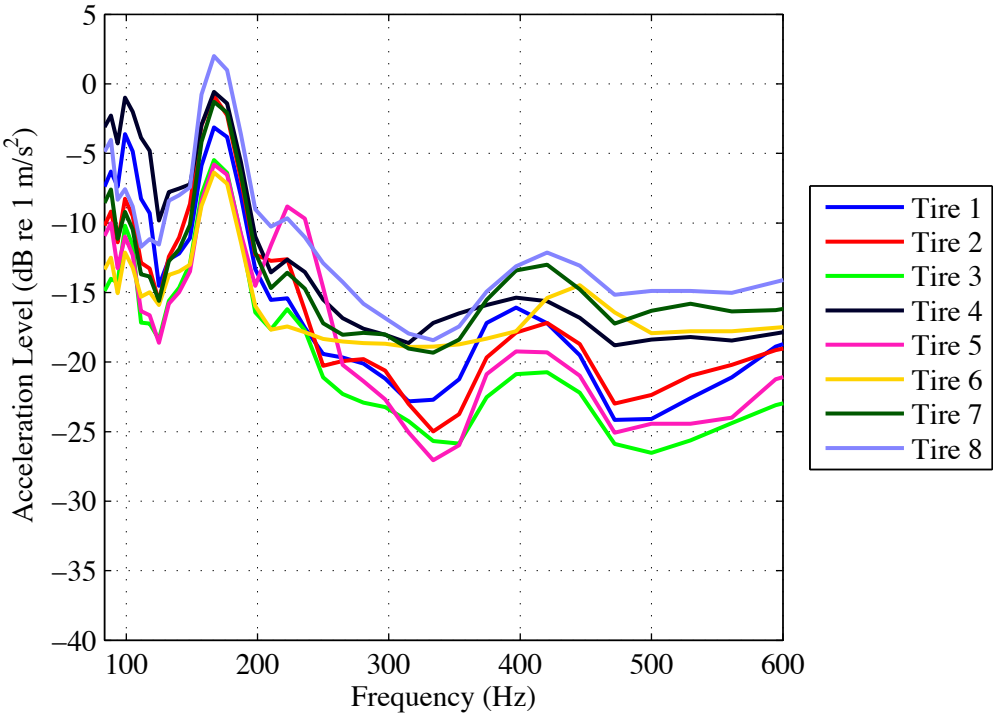

Figure 2.15. Acceleration in the tire's direction of travel (X-axis) for eight tires.

The vibration levels across the rest of the spectrum appear to be nearly flat and suggests that random vibration is applied to the hub in the X-direction which masks specific tire structure-borne noise characteristics.

Figure 2.16 displays the acceleration in the Y-axis direction. The out-of-plane

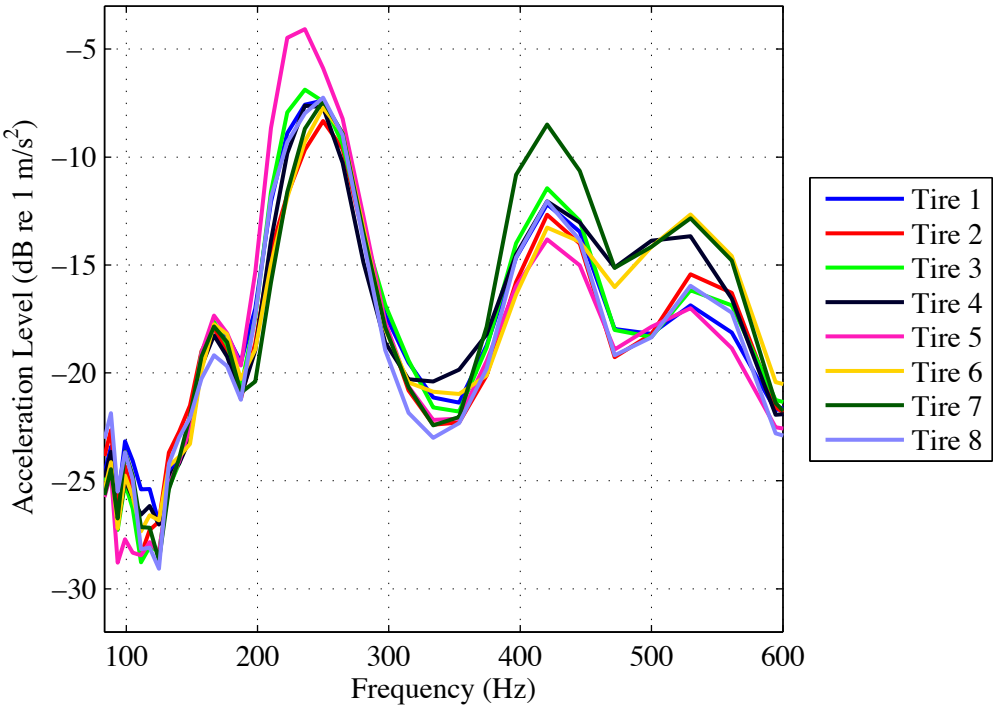

Figure 2.16. Out-of-plane acceleration (Y-axis) for eight tires.

acceleration has a peak running from approximately 160 Hz to 300 Hz that is not seen in the other accelerometer measurements. Since there is very little variation in level at these frequencies for the 8 tires, this vibration could be related to the rim or the TPTA rig. The peaks existing between 400 Hz and 600 Hz are ranked similarly to the normal acceleration measurements.

The normal acceleration (Z-axis) shown in Figure 2.17 displays the most variation and highest levels across the spectrum of interest for structure-borne noise. Similar to the X-axis direction acceleration, a peak around 160 Hz exists, but the small variation

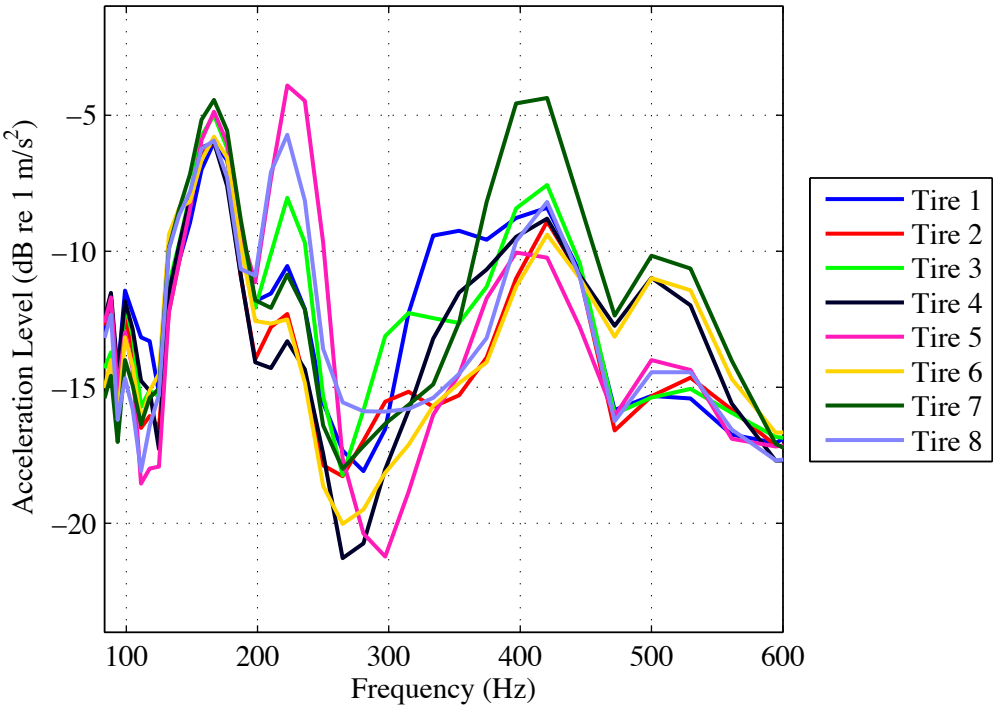

Figure 2.17. Normal acceleration (Z-axis) for eight tires.

in level across the eight tires which suggests a non-tire influence, especially since it also exists at a much lower level in the unloaded tire test. The peak around 210 Hz - 220 Hz correlates strongly with the suggested appearance of a tire's first acoustic mode. The vibration measurements above 350 Hz would indicate the cut-on of higher order transverse modes at the ring frequency of each tire. Overall levels for normal acceleration in Table 2.3 provide the rankings for comparison. Levels were calculated without the assumed non-tire noise at the 157 Hz, 167 Hz, and 177 Hz twelfth-octave bands. The off-vehicle test will ideally predict the structure-borne noise for each tire with levels relatively similar to the normal vibration measurements.

Table 2.3. Overall structure-borne noise level of each tire for the defined spectra.

Rank	Tire	dB re 1 m/s^2
1 (Loudest)	7	4.6
2	5	4.3
3	8	3.8
4	3	3.7
5	1	3.5
6	4	2.8
7	2	2.6
8 (Quietest)	6	2.5

2.4.2.2 Tire 7, Varying Speed

The following results and discussion are related to the pavement-averaged acceleration measured for tire 7 filled to the recommend pressure and varying speed from 15 mph to 30 mph in 5 mph increments. Acceleration data per pavement and direction are plotted in Figures A.8 - A.10 in Appendix A.

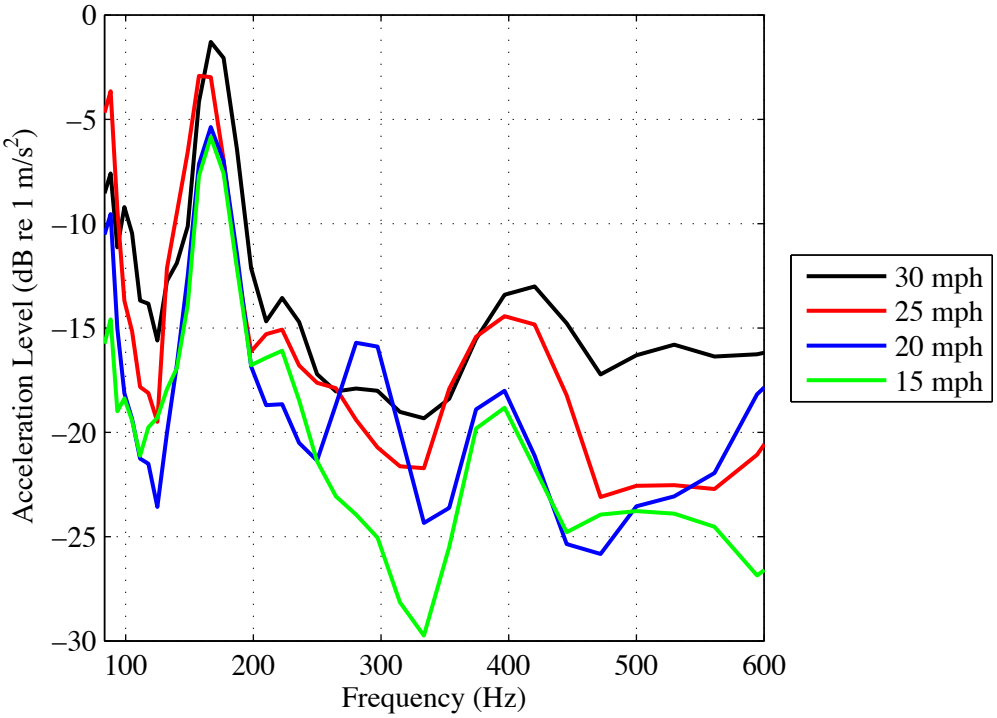

Figure 2.18. Acceleration in the tire's direction of travel (X-axis) for tire 7 at various speeds.

In general, a level change across the spectrum occurs when varying speed for the acceleration along the X-axis as shown in Figure 2.18. The noise around 160 Hz persists at all speeds and further suggests that it results from a noise source not related to the tire itself.

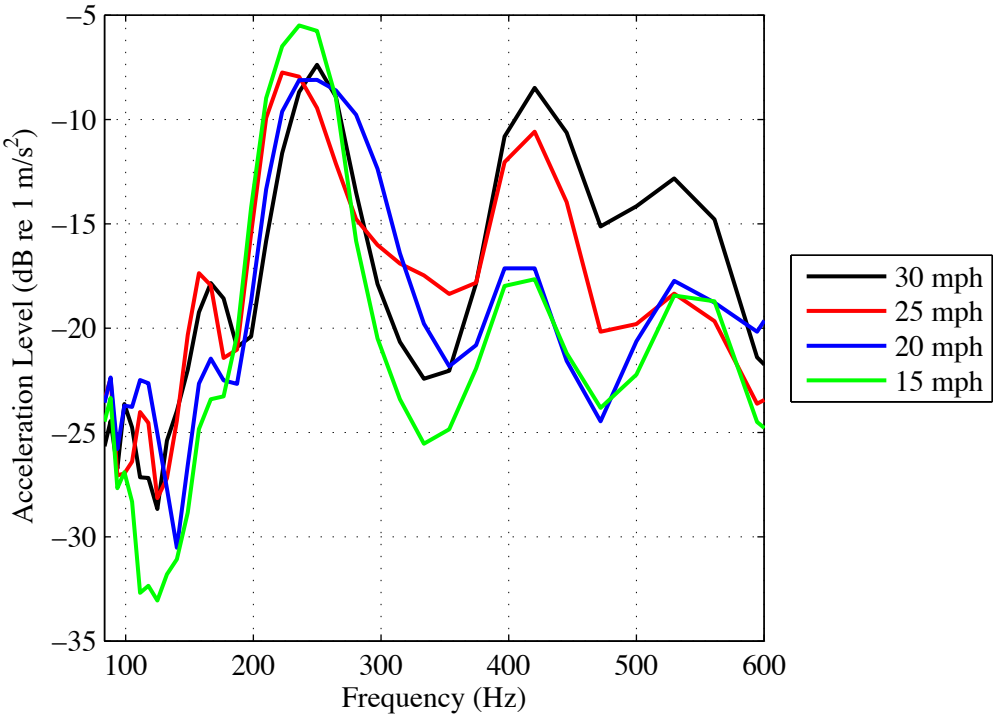

Figure 2.19. Out-of-plane acceleration (Y-axis) for tire 7 at various speeds.

Figure 2.19 reveals that the out-of-plane acceleration also shows a level change through frequency. From approximately 160 Hz to 300 Hz, speed independent structure-borne noise exists indicating a non-tire contribution.

As with the sample set, full speed results, the normal acceleration (Z-axis), Figure 2.20, appears to display the most variation through frequency. Similar to the X-axis acceleration, a peak relatively independent of speed appears around 160 Hz. However, the remaining spectrum levels are not just scaled. There appears to be a shift down

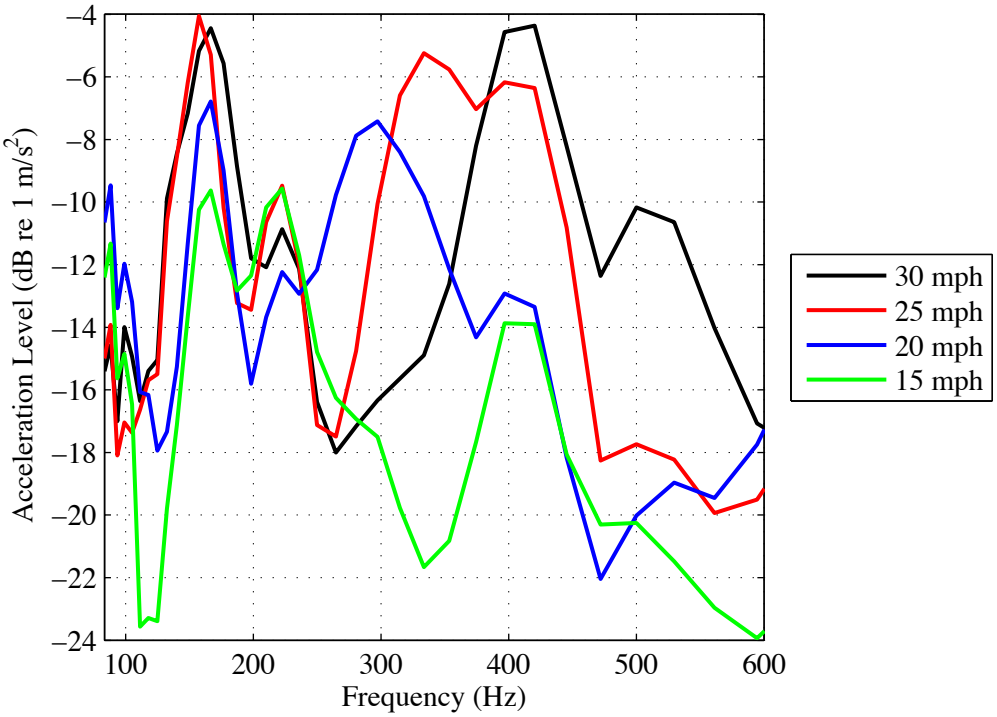

Figure 2.20. Normal acceleration (Z-axis) for 8 tires.

in frequency of spectral features with decreasing speed. This variation suggests that the normal acceleration has a dependency on speed besides a simple variation in level.

An overall structure-borne noise level for each acceleration direction was calculated after removing non-tire noise contributions. Figure 2.21 shows that when plotted against a logarithmic speed axis the Y-axis acceleration has a very linear scaling. The X-axis acceleration appears to also scale linearly but has some slight variation that is also seen in the Z-axis acceleration. While the normal acceleration increases with speed, the relationship has characteristics that suggest it is not just a linear change in level.

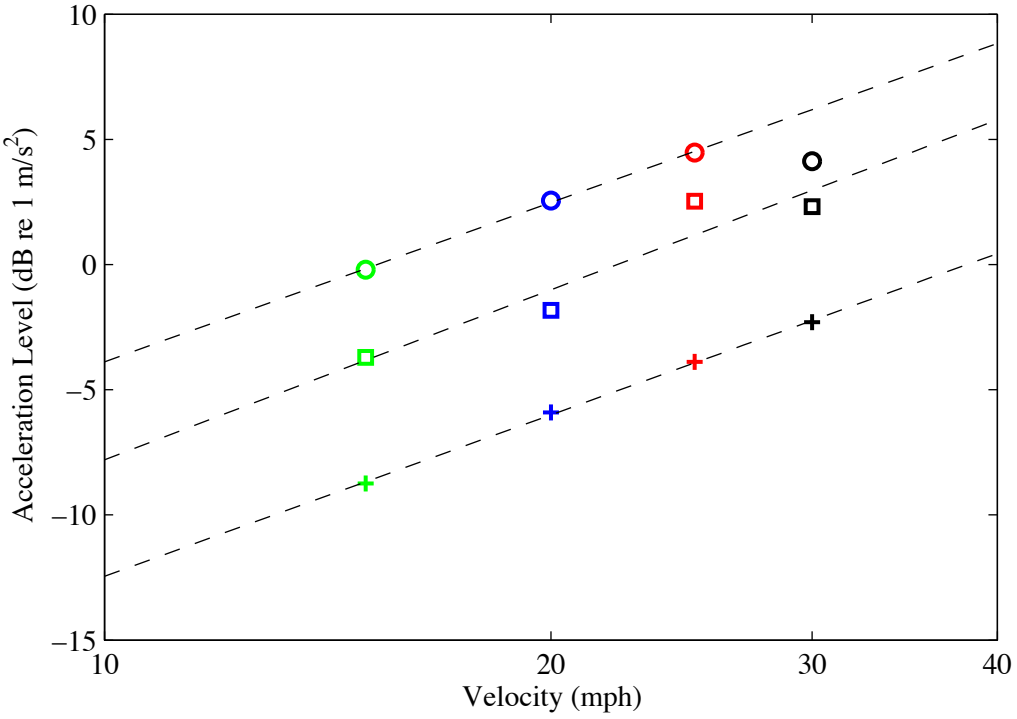

Figure 2.21. Overall acceleration levels at different speeds for tire 7 (square = X-axis, plus = Y-axis, circle = Z-axis).

2.5 Summary of Noise Radiation and Vibration of a Radial Tire

The TPTA experiment provided valuable insight into the tire/road interaction noise. The OBSI measurements results showed a consist peak frequency for all the tires at the 800 Hz third-octave band. This peak persisted through varying speed for a single tire. The spectral content in this frequency range correlated strongly with numerous tests shown by Sandberg and Ejsmont [3]. The defined ranks at and above the 630 Hz band suggest a cut-on of sound radiation attributed to tire specific characteristics. The experiment also confirmed how airborne noise relates to speed with linear change in dB IL for a logarithmic increase in speed. Concerning vibration, results from two of the three axes tested did not provide clear evidence for variation in structure-borne noise across the spectrum. The normal acceleration measured revealed unique spectral content and overall level differences. By changing the speed of the TPTA, the normal vibration again had the most interesting characteristics with a peak feature decreasing in frequency as the speed was lowered. The results should provide a wide enough range of airborne and structure-borne noise to compare against the off-vehicle experiment's data for predicting a tire's noise potential.

3. STRUCTURAL WAVE PROPAGATION ON A RADIAL TIRE

3.1 Introduction

A reduction of the monetary and time costs associated with collecting tire noise data for relative comparison is a priority for automobile OEMs. An analysis of the structural wave propagation of a tire could provide the necessary data to predict airborne and structure-borne noise potential of each tire. That idea is explored in this chapter.

3.2 Measurement of Structural Wave Propagation

3.2.1 Stationary Tire Test

To measure the natural response of a tire circumferentially, the tires were mounted to a stand with no significant vibrational modes up to 2000 Hz. The tire could be rotated 360 degrees for ease of measurement with the Polytec Scanning Vibrometer equipment. White noise was created within the Polytec software and was sent from the Polytec Junction Box through a Wavetek Dual HI/LO Filter model 852 set to a frequency range of 40-2000 Hz. The filtered signal was split to be sent back to the Polytec Junction Box for verification and sent to be amplified by a QSC Stereo Amplifier model 1080. The output from the amplifier was delivered to a Brüel and Kjær Type 4810 shaker fastened to the stand. The shaker could be adjusted normal to the tire and across the tire width to locate the stinger where required. The normal force produced by the shaker was delivered through a stinger to a PCB 208A02 Force Transducer, which was connected to the Polytec Junction Box. A small pad or beam, depending on the forcing method, was mechanically fastened to the force transducer and was chemically attached to the tire. The normal velocity on the tire surface

between the tread rows was measured using a Polytec PSV-400 Scanning Head with a PSV-A-420 Gemoetry Scan Unit attached. The data was transmitted from the scanning head to the vibrometer controller, to the junction box, and finally to a computer running the Polytec Scanning Vibrometer software.

Data was taken for 800 ms at a sample rate of 16384 Hz. The spectra for each point circumferentially had a frequency resolution of 1.25 Hz and was averaged over 60 measurements. A Hann window was applied to both the velocity and force data. During the test, the coherence of the point mobility was verified for each circumferential point.

Figure 3.1 is the tire stand used for the experiment, and Figure 3.2 shows an experimental test.

3.2.1.1 Laser Vibrometer

The Polytec PSV-400 Scanning Head measured the normal velocity of the tire with a sensitivity of 1 mm/s/V. The PSV-A-420 Gemoetry Scan Unit allowed the laser to correct for the curvature of the tire. Since tires have a dark surface, the scanning head registered a very low signal level, which increased the noise in the measurement. Magnaflux Spotcheck Developer SKD-S2 was applied to each tire before the scans. The increased reflectivity improved the signal to noise ratio and raised the point mobility coherence to almost 1 across the spectra. Figure 3.3 demonstrates the difference in the tire tread with and without the Magnaflux.

3.2.1.2 Point Excitation

A hexagonal pad was mechanically fastened to the PCB 208A02 Force Transducer. The pad was chemically attached to a tread block not along the centerline of the tire. This set-up would excite multiple transverse modes along with the circumferential modes. Figure 3.4 shows the point excitation arrangement.

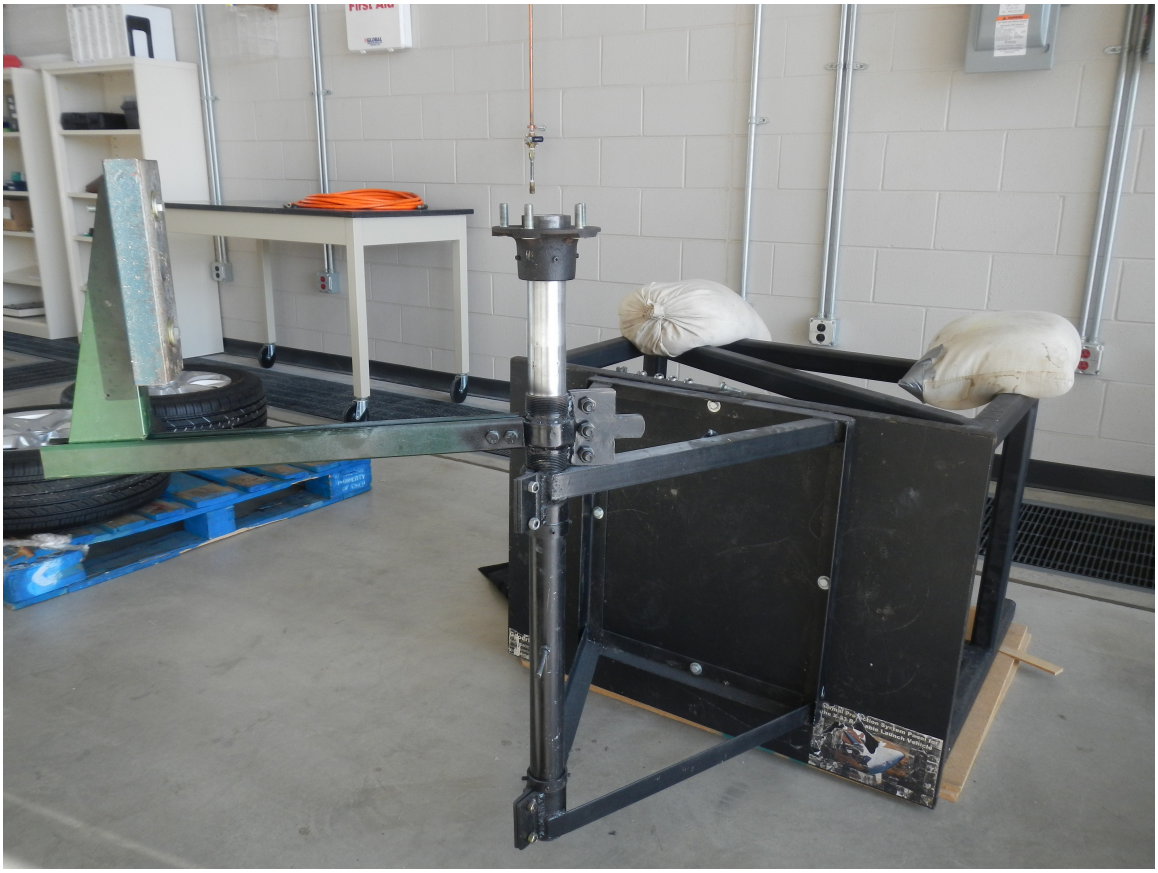

Figure 3.1. Tire stand without a tire mounted.

Figure 3.2. Stationary tire test in action.

Figure 3.3. Tire before adding the Magnaflux Spotcheck Developer SKD-S2 (left half) and after (right half).

Figure 3.4. Point excitation set-up for the stationary tire test.

3.2.1.3 Patch Excitation

A small aluminum beam 4 x 1 x 1/4 in. was created to deliver the patch excitation. The size and material was chosen so that the first bending natural frequency would occur at approximately 3.2 kHz. The beam was mechanically fastened to the force transducer and was chemically attached at the tire centerline across multiple tread blocks. The patch excitation was designed to simulate the effect of an area of the tire being compressed, as when the tire is loaded on the TPTA or on an automobile. This arrangement of excitation, as seen in Figure 3.5, should result in fewer transverse modes appearing in the wavenumber decomposed data.

Figure 3.5. Patch excitation set-up for the stationary tire test.

The beam unfortunately prevented a measurement point from being recorded with the laser vibrometer. It was decided that a post-processing fitting technique would be used to account for the point and complete the circumferential point mobility.

3.3 Signal Processing

The Polytec software was used to calculate the H1 point mobility and coherence circumferentially on the tire. The data was imported into MATLAB for post-processing and analysis.

3.3.1 Wavenumber Decomposition

The point mobility results were placed in a matrix format from -π to π spatially and 0 to 2 kHz spectrally. By using Equation 3.1 taken from Bolton et al. [8]:

$$v_r(\theta) = \sum_{n=-\infty}^{\infty} a_n e^{-ik_{\theta_n} s} \tag{3.1}$$

a wavenumber decomposition was performed on the data where s is the distance from driving point to a measurement location, and k_{θ_n} is the circumferential wavenumber ($k_{\theta_n} = n/r$ with r as the radius of the tire). Each n component is a circumferentially propagating disturbance of the radial velocity at the specified point. The processing was done by using a discrete Fourier transform algorithm on the spatial data at each frequency. The output matrix contained frequency-wavenumber data that was analyzed for wave speed and attenuation.

3.3.2 Vibration Potential Data Processing

A prediction of structure-borne noise was calculated from the wavenumber decomposed circumferential point mobility. Figure 3.6 shows the layouts of the various circumferential modes.

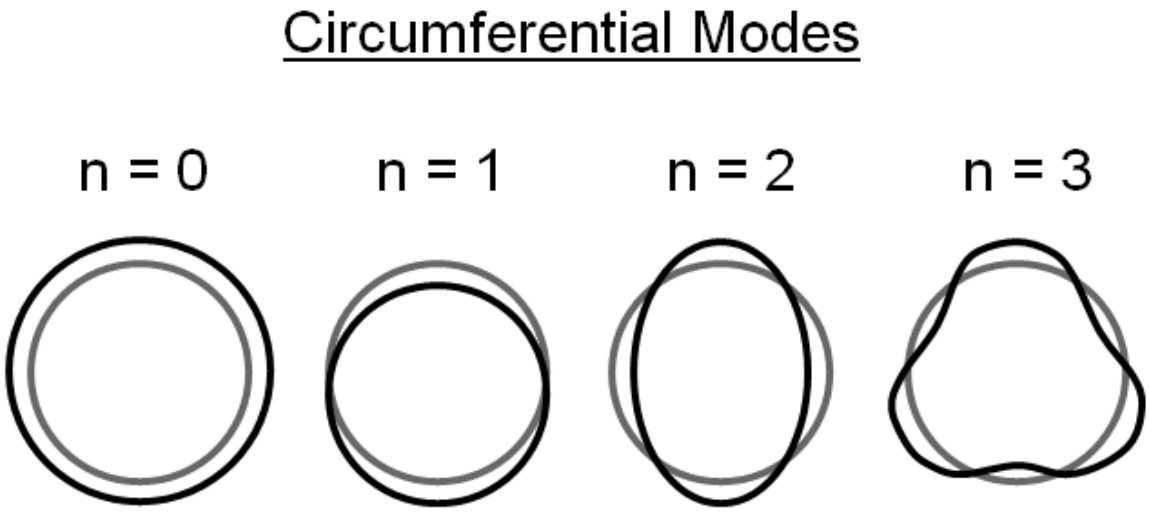

Figure 3.6. The first four circumferential modes of a tire.

In principle, the only circumferential mode that provides a net force to the hub is the $n = 1$ mode or the first circumferential wave number k_1. Therefore, the $+k_1$ and $-k_1$ spectra were summed and twelfth-octave filtered for comparison with the acceleration measurements from the TPTA experimental data. The transverse modes, from bead-to-bead, cut-on at different frequencies for each tire because of the variations in width and construction material. This should create spectral differences between the tires' vibration potentials.

3.3.3 Airborne Potential Data Processing

The prediction of airborne noise from the wavenumber decomposition required a unique calculation procedure. In the frequency-wavenumber domain, a slope constructed using $\frac{\Delta f}{\Delta k}$, where f is frequency and k is wavenumber, is considered to be the wave speed of each $|a_n|$. If it is assumed that only waves traveling as fast or faster than the speed of sound can radiate as airborne noise, the supersonic $|a_n|$ values at each frequency were squared and integrated across the wavenumber spectra. The resulting vector was a sum of the supersonic components through frequency. It will be referred to as the airborne potential of the tire and was third-octave filtered for comparison to TPTA data.

3.4 Results and Analysis

3.4.1 Circumferential Spectral Plots

The eight tires were tested with the point excitation arrangement first. The circumferential spectral plot for Tire 8 is plotted in Figure 3.7. The remaining seven tires are shown in Figures B.1 - B.7 in Appendix B.

Each tire exhibits unique characteristics, but there are several similarities. The H1 point mobility has frequency ranges where similar features exist for all the tires. From approximately 100 Hz to 350 Hz, a very regular pattern suggests a wave type

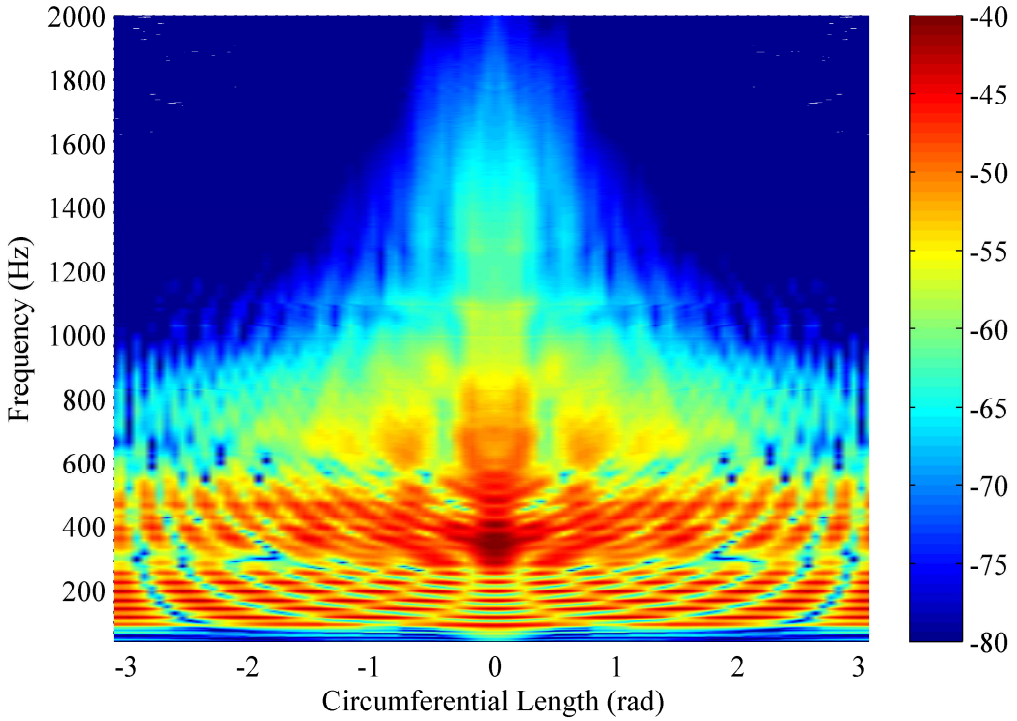

Figure 3.7. Circumferential spectral plot for Tire 8.

consistent for tire's of similar size and shape. Since the patterns extend circumferentially, they can be viewed as standing waves existing at specific frequencies. The transition at approximately 300 Hz - 450 Hz is a change in wave type and/or speed. The difference in spectral content and decay in magnitude away from the drive point (0 radians) signifies a cut-on of a different wave type. The tires' natural damping prevents a standing wave from developing. However, faint traces of the lower frequency modes are seen. Above 1200 Hz, a change can be seen in several tires. There is a more drastic decrease in level while moving away from the drive point. The point mobility coherence above 1200 Hz also showed a drop with increased distance from the excitation. This range could signify the cut-on of another wave that is heavily damped by the tire's attenuating characteristics.

The patch excitation variation was performed on three tires to compare the differences between forcing methods and decide which would be more beneficial in finding airborne and structure-borne noise potential. Figure 3.8 is the point mobility from patch excitation of Tire 8. Figures B.9 and B.10 are the circumferential spectral plots from patch excitation of Tire 5 and Tire 7 respectively in Appendix B.

A comparison of the two forcing methods in the low frequency range, 100 Hz to 400 Hz, showed little difference. The next spectral range, however, had a reduction in magnitude near the driving point, but maintained the circumferential pattern. Continuing higher in frequency, the patch excitation magnitude similarly decays moving away from 0 radians but extends to a higher frequency range than the point excitation. The wavenumber decomposition plots will reveal more information on these differences.

3.4.2 Wavenumber Decomposition Plots

Frequency-wavenumber plots were created after performing the wavenumber decomposition on the circumferential point mobility data for each tire. Figure 3.9 below is the wavenumber decomposition plot for Tire 8 with point excitation. Lines rep-

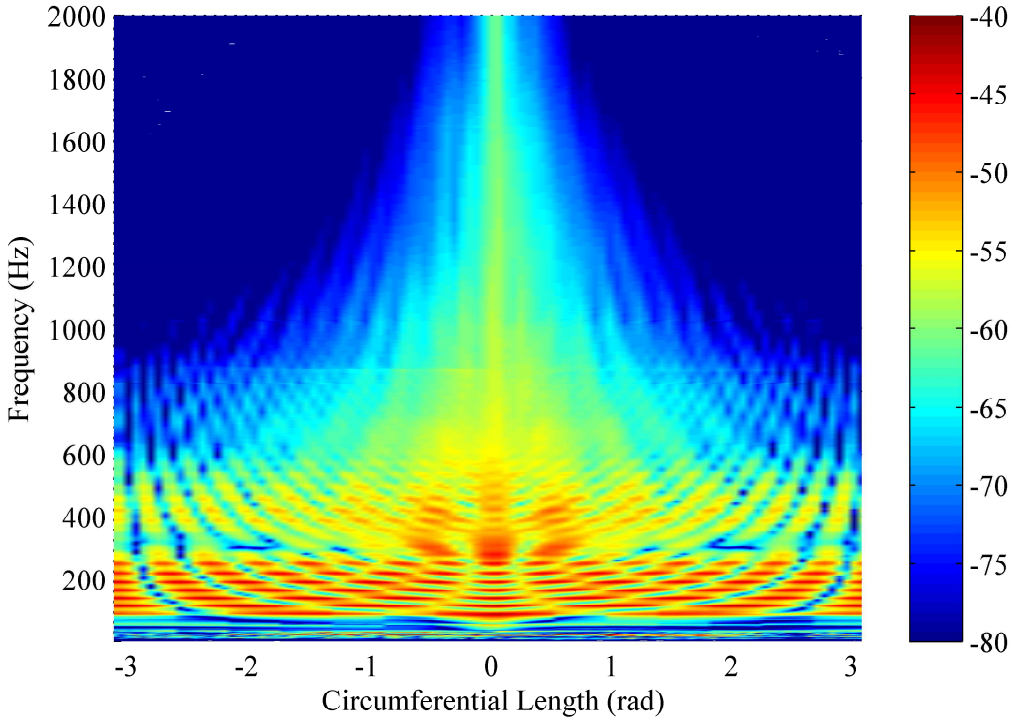

Figure 3.8. Circumferential spectral plot for Tire 8 from patch excitation.

resenting two phase speeds were overlaid to show the difference between supersonic components that could contribute to airborne noise and slower moving flexural waves. In Appendix B, Figures B.12 - B.18 are the frequency-wavenumber plots for the remaining tires.

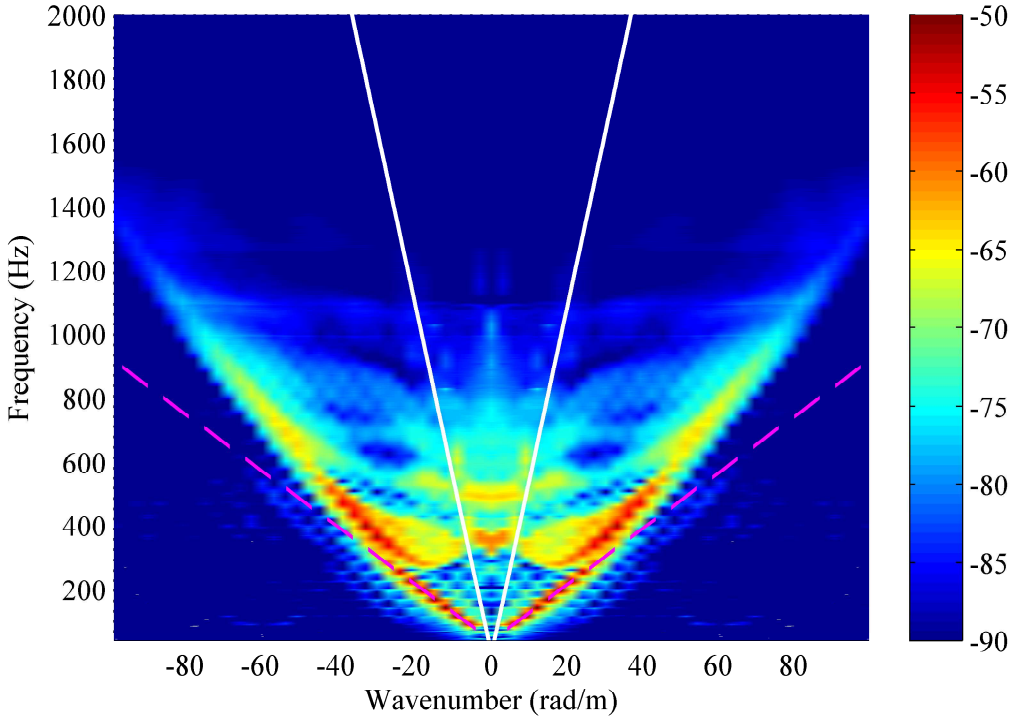

Figure 3.9. Frequency-wavenumber plot for Tire 8 (White = Speed of Sound (340 m/s slope), Pink = 60 m/s phase speed).

As with the circumferential spectral plots, features exist within certain frequency ranges. A slow moving wave (60 m/s - 80 m/s) propagates in the 100 Hz - 350 Hz range. The 350 Hz - 800 Hz range has a similar slow moving wave in the higher wavenumbers, but a faster wave also cuts-on around the ring frequency (350 Hz - 450 Hz). Above 800 Hz, the magnitude drops significantly. Another fast wave may cut-on around the 1100 Hz - 1200 Hz range. Lastly, a higher order circumferential acoustic

mode appears around 850 Hz and 1050 Hz, notably in the frequency-wavenumber plot for tire 8.

The patch excitation wavenumber transformed data for Tire 8 is plotted in Figure 3.8. Frequency-wavenumber plots for Tire 5 and Tire 7 are shown in Figure B.20 and B.21 respectively in Appendix B.

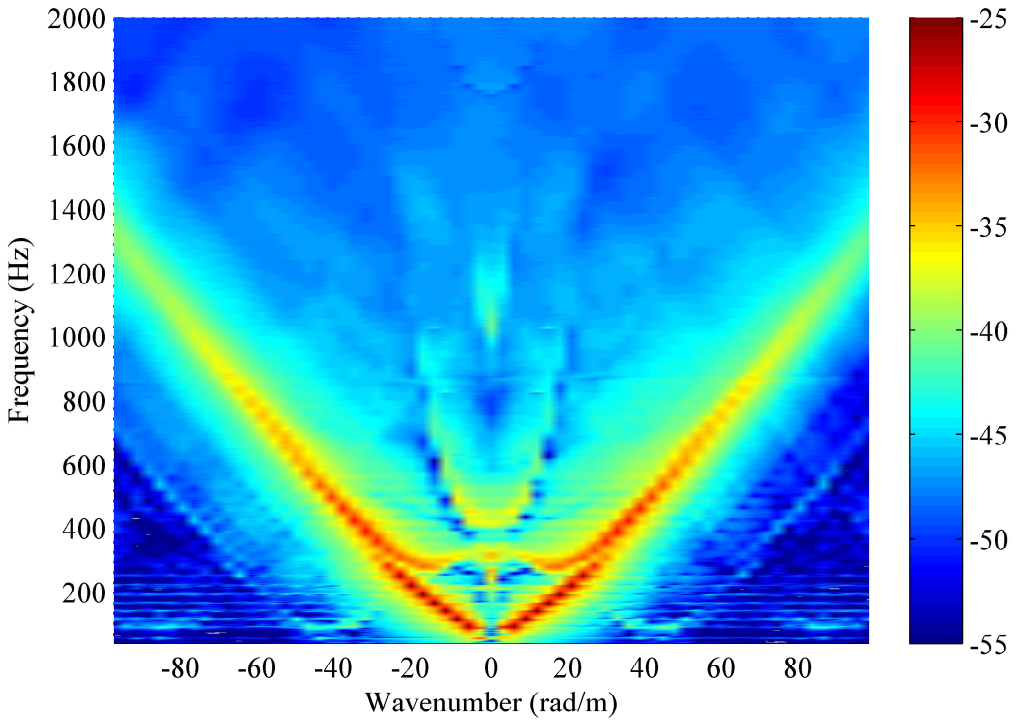

Figure 3.10. Frequency-wavenumber plot for Tire 8 from patch excitation.

Again, the low frequency content appears to be nearly identical between the two excitation methods. The 350 Hz - 800 Hz range has the slower moving wave, but the magnitude of the fast wave at the ring frequency appears to decrease. The higher order circumferential acoustic modes again appear around the same frequencies as the point excitation method. The wavenumber decomposed plots from the patch excitation with a beam do have some differences from the point excitation case. A fast moving wave around 1000 Hz - 1200 Hz appears much clearer with this method,

and around 1800 Hz another acoustic mode appears. This correlates strongly to a duct mode created by the air space between the tire carcass and the rim.

Figure 3.11 shows the first acoustic mode around 220 Hz, which should have a strong effect on the vibration potential because it exists at the $n = 1$ circumferential mode. The higher frequency duct mode plotted in Figure 3.12 should provide an increase in airborne noise.

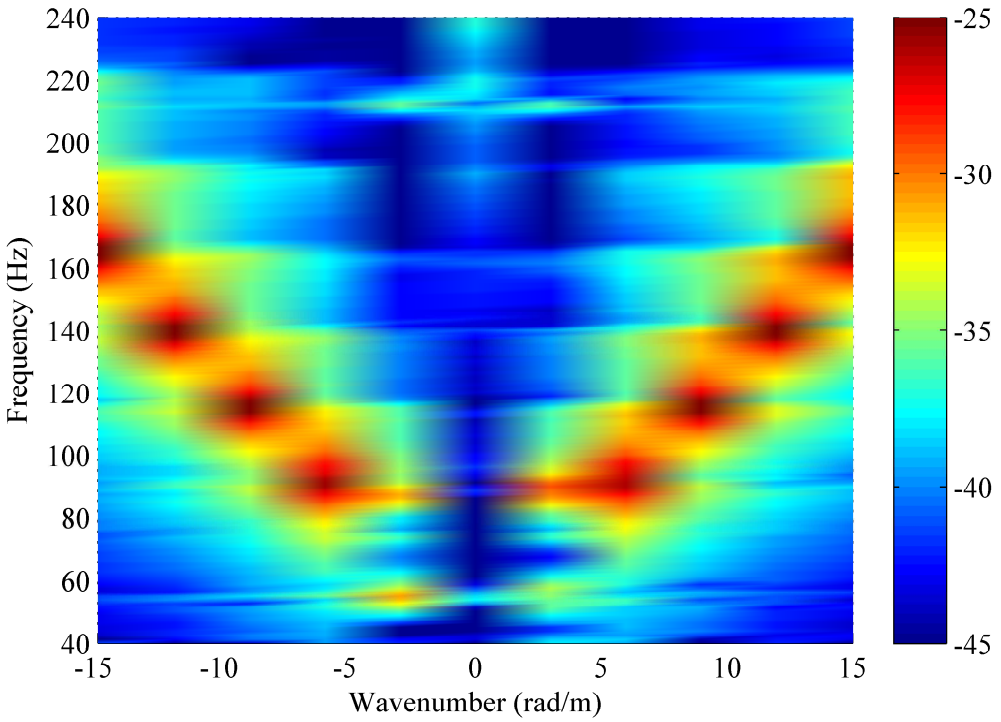

Figure 3.11. First acoustic mode for Tire 8 from patch excitation.

The variation in cut-on frequency and magnitude of the waves should account for differences in structure-borne noise spectra for each tire. Each waves' features also play a role concerning airborne noise, but since the potential is a summation of supersonic components, faster waves and duct modes should also have an influential contribution.

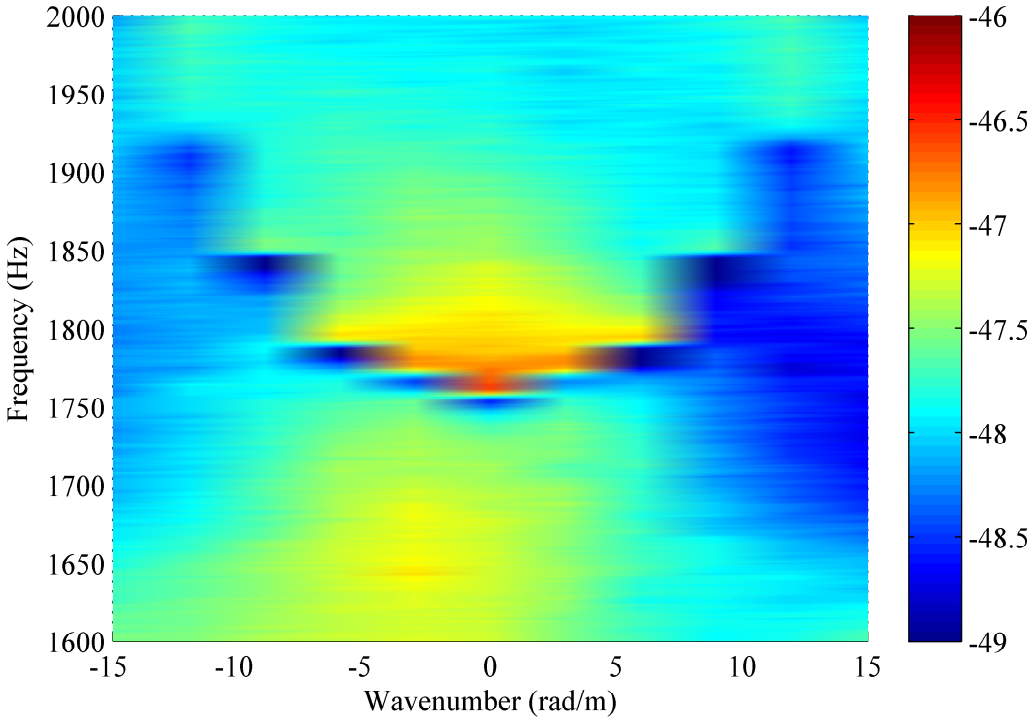

Figure 3.12. Air space duct mode for Tire 8 from patch excitation.

3.4.3 Vibration Potential

3.4.3.1 Spectral Analysis

The plot from the point excitation method in Figure 3.13 shows the spectral prediction of structure-borne noise for each tire.

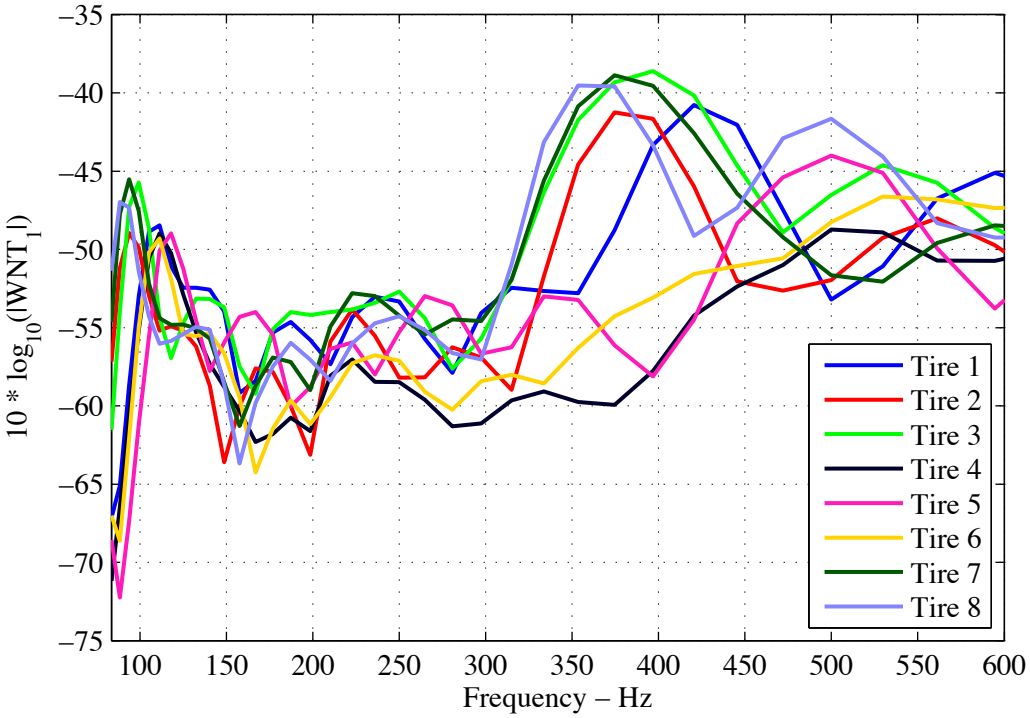

Figure 3.13. Structure-borne noise potential for the eight tires.

Peaks around 100 Hz would indicate the cut-on of the first flexural wave. The tires split into two groups for this feature with one below 100 Hz and the other above 100 Hz. Another grouping split appears around the ring frequency, 350 Hz - 500 Hz. The set of tires with peaks around 350 Hz - 400 Hz have similarities including manufacturer (4 of 5 Michelin) and cap ply type (4 of 5 Polyamide). The remaining tires that seem to peak around 500 Hz - 600 Hz have similar cap ply type (Nylon) and differ in manufacturer from the other group. These characteristics could provide

information related to material selection and tire construction concerning structure-borne noise.

After comparing the spectral data to the TPTA experiments, several questions are raised. First, the cut-on of the first flexural mode is not obvious in the TPTA normal acceleration measurements. This could be related to the shape of the transverse mode or be propagation effects. The vibration potential does not have a clear peak around the expected first acoustic mode. With close inspection of the frequency-wavenumber plots for each tire, it is visible. Finally, the ring frequency groups are appearing at frequencies above and below what were measured for their respective TPTA tests.

Figure 3.14 is a plot of the vibration potential plot from the patch excitation method for the three tires tested. The patch excitation method for the stationary

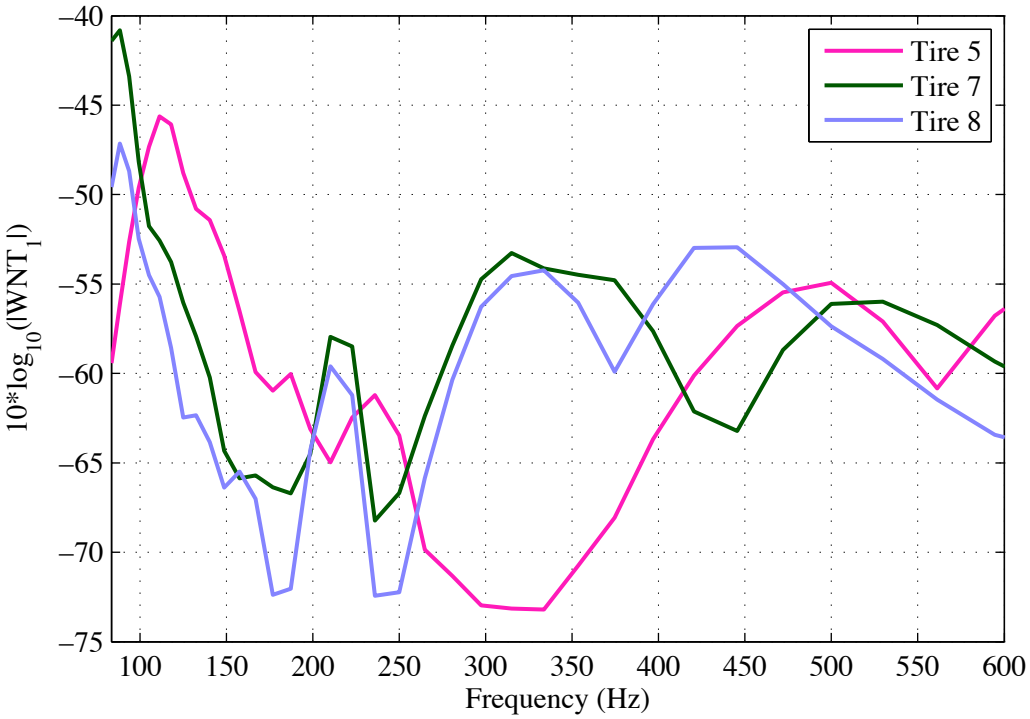

Figure 3.14. Structure-borne noise potential for the three tires from patch excitation.

tire test highlights several key features. The most prominent peak occurs around 100 Hz for all three tires. This is the cut-on of the first flexural mode and has not shifted in frequency compared to the point excitation vibration potential plot. Just above 200 Hz, the first acoustic mode now has a well defined peak. The levels for vibration potential around the ring frequency dropped drastically and shifted down in frequency slightly. This can be attributed to the higher order transverse modes no longer being excited because of the beam forcing. The patch excitation method for structure-borne noise prediction offers several key advantages over the point excitation method but cannot be determined as the only valid option until other factors are investigated.

3.4.3.2 Overall Level Analysis

To compare the stationary test results, an overall level was calculated for the vibration potential, and each tire was ranked loudest to quietest in Table 3.1.

Table 3.1. Vibration noise potential level of each tire for the defined spectra from point excitation force.

Rank	Tire	dB IL
1 (Loudest)	3	-33.2
2	8	-33.7
3	7	-33.9
4	1	-35.7
5	2	-36.5
6	5	-38.2
7	6	-39.4
8 (Quietest)	4	-40.7

Figure 3.15 shows a side-by-side comparison with lines drawn between the tires to show their difference in rank between the two tests. Measuring the accuracy of the

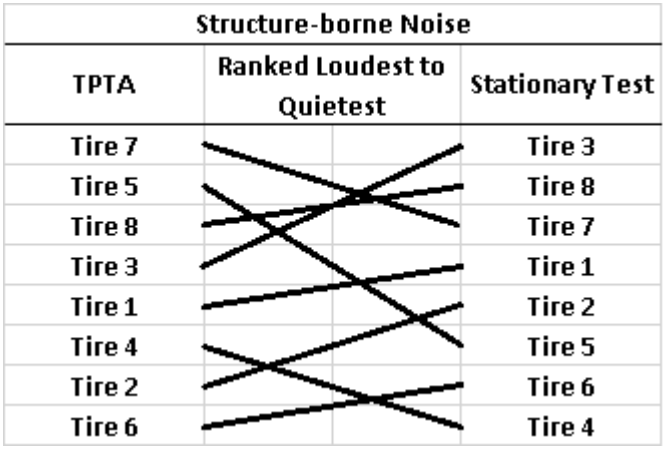

Figure 3.15. Comparison of the ranks between the two experiments.

stationary test in predicting a tire's structure-borne noise was determined using the differences between ranks of the tests in Equation 3.2:

$$d_{error} = \sqrt{\frac{(R_{TPTA_1} - R_{LDV_1})^2 + (R_{TPTA_2} - R_{LDV_2})^2 + ... + (R_{TPTA_N} - R_{LDV_N})^2}{N}} \tag{3.2}$$

with $R_{TPTA_n} = n$th tire's rank from the TPTA test, $R_{LDV_n} = n$th tire's rank from the stationary tire test, N = number of tires, and d_{error} = standard deviation between ranks with $d_{error} = 0$ as a perfect prediction. The d_{error} for structure-borne noise is 2.23. Therefore, the stationary tire test using the point excitation method misranked 66% of the tire's vibration potential by 2.23.

For the patch excitation method, Table 3.2 lists the ranks and the overall levels for structure-borne noise. A quick comparison to the TPTA vibration levels shows that the d_{error} equals 0. While only three tires were tested with this method, the re-ranking of tire 8 shows that the patch excitation may be more accurate in the prediction of the structure-borne noise for a tire.

Table 3.2. Vibration noise potential level of each tire for the defined spectra from patch excitation force.

Rank	Tire	dB
1 (Loudest)	7	-37.3
2	5	-39.4
3 (Quietest)	8	-41.7

3.4.4 Airborne Potential

3.4.4.1 Spectral Analysis

The plot from the point excitation method in Figure 3.16 shows the spectral prediction of airborne noise for each tire. The frequency range was limited to match the data from the TPTA.

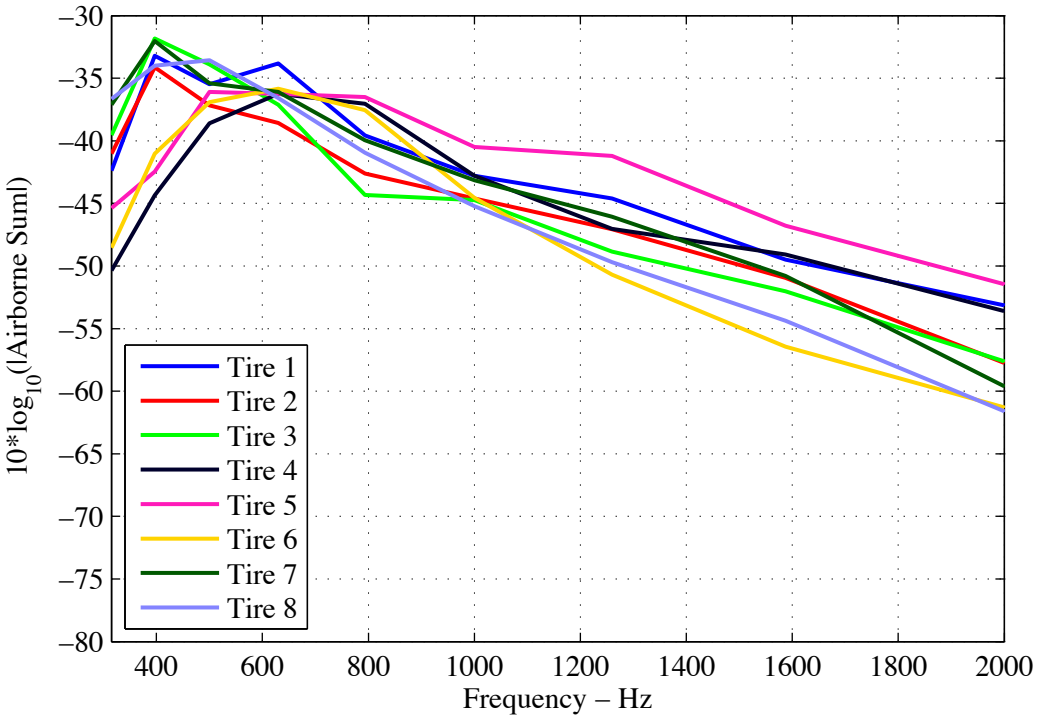

Figure 3.16. Airborne noise potential for the eight tires.

The sound radiation potential of the tires according to this method appears to decrease in level with increase in frequency after 400 Hz or 630 Hz. The range is related to the ring frequency cut-on for each tire. This spectral feature is similar to the TPTA measurements above 800 Hz. However, below 800 Hz, the TPTA measurements show a decrease in intensity as frequency decreases. Because the structure-borne

noise potential from patch excitation had lower levels around this frequency range, it is expected to have positive effects on the prediction of the airborne noise.

Figure 3.17 shows the sound radiation potential from the patch excitation method for the three tires tested. As expected, the results from the patch excitation method

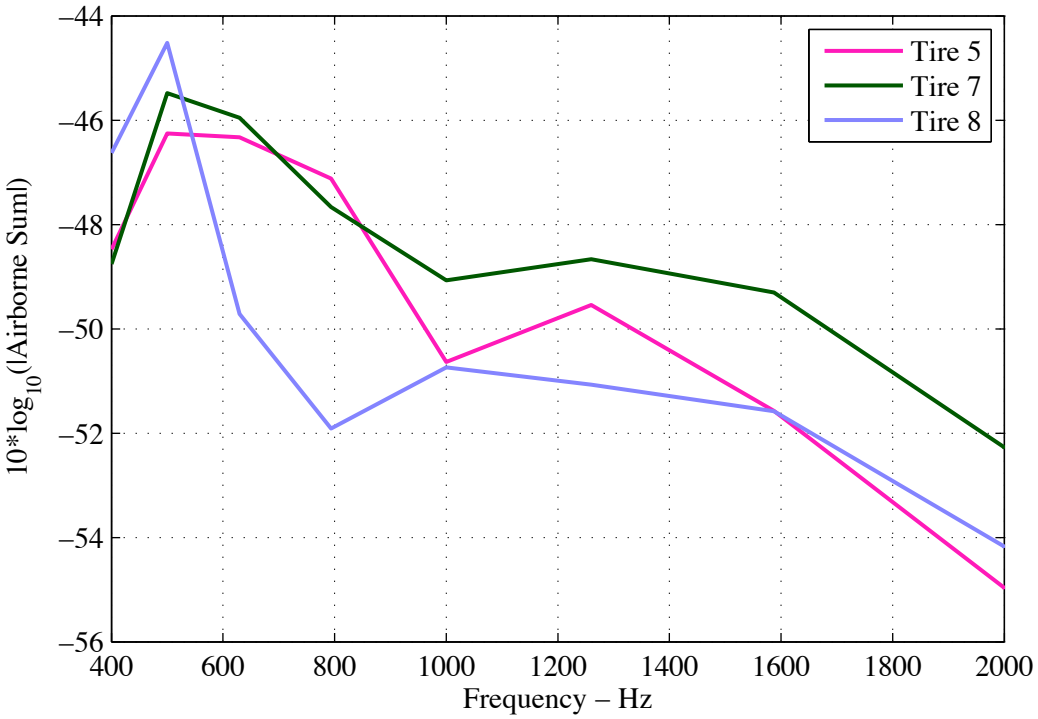

Figure 3.17. Airborne noise potential for three tires from patch excitation.

have a large decrease in level in the lower frequencies. Also, ranking at third-octave frequencies among the three tires is much closer to the TPTA intensity rankings than the point excitation method.

Neither method displayed the same spectral characteristics as the TPTA measurements. One missing component would be the horn effect, which has been shown to theoretically amplify specific frequencies by more than 20 dB [12–14]. The horn effect has been shown to vary based on distance away from the contact patch [13, 14]. As the distance increases, the effective peak frequency of amplification decreases. The

circumferential point mobility plots for each tire show that above 400 Hz, a majority of the energy is located near to the excitation force. This would result in the horn effect amplifying certain frequencies more than others. The differences between the airborne noise prediction and TPTA OBSI measurements could be altered by a generalized horn effect filter along with adjusting for speed.

3.4.5 Overall Level Analysis

Overall levels were calculated for the airborne potential, and each tire was ranked loudest to quietest in Table 3.3. A comparison of overall airborne noise potential between the two experiments is shown in Figure 3.18. As with the vibration potential, the accuracy of the prediction is not very high, and the d_{error} for airborne noise is 2.55.

Table 3.3. Airborne noise potential level of each tire for the defined spectra from point excitation force.

Rank	Tire	dB
1 (Loudest)	7	-27
2	3	-27.2
3	1	-27.3
4	8	-27.4
5	5	-29
6	2	-29.2
7	6	-29.9
8 (Quietest)	4	-30.4

The patch excitation method overall levels for airborne noise and tire ranks are listed in Table 3.4. Even though the d_{error} dropped to 0.81, the ranks of the tires compared to the same subset from the point excitation method did not change. Unlike the TPTA overall levels, a majority of the calculation is contributed by spectral

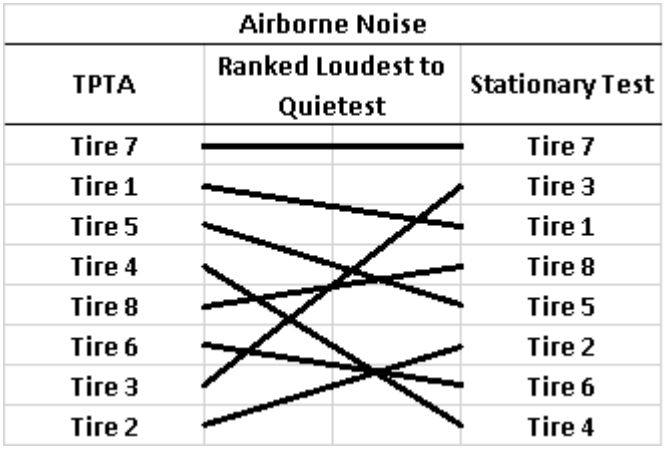

Figure 3.18. Comparison of the ranks between the two experiments.

content below 800 Hz. This could be accounted for by speed variation and/or a radiation modification filter based on the horn effect.

Table 3.4. Airborne noise potential level of each tire for the defined spectra from patch excitation force.

Rank	Tire	dB
1 (Loudest)	7	-36.9
2	8	-38.1
3 (Quietest)	5	-38.6

3.5 Summary of Structural Wave Propagation

The analysis of structural wave propagation on a tire was successful using the stationary tire test. Wavenumber decomposed results showed the variations in wave groups for the eight tires. The vibration potentials for the eight tires appear to show some consistency spectrally with the measurements from the TPTA experiment. The differences in peaks could be accounted for by addressing effects found based on automobile speed. Overall level comparison was helpful in ranking the tires, but the first flexural mode appears mostly responsible for the ranks with the patch excitation method. Because this feature is not so obvious in the TPTA measurements, the low frequency limit for analysis and structure-borne noise prediction may need to be adjusted. Airborne potentials for the eight tires suffered from the ring frequency dominating the spectral prediction. An adjustment with speed might help with ranking the tires' overall levels, but likely will not help with the spectral content since no variation was seen with varying speed in the TPTA experiment. The low frequency limit for the airborne potential will also have to be changed or it will be necessary to identify another radiation efficiency factor for the tires besides group phase speed.

4. MOVING INPUT FUNCTION

4.1 Introduction

Some similarities existed between the stationary test noise predictions and TPTA measurements. However, the speed variation showed that the spectra of the structure-borne noise changes with automobile velocity as does the overall level of the airborne noise. Since the noise predictions were calculated from the tire's natural response, a modification is needed to accurately compare the stationary tire experiment data with the TPTA data. A very regular tread pattern could create a tread passage frequency, which would enhance certain response characteristics of each tire. After examining the tires, it was noted that tire manufacturers do attempt to randomize their patterns to prevent the pure tone of a tread passage frequency from occurring. However, since a tire has a finite circumference and tread size/spacing is also optimized for traction and stability, the amount of randomization is limited.

It was suggested to add the effect of a spatial window from contact patch features to the circumferential point mobility before wavenumber decomposition. This modification would amplify or decrease the transformed data based on the input force over the designated area. A simplification of the tread features was required to implement this concept. The part of a tread block that comes into contact with the road was given a value of 1, while the circumferential grooves and transverse sipes were assigned to be 0. While this created a slight a variation on noise potential, a further investigation was proposed to have the tire move through the contact patch to add a temporal aspect to the spatial windowing.

4.2 Theory

A tire can be divided into spatial points using Equation 4.1:

$$\Delta x = \frac{v}{FS} \tag{4.1}$$

with FS as the temporal sampling frequency and v as the velocity of the tire. This created a synchronized advancement of points in both space and time. The division of the tire, Figure 4.1, created sections with tread blocks, sipes, and grooves.

Figure 4.1. Δx section of tire tread.

The area of the "On" portion was calculated and divided by the total sectional area. Completing this circumferentially resulted in a vector of values between 0 and 1. These values represented the amount of input to a tire a section contributed transversely when the entire section of the tire was in contact with the road.

However, because contact patches are rarely perfect rectangles, the circumferential spatial values were modified as they moved through the contact patch with a spatial window. The spatial window was defined using the footprint of a tire. An example of a footprint and the resulting window are shown in Figure 4.2.

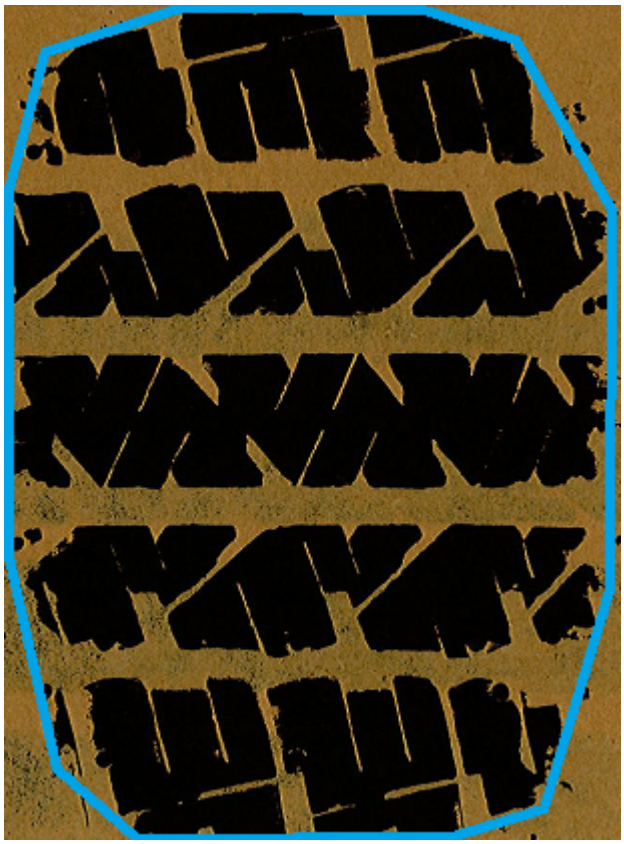

Figure 4.2. Footprint for tire 7 with outline of spatial window.

This spatial window expanded the circumferential vector to a matrix with each column being a spatial point's input value varied through the contact patch. An example matrix is provided in Table 4.1.

The temporal aspect of this method was added next by taking a spatial snapshot of the values as the tire rotated through this contact patch. The value of points outside of this contact patch as a tire rotated were set to zero since no force is applied. A snapshot is shown in Figure 4.3.

Table 4.1. Spatial input values windowed by the contact patch.

		Circumferential Spatial Point						
		1	2	3	...	2520	2521	2522
Contact Patch	1	0.186	0.357	0.351		0.386	0.375	0.346
	2	0.190	0.367	0.363		0.398	0.387	0.358
	3	0.200	0.374	0.364		0.407	0.396	0.368
	...							
	67	0.393	0.702	0.679		0.684	0.677	0.640
	68	0.393	0.702	0.679		0.684	0.677	0.640
	69	0.393	0.702	0.679		0.684	0.677	0.640
	...							
	133	0.200	0.374	0.364		0.407	0.396	0.368
	134	0.190	0.367	0.363		0.398	0.387	0.358
	135	0.186	0.357	0.351		0.386	0.375	0.346

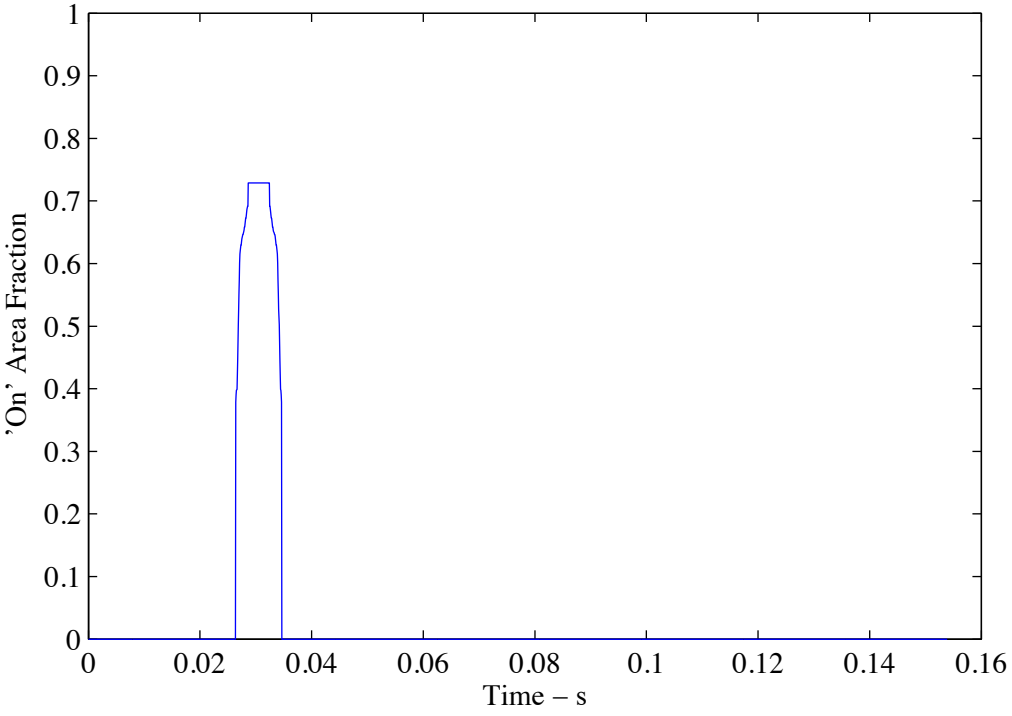

Figure 4.3. Spatial point 500 amplitude change through time.

The figure highlights when a specific spatial point is applying a force in time to the tire and the magnitude of the force due to the spatial window from the tire footprint.

By advancing through a single revolution of a tire, one creates a matrix with varying values spatially and temporally. A wavenumber decomposition was performed for each snapshot. Then, a Fourier transform through time was conducted at each wavenumber to end with an input function that could be overlaid on the wavenumber decomposed circumferential point mobility of a given tire to modify the response according to vehicle velocity.

4.3 Experimental Analysis

Multiple methods for obtaining tread information were attempted including 3D scanning and physical measurement of tread blocks. The procedure that provided the best output involved image analysis of a tire track. The Firestone FR710 was used for comparison with previously presented speed varying data.

The tire was mounted onto the TPTA. Kraft paper was taped over the smooth pavement sample. The tire was painted black and loaded to 720 lbs. Then, it was pushed manually over the entire pavement sample before being unloaded. The result was a tire track displaying the circumferential tread pattern. The paper was cut into 11 x 17 sections and scanned into the computer. Some cropping and touch-up work was required before importing the images into MATLAB and reconstructing the tire. Figure 4.4 shows the reconstructed tread pattern.

After sampling a single revolution in space and time using the aforementioned theory, a frequency-wavenumber plot, shown in Figure 4.5, can be created. The plot has several lines overlaid for analysis. The white line is a slope set at 30 mph, which lines up exactly with a wave. The magenta lines are set at the speed of sound, 340 m/s, to visualize how the data would affect the tires' wavenumber decomposed data. The moving input appears to have spectral content that will impact airborne and structure-borne noise.

Figure 4.4. Reconstructed tire tread pattern in MATLAB.

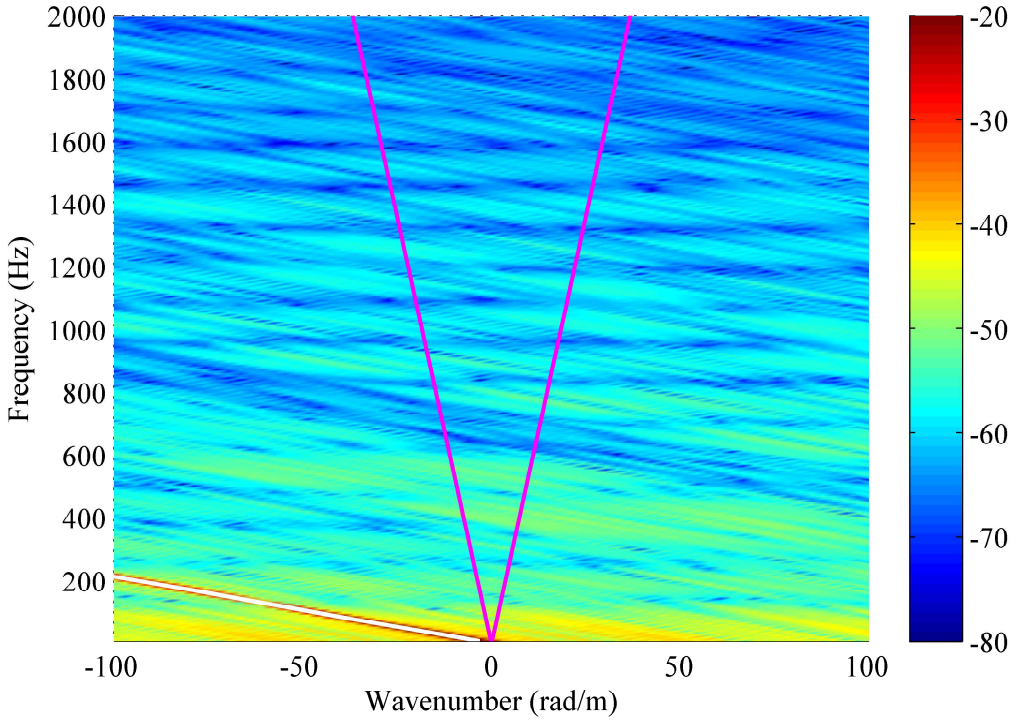

Figure 4.5. Frequency-wavenumber plot from moving input tread force.

To verify if a change in speed could have an effect, the procedure was repeated in 5 mph increments. Figure 4.6 is a plot of the impact the moving input would have on the vibration potential for noise with a variation in speed. Similar to the normal accelerometer measurements from the TPTA experiment, a series of peaks decreases in frequency as the speed decreases. This feature suggests that the moving input or another similar speed dependent force affects the natural response of the tire. As peaks and valleys shift in frequency, they could amplify or remove tire vibration characteristics at specific speeds. For spectral comparison to the TPTA experiment, the energy of the patch excitation and moving input vibration potentials were normalized. Figure 4.7 demonstrates the effectiveness of the moving input at shaping the stationary tire test results to match the speed of the TPTA data.

Figure 4.8 shows the impact the moving input would have on the airborne potential with a variation in speed. Across the frequency range of interest, the moving input function will not help shape the airborne potential to be similar to the TPTA results. However, increasing the speed of the moving input function appears to raise the overall level of the airborne noise potential. A plot of the spectrum level vs. log(speed) in Figure 4.9 shows a linear increase in level with the log(speed) quite similar to the overall sound intensity level data. A standard filter could be applied to the input function to mimic the radiation efficiency seen in the TPTA measurements.

4.4 Theoretical Analysis

While the moving input method appears to have a positive effect on the noise spectra, some theoretical extremes of tire tread patterns need to be investigated to strengthen the hypothesis.

Two tire track images were created using MATLAB. The size and circumferential grooves from the Firestone FR710 were used in both to provide a basis and some similarity to the experimental analysis. The first image contained a transversely uniform

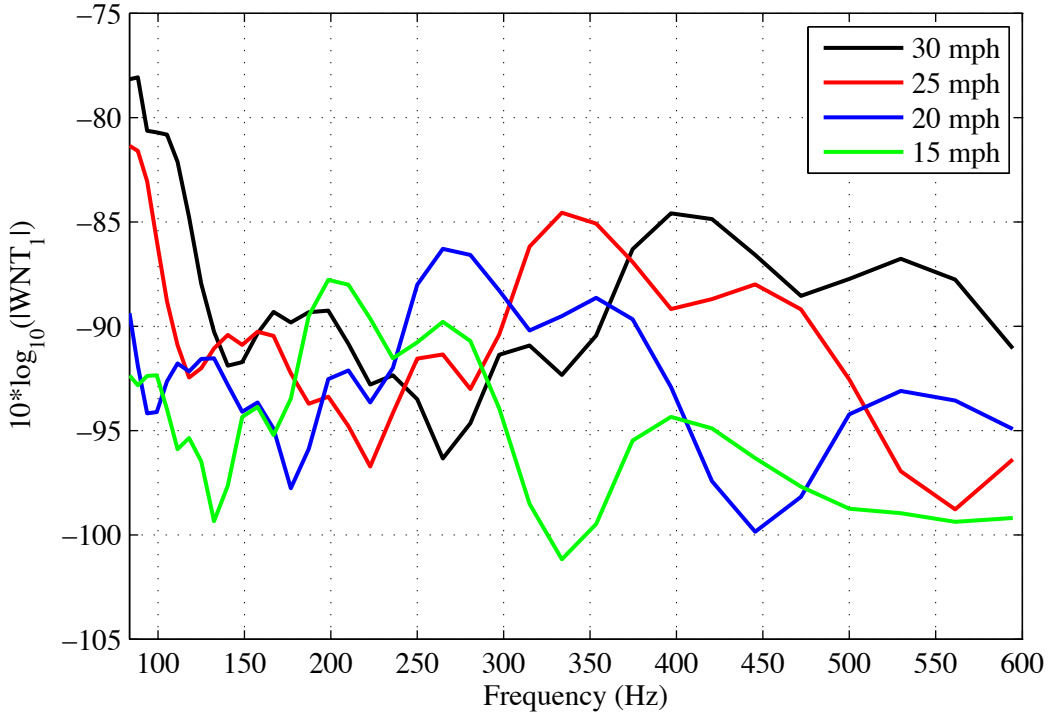

Figure 4.6. Moving input force vibration potential spectrum.

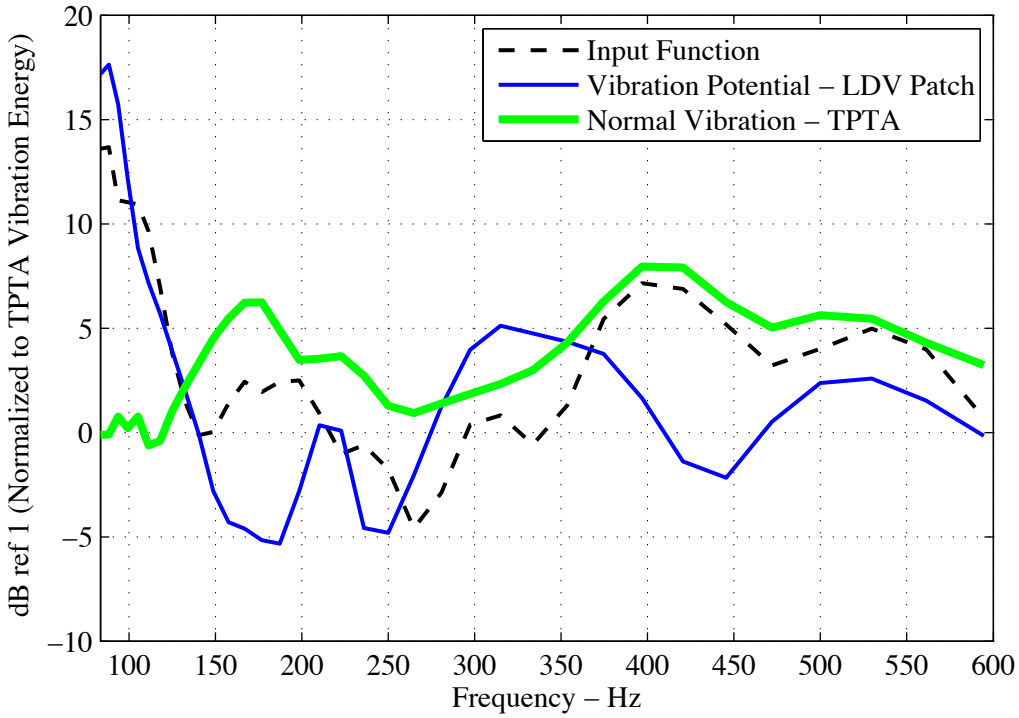

Figure 4.7. Moving input force vibration potential spectrum.

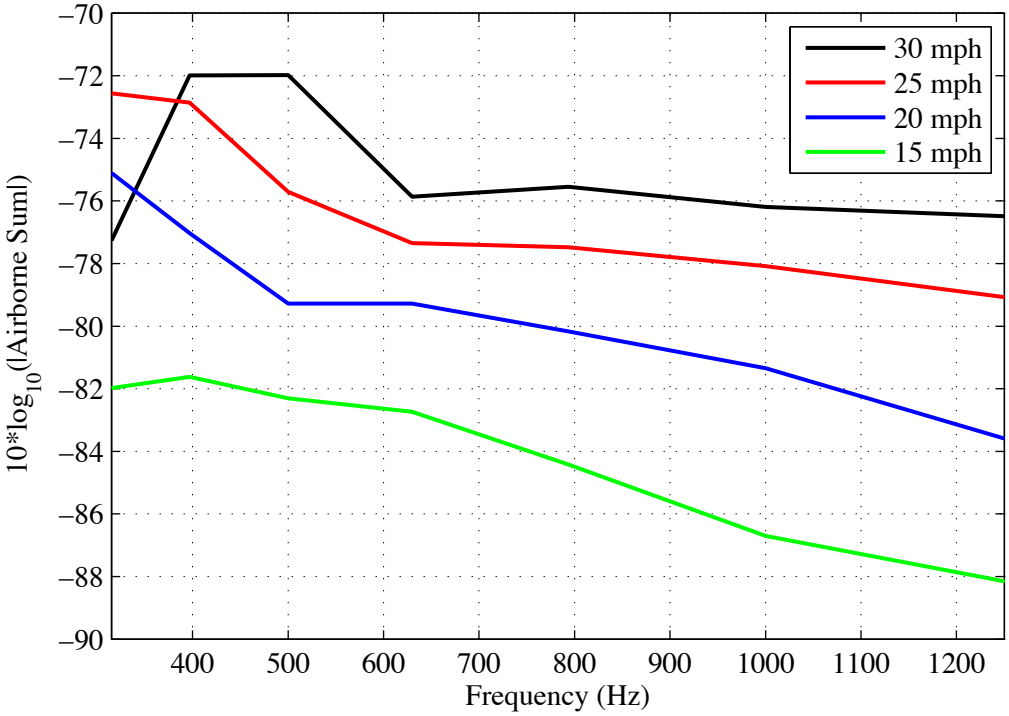

Figure 4.8. Moving input force airborne noise potential spectrum.

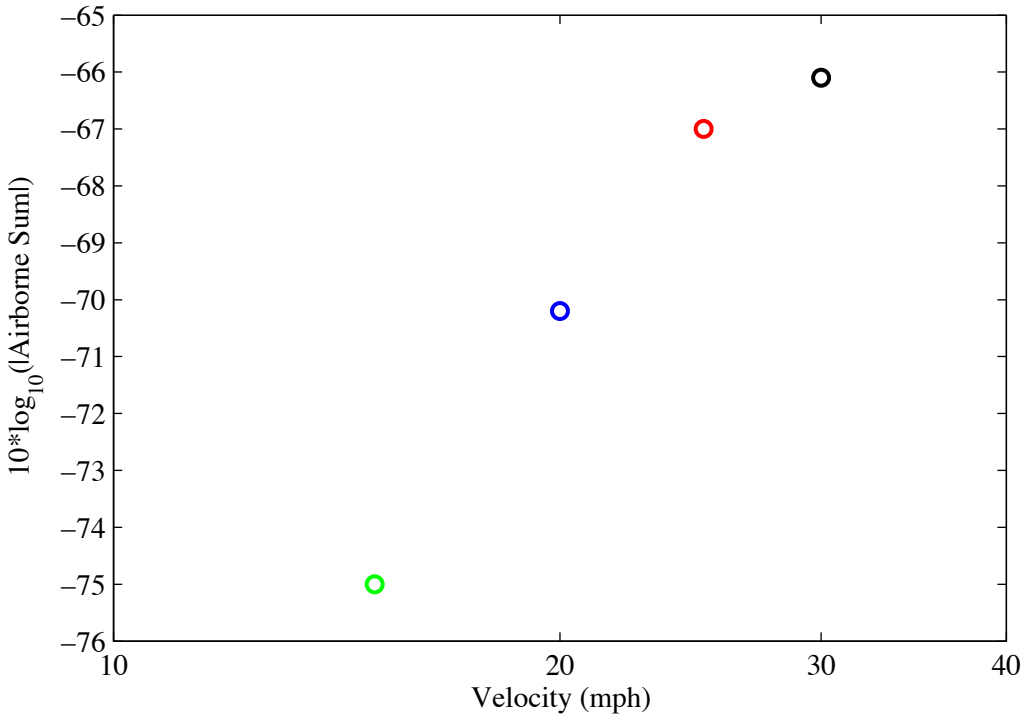

Figure 4.9. Airborne spectrum level vs. speed for Tire 7 using the moving input.

periodic tread block pattern. The second was created by normally randomizing tread block length and width. Figure 4.10 shows the theoretical track images.

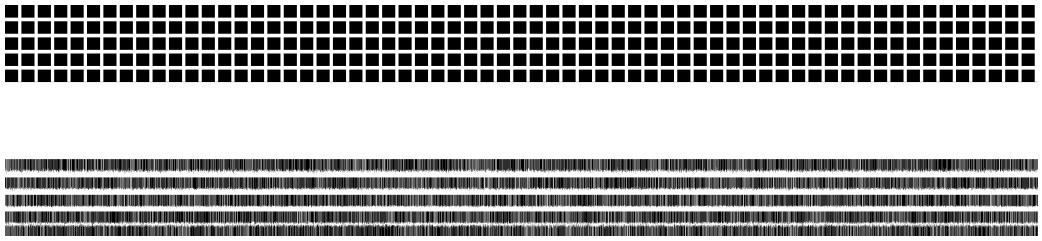

Figure 4.10. Periodic tread pattern (top) and random tread pattern (bottom).

These tracks were developed to analyze the two extremes of tread pattern design to verify if the experimental moving input was reasonable. After a wavenumber decomposition, the random pattern should have small variation in amplitude throughout the frequency-wavenumber spectra. Assuming a speed of 30 mph and tire circumference of 2 m, the angular velocity was calculated to be 6.7 rps. With a periodic pattern containing 63 tread blocks, an increased amplitude was expected at approximately 422 Hz. Figures 4.11 and 4.12 show the wavenumber decomposed results for the periodic and random tread patterns, respectively.

The frequency-wavenumber plots show similarities and differences between the patterns. Both have a "wave" extending from 0 rad/m and 0 Hz at a slope of 30 mph.

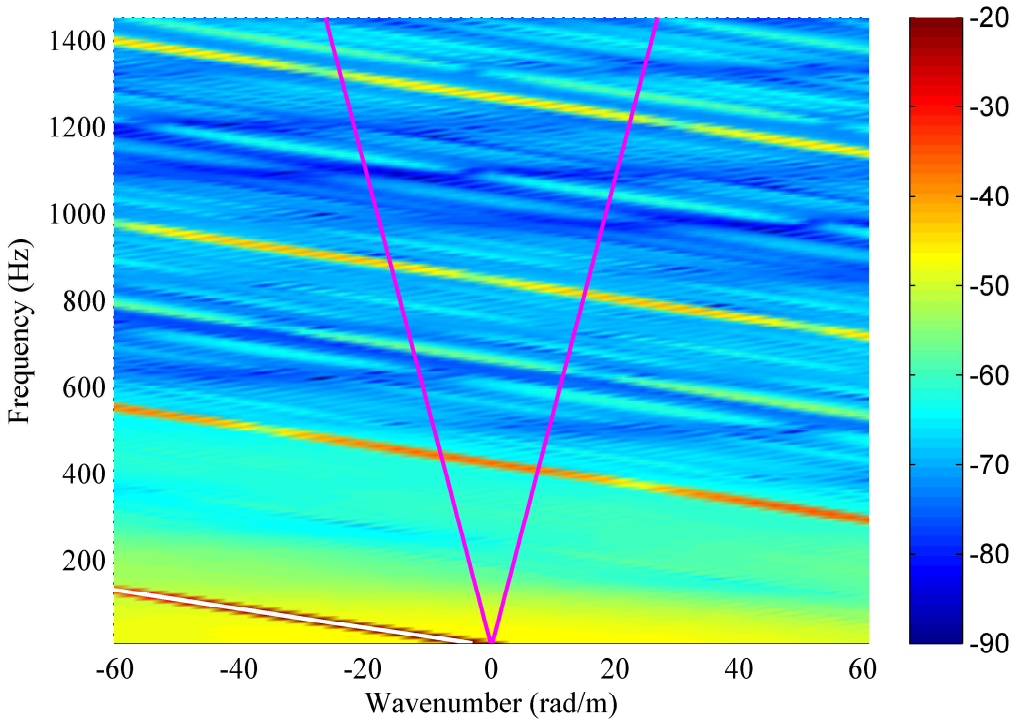

Figure 4.11. Frequency-wavenumber plot for the periodic tread pattern.

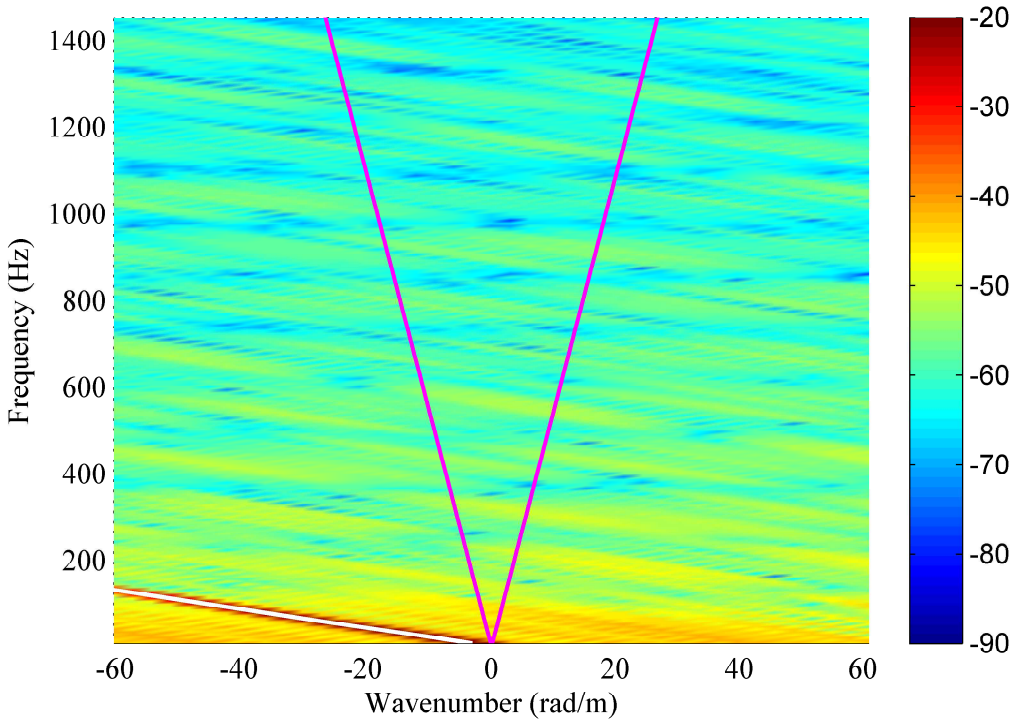

Figure 4.12. Frequency-wavenumber plot for the random tread pattern.

The random pattern spectra appears to contain random noise throughout while the periodic pattern spectra has a clearly defined slope running through 420 Hz.

Figure 4.13 shows the vibration potential of each pattern as calculated from the wavenumber decomposed circumferential point mobility of the tires. Clearly the periodic pattern exhibits a large increase in level around 422 Hz. While the random pattern has some peaks and valleys, they vary much less in level and look more like general noise.

For the airborne noise potential, the periodic pattern has the 422 Hz feature as well as what appeared to be harmonics in the wavenumber decomposition plot. The random pattern has no significant spectral content and has an overall lower level.

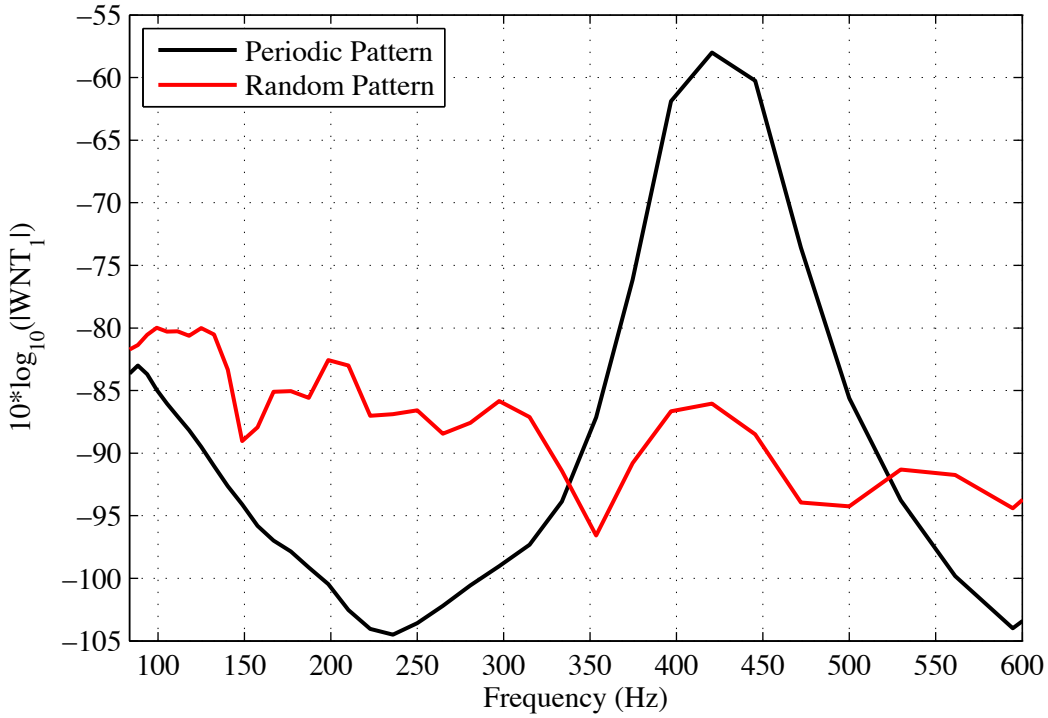

Figure 4.13. Moving input force vibration potential spectra for two theoretical tread patterns.

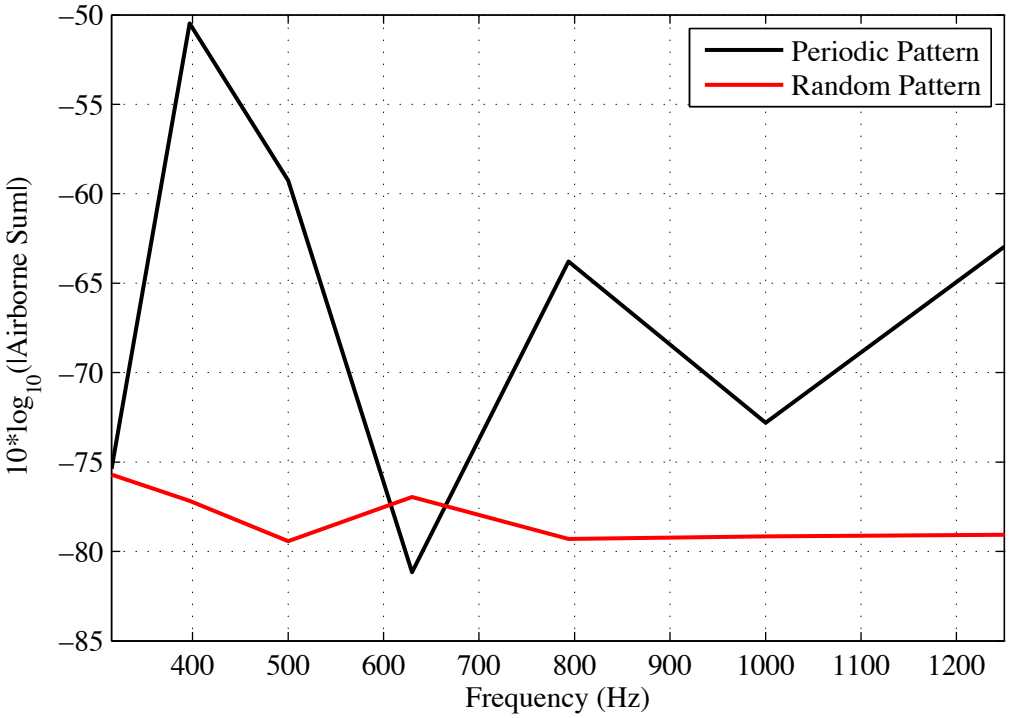

Figure 4.14. Moving input force airborne potential spectra for two theoretical tread patterns.

4.5 Summary of Moving Input Function

The moving input function developed in this chapter was based on tread patterns for a tire and automobile velocity. By using a painted tire track, the image analysis and signal processing combined to output an input that could modify the tire's noise potential from the stationary tire test. For structure-borne noise, the results have similar spectral content related to the TPTA normal acceleration. The main features also shift down in frequency with decreasing speed. The airborne noise also saw a shift in frequency content, but, more importantly, a linear vs logarithmic velocity relationship was found. The theoretical tire tread patterns suggest that an extremely regular tire tread will have profound effects on the structure-borne noise at the tread passage frequency. The random pattern does not appear to have an impact on vibration potential. The periodic pattern should also affect the spectral variation of airborne noise, but the higher level across the spectrum compared to the random pattern would have a greater influence when combined with the airborne potential from the stationary tire test. This method should be investigated further as it could have a unique impact on the prediction of a tire's noise potential.

5. RELATIVE TIRE NOISE POTENTIAL MODEL

5.1 Introduction

The stationary tire test and moving input function analysis offered insight into the prediction of airborne and structure-borne noise of a tire. A second set of tires was collected from an automobile OEM to analyze the effectiveness of the combined methods into a single model.

5.2 Tires Tested

The tires tested were chosen by the automobile OEM based on an in-house test. Noise measurements were recorded within the cabin of a vehicle running on a test track at 80 kph (49.7 mph). The difference between tests was the tires so it is assumed that the spectrum differences were only related to tire noise. A list of the tires is provided in Table 5.1.

The data for the full third-octave spectrum is plotted in Figure 5.1. The automobile OEM defines airborne (A/B) noise as A-weighted from 630 Hz - 3150 Hz third-octave bands. Structure-borne (S/B) noise is A-weighted 60 Hz - 300 Hz narrow band and plotted in Figure 5.2. The tires were selected because they represented high, medium, and low performance concerning airborne and structure-borne noise. Tables C.1 and C.2, in Appendix C, rank the tires according to their airborne and structure-borne noise results, respectively.

Table 5.1. List of Tires Tested.

Tire	Manufacturer	Tire Code	Identifying Type	Inflation Pressure	Tread Plies
9	Goodyear	215/60 R16	Assurance Fuel Max	32 PSI	Tire: 2 Polyester, 1 Nylon, 2 Steel Sidewall: 2 Polyester
10	Michelin	P215/55 R17	Energy MXV4 S8	32 PSI	Tire: 2 Polyester, 1 Polyamide, 2 Steel Sidewall: 2 Polyester
11	Pirelli	P245/45 R17	P6 (Four Seasons)	32 PSI	Tire: 2 Rayon, 2 Steel, 2 Nylon Sidewall: 2 Rayon
12	Bridgestone	225/45 R19	Potenza RE050A	33 PSI	Tire: 2 Rayon, 2 Steel, 1 Nylon Sidewall: 2 Rayon
13	Bridgestone	255/35 R19	Potenza RE050A	33 PSI	Tire: 1 Rayon, 2 Steel, 2 Nylon Sidewall: 2 Rayon

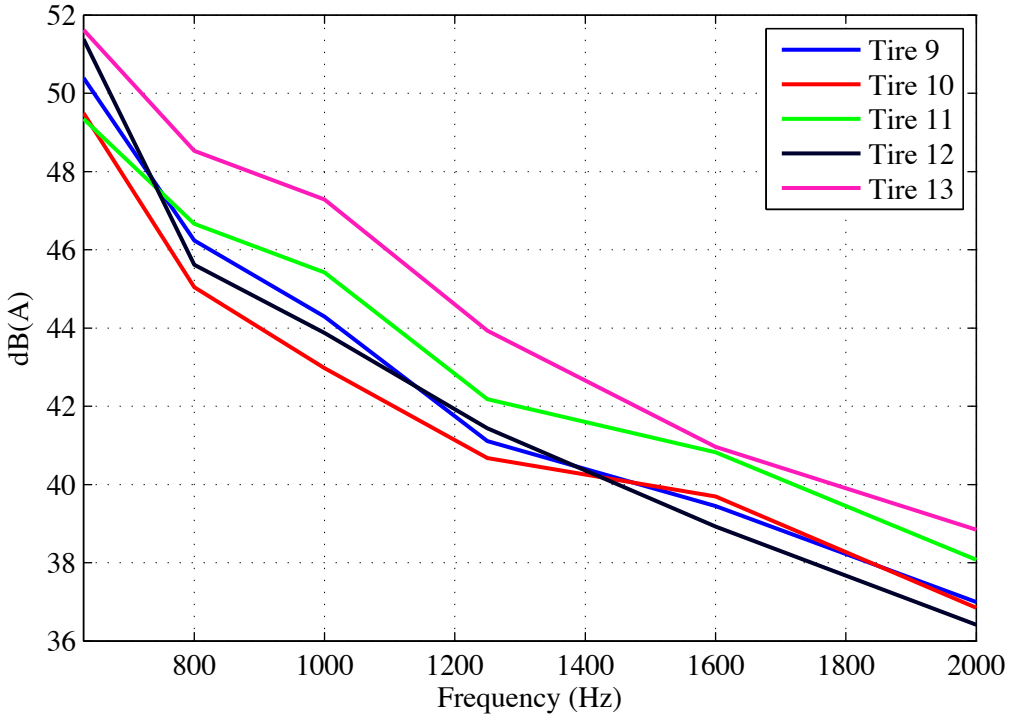

Figure 5.1. Full spectrum third-octave noise measurements from the interior of a car of 5 tires.

5.3 Procedure

A new test stand, Figure 5.3, was provided by the automobile OEM and designed to have no significant vibrational modes below 2 kHz. Each tire was sprayed with the Magnaflux Spotcheck Developer SKD-S2 before conducting the stationary tire test with the patch excitation forcing method. A wavenumber decomposition was used on the measured point mobilities.

For the moving input function, each tire was mounted onto the TPTA. Kraft paper was taped over the smooth pavement sample. The tire was painted for the initial contact patch before loading it to 720 lbs. The TPTA was manually rotated while paint was applied to the treads. The tire was unloaded and tread pattern

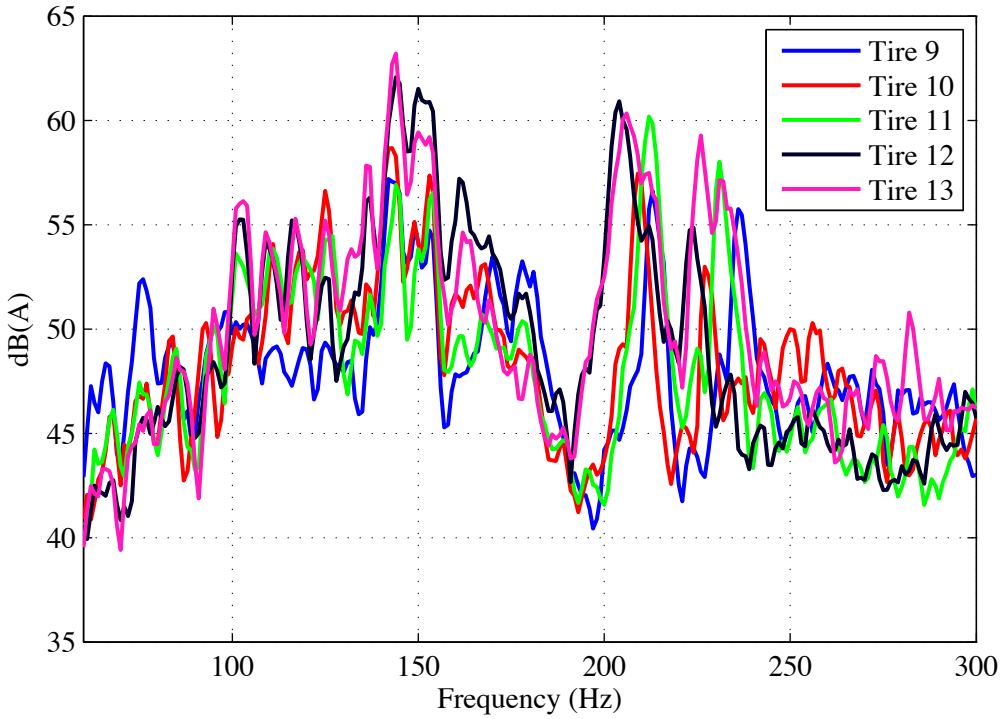

Figure 5.2. Structure-borne narrow band noise measurements from the interior of a car of 5 tires.

Figure 5.3. New test stand for conducting laser vibrometer measurements with the patch excitation method.

removed. A smaller piece of Kraft paper was then attached to the pavement, and the tire painted over a section. The load was applied and removed after 10 seconds to leave a clean footprint for each tire. The tread pattern was cut into 11 x 17 in. sections for scanning.

After scanning the tire images, the footprint was measured to set-up the spatial window for each tire. In MATLAB, the reconstructed tread patterns were run through the moving input function with a velocity of 80 kph (49.7 mph) for a single revolution. Since the frequency spectrum would not align, the moving input data was A-weighted and third-octave/twelfth octave filtered for the airborne and structure-borne potentials, respectively. The filtered spectra were multiplied by the noise potentials from the stationary tire tests' wavenumber decomposed data. A calculation of overall levels was performed in the frequency range of interest defined by the automobile OEM.

5.4 Results and Analysis

The circumferential spectral plots and frequency-wavenumber plots for each tire are shown in Appendix C, Figures C.1 to C.10. While calculating the airborne and structure-borne noise potential for the tires using the methods from Chapter 3, an A-weighting filter was applied.

5.4.1 Airborne Potential

5.4.1.1 Spectral Analysis

Figure 5.4 is the third-octave filtered airborne noise prediction for the five tires using the frequency range of interest from the automobile OEM. A comparison of the provided noise data with the stationary tire test processed results shows very little similarities. However, the higher speeds of the automobile OEM test will cause the moving input function spectral content to shift to higher frequencies, likely in the range of interest for airborne noise. Figure 5.5 shows the speed modified airborne

noise prediction. The general decrease in level with increasing frequency corresponds to the trend seen in the automobile OEM data. The rankings across the spectrum have also changed.

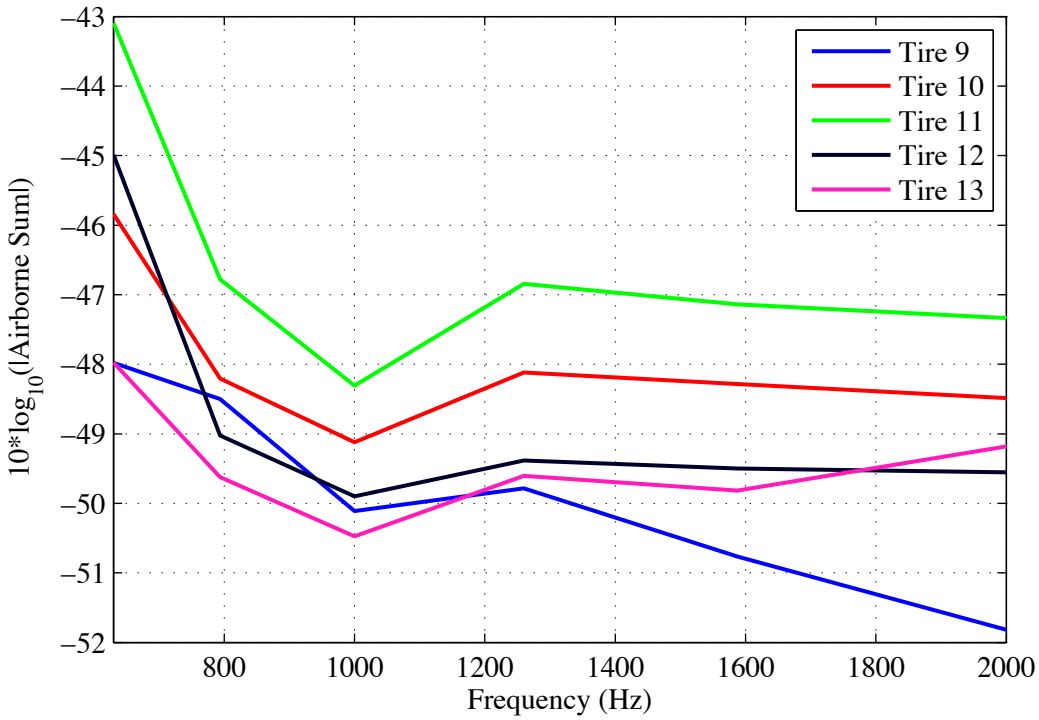

Figure 5.4. Airborne noise potential for five tires from patch excitation.

5.4.1.2 Overall Level Analysis

The use of the moving input function in combination with the stationary tire test data provides noticeably improved results. A comparison of the ranks between the two data sets without the moving input function is shown in Figure 5.6. The d_{error} is 2.41. The moving input function reduces the d_{error} to 1.67. Figure 5.7 shows the ranked comparison. Recalling the results from the TPTA experiment, the levels at 800 Hz were the peaks for almost all the tires and across various speeds. The

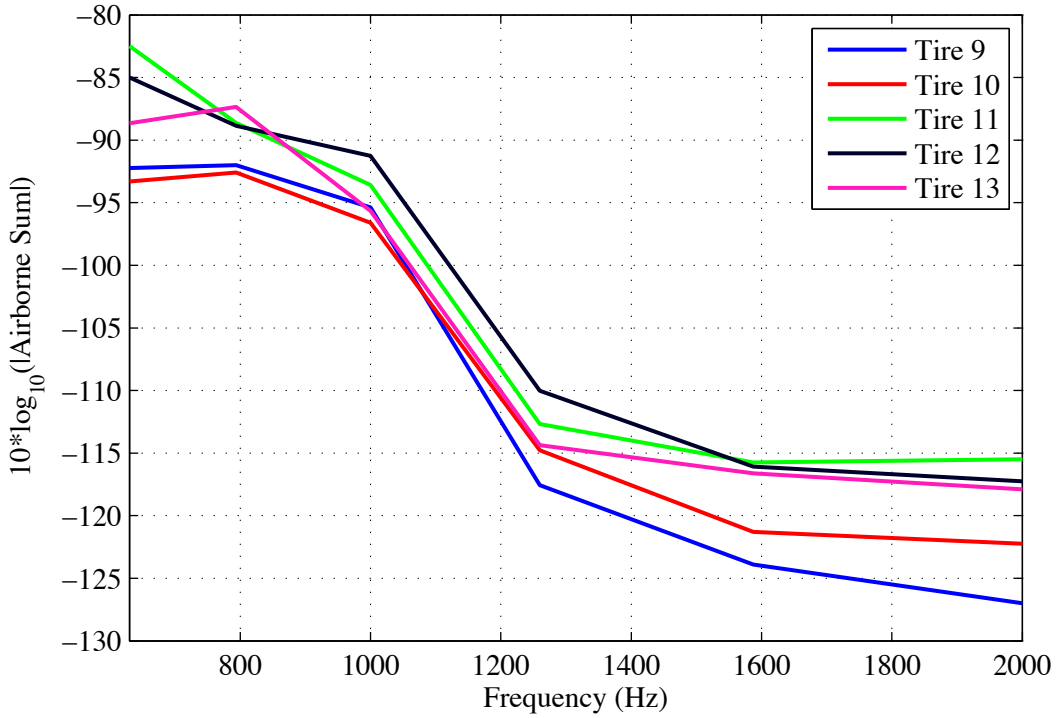

Figure 5.5. Airborne noise potential for five tires from patch excitation modified by the moving input function at 80 kph.

measurements from the automobile OEM airborne data, however, have high levels at the 630 Hz third-octave band. Recent operational transfer path analysis performed concerning cabin and tire noise has found that for a certain vehicle structure-borne noise dominates below 700 Hz and airborne noise above 700 Hz [15]. The previous analysis suggests that the overall airborne noise predictions should be recalculated assuming that the airborne summation is applicable above 800 Hz. A new comparison is shown in Table 5.8, and this assumption reduces the d_{error} to 1.10. The combination of the two methods can accurately order the airborne noise potential of five tires from loudest to quietest with an error of only one rank.

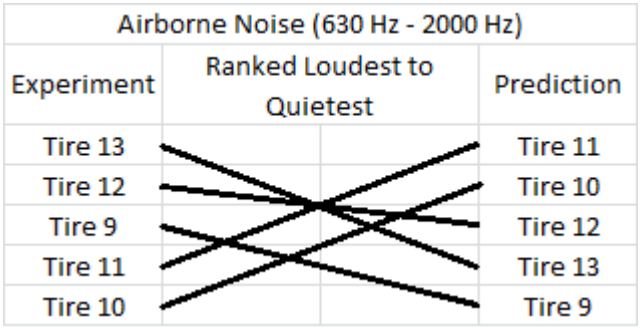

Figure 5.6. Overall airborne noise level comparison between experimental data and prediction (without moving input).

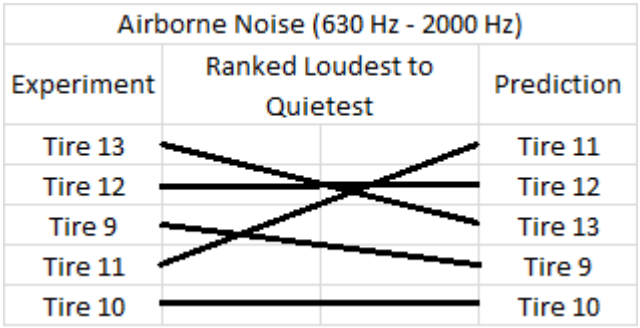

Figure 5.7. Overall airborne noise level comparison between experimental data and prediction (with moving input).

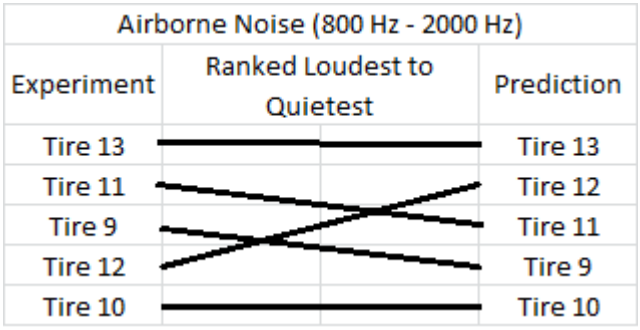

Figure 5.8. Overall airborne noise level comparison between experimental data and prediction.

5.4.2 Vibration Potential

5.4.2.1 Spectral Analysis

The narrow band A-weighted structure-borne noise prediction for the five tires is plotted in Figure 5.9. One interesting feature to note from comparing the structure-borne noise results is around 210 Hz where the first acoustic mode is usually located. The narrow band data shows two peaks separated in frequency by relatively the same bandwidth for each tire. Cao and Bolton suggested that the rotating aspect of the tire and air flow within causes a split in the positive and negative wave propagating away from the drive point [16]. An enhanced view of this frequency range for the two results in Figure 5.10 shows that the acoustic mode appears to divide into two separate peaks at frequencies above and below the peak in the stationary tire test. Apart from these peaks around the first acoustic modes, the spectral content of the automobile OEM provided data and the stationary tire test with patch excitation are quite different in this frequency range. Some notable features including the first flexural modes show up but are at significantly lower levels in the automobile OEM data. The inclusion of the moving input function in Figure 5.11, does little to improve the structure-borne noise prediction spectrally and appears to modify the levels across the spectrum incorrectly. The upper frequency limit of the automobile OEM data was increased to 600 Hz to examine additional spectral content. Plotted in Figure 5.12, the frequency range of focus for their ranking is understood since the largest peaks occur in the 60 Hz - 300 Hz region. The vehicle could be acting as a filter and reducing the influence of the 300 Hz - 600 Hz range that appeared to be a major contributor in the TPTA results.

5.4.2.2 Overall Level Analysis

Figure 5.13 is the predicted overall structure-borne noise from the stationary tire experiment with patch excitation for 60 Hz - 300 Hz. The prediction of overall

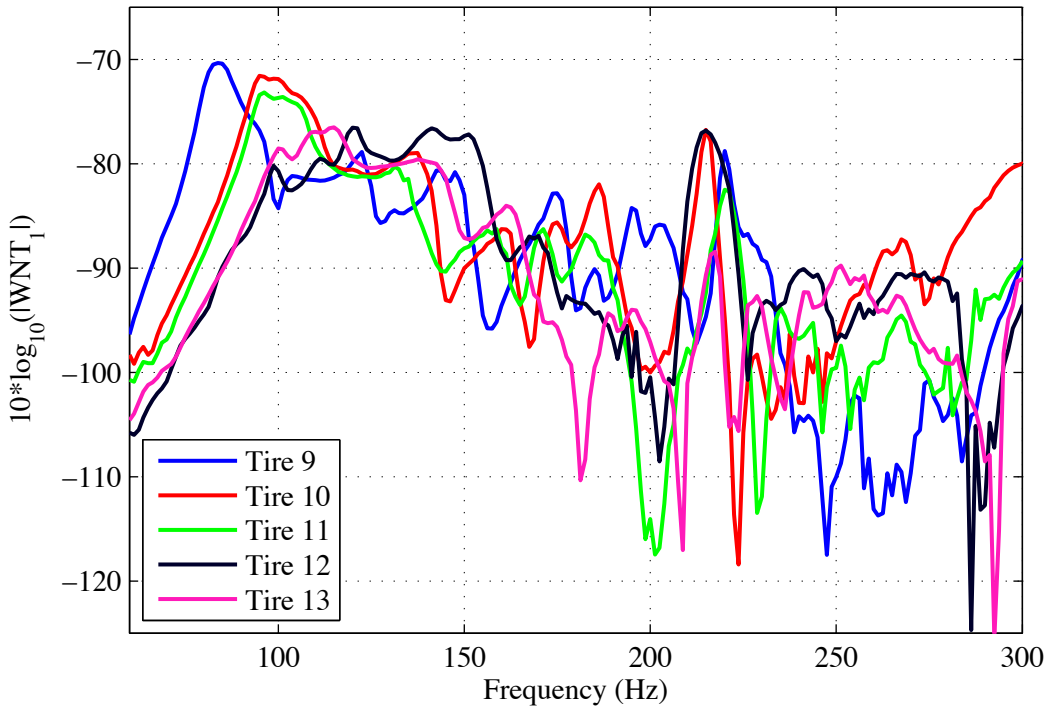

Figure 5.9. Structure-borne noise potential for five tires from patch excitation.

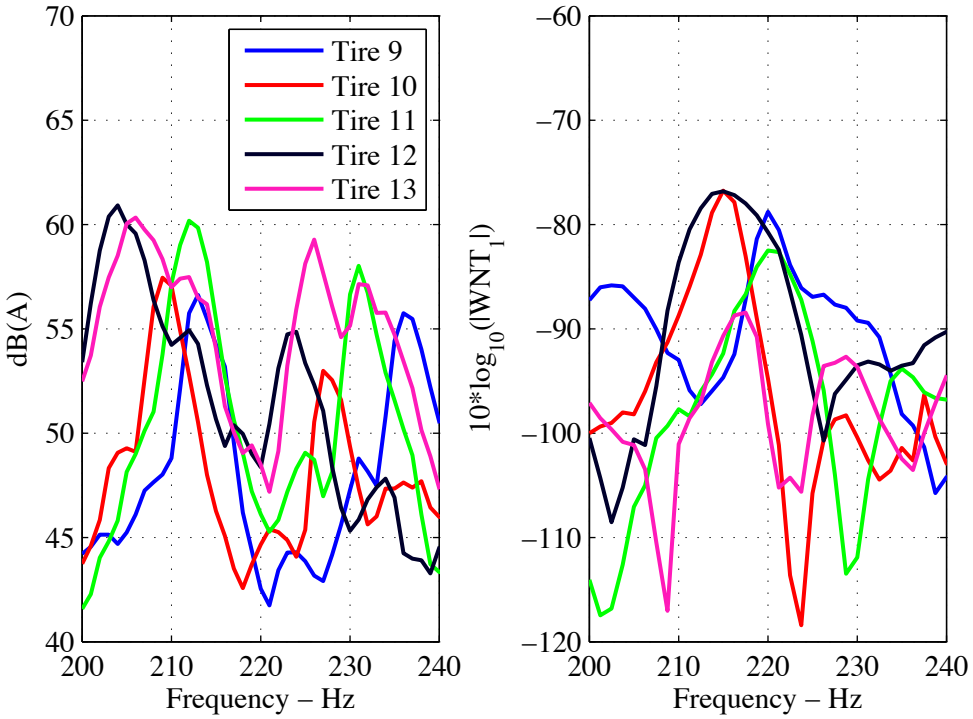

Figure 5.10. Acoustic mode analysis from the structure-borne noise results from the automobile OEM (left) and structure-borne noise potential for five tires from patch excitation (right).

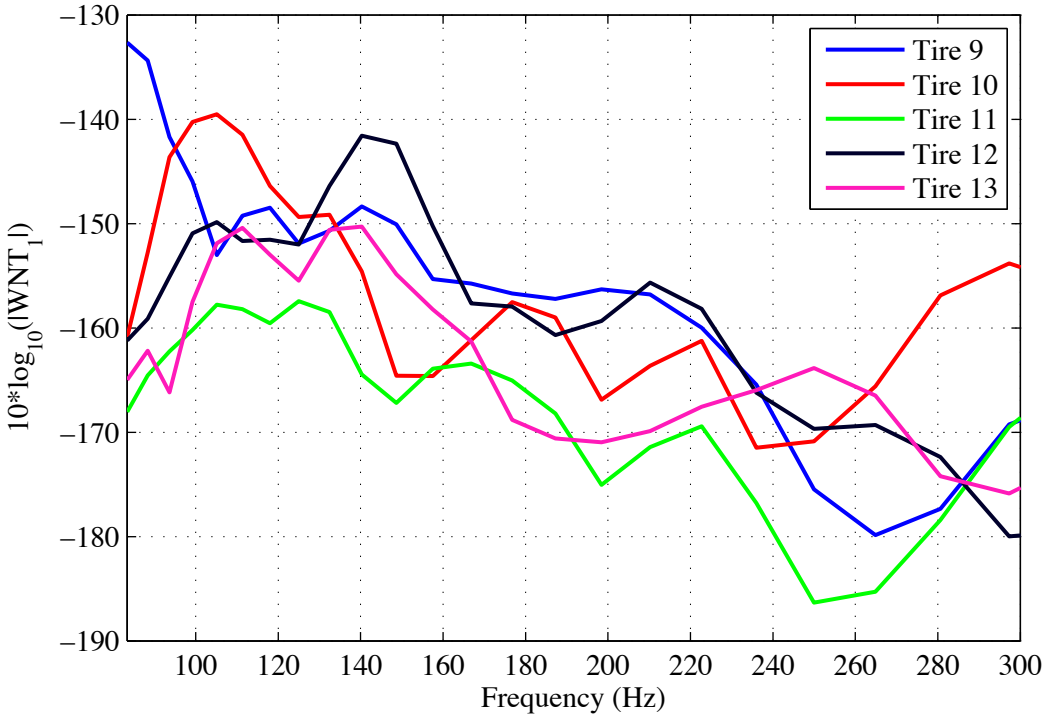

Figure 5.11. Structure-borne noise potential for five tires from patch excitation modified by the moving input function at 80 kph.

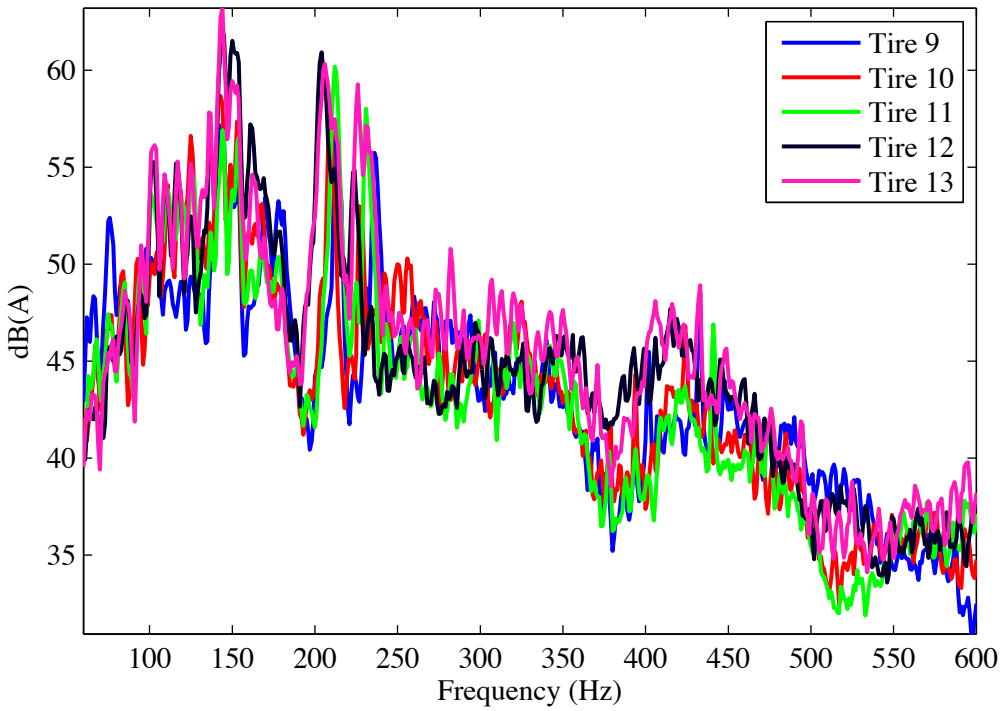

Figure 5.12. Structure-borne narrow band noise measurements from the interior of a car of 5 tires.

level is quite poor with a $d_{error} = 2.76$. Figure 5.14 is the comparison of the speed modified structure-borne noise prediction and automobile OEM experimental ranks. The d_{error} of the combined methods is 2.61. The error for both seems largely related to the influence of the first flexural mode's cut-on frequency around 100 Hz. Since the TPTA measurements did not show a relationship between this feature and normal acceleration, the low frequency limit may be raised to account for this.

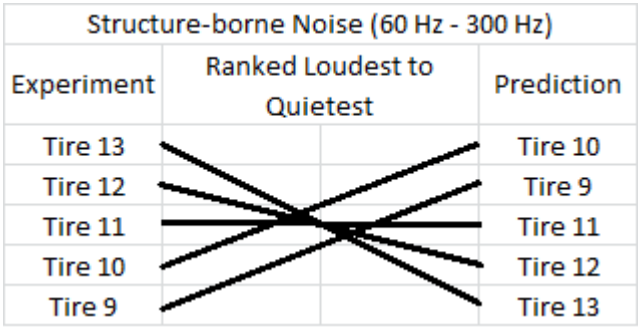

Figure 5.13. Overall structure-borne noise level comparison between experimental data and prediction without moving input method.

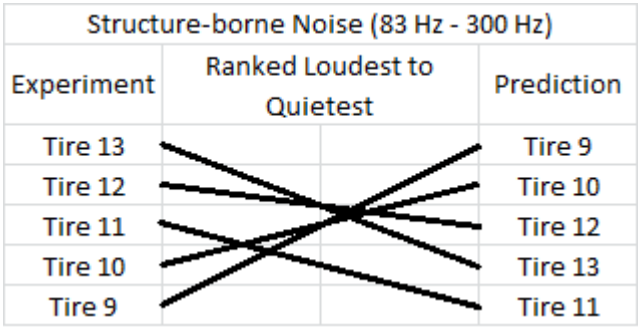

Figure 5.14. Overall structure-borne noise level comparison between experimental data and prediction with moving input method.

5.5 TPTA Experimental Results

Before drawing conclusions about the validity of the relative tire noise model, follow-up TPTA testing was conducted with the five new tires. The purpose was to

identify differences between automobile OEM results, TPTA results, and the relative tire noise model.

5.5.1 On-Board Sound Intensity Results and Analysis

The coherence of the five tires, shown in Figure 5.15, appeared similar to the results for the initial eight tires. The peak at 800 Hz for the pavement-averaged On-Board Sound Intensity (OBSI), shown in Figure 5.16 is again a common spectral feature. The OBSI levels per pavement are plotted in Appendix C, Figure C.11. Since the levels at the 630 Hz band were significantly lower than the remaining spectra, the suggestion that the majority of airborne noise contribution from tires occurs at and above the 800 Hz third-octave band is considerably strengthened. By comparing the ranking of the automobile OEM airborne noise results and the TPTA OBSI measurements over the 800 Hz - 1250 Hz range in Figure 5.17, the noise variation from vehicle velocity also seems to be confirmed since no change in ranking is expected if changing speed has no effect on spectral content and overall levels.

Using the relative tire noise model with a 30 mph speed to match the TPTA experiment, the spectral content does change compared to the model at 80 kph. Figure 5.18 shows airborne noise potential for the tires at a speed of 30 mph has much less energy in the 800 Hz and 1000 Hz third-octave bands. This suggests that the moving input function does not contribute as much to the airborne noise potential at lower speeds. The increase seen in the 80 kph prediction appears to have shifted to lower frequencies and may affect the structure-borne noise potential. An overall level comparison between the TPTA and relative tire noise model is shown in Figure 5.19 and has a $d_{error} = 1.10$.

5.5.2 Accelerometer Results and Analysis

The acceleration in the tire's direction of travel, plotted in Figure 5.20, has a peak in spectral content around 160 Hz. The magnitude in the remaining frequency range

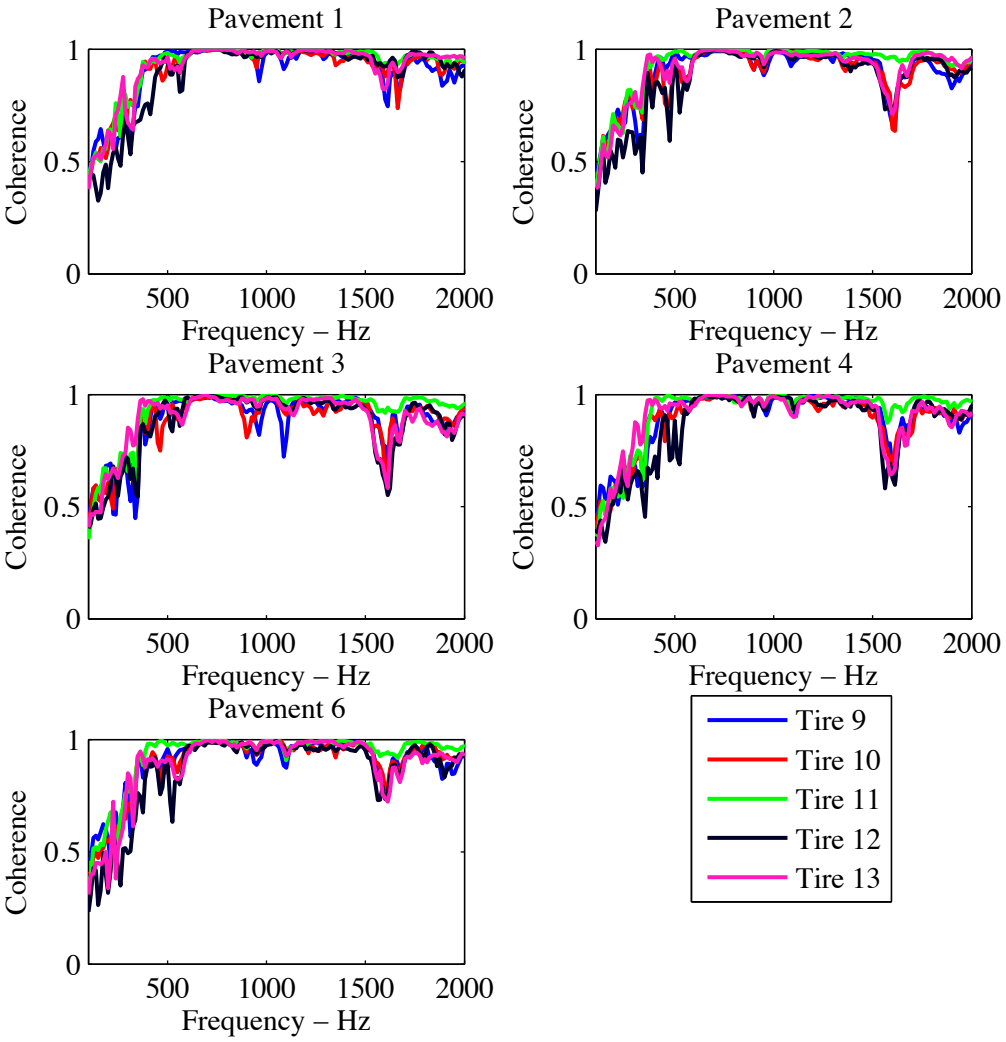

Figure 5.15. The coherence per pavement for the five tires tested.

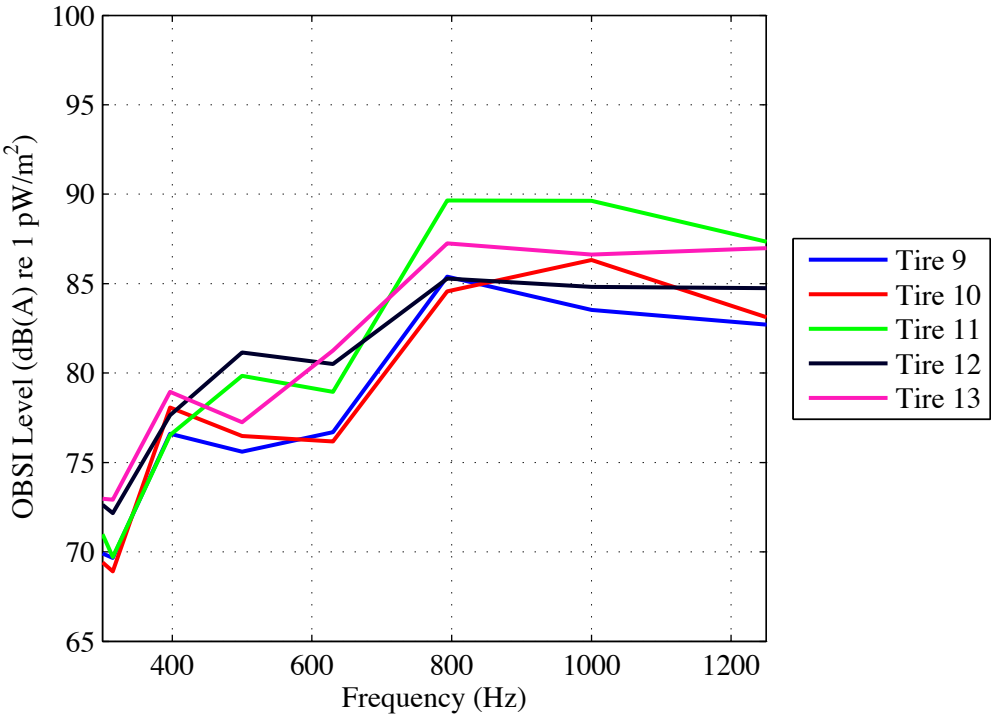

Figure 5.16. Averaged sound intensity level for the five tires.

Airborne Noise (800 Hz - 1250 Hz)		
Experiment	Ranked Loudest to Quietest	TPTA
Tire 13		Tire 11
Tire 11		Tire 13
Tire 9		Tire 12
Tire 12		Tire 10
Tire 10		Tire 9

Figure 5.17. Overall airborne noise level comparison between automobile OEM experimental data and TPTA results.

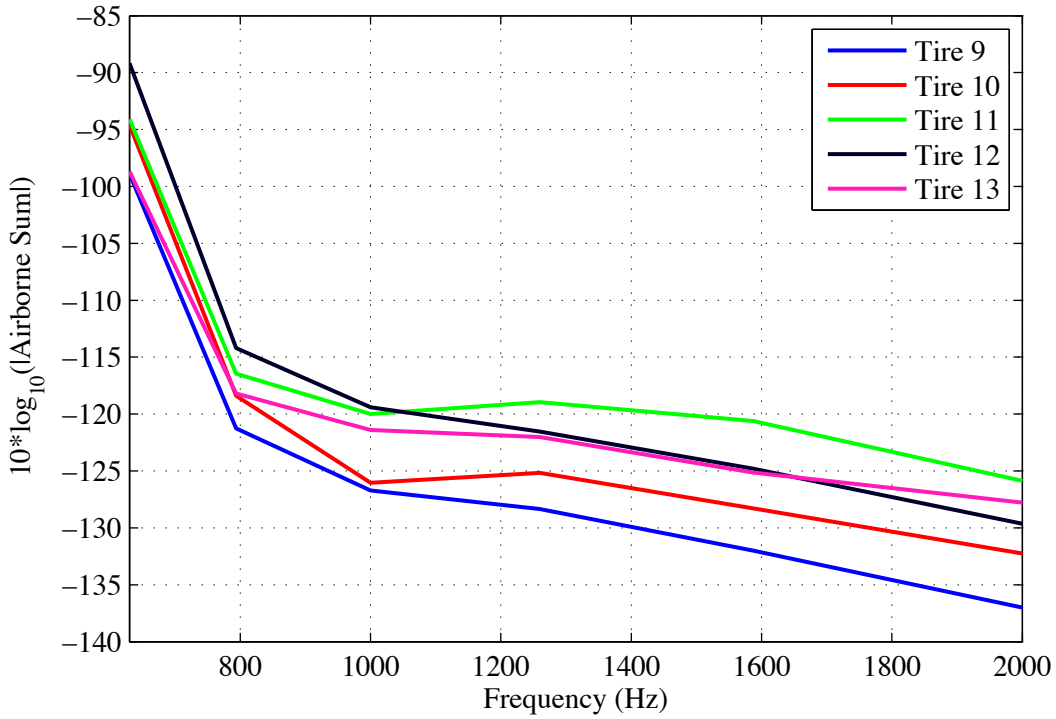

Figure 5.18. Airborne noise potential for five tires from patch excitation modified by the moving input function at 30 mph.

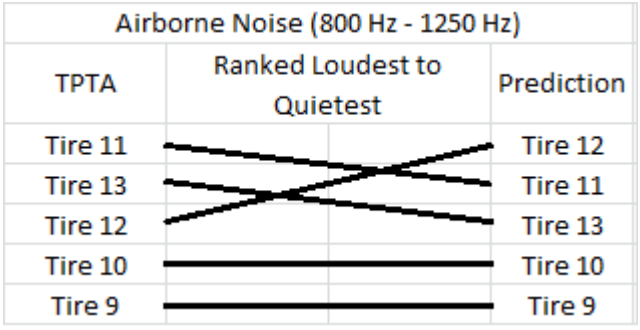

Figure 5.19. Overall airborne noise level comparison between TPTA results and prediction with the moving input method.

of interest was much lower. The original eight tires had similar results. A comparison of the spectrum with the automobile OEM's data shows almost completely incorrect ranking around the 160 Hz peak. This suggests that the noise is somehow related to the TPTA itself.

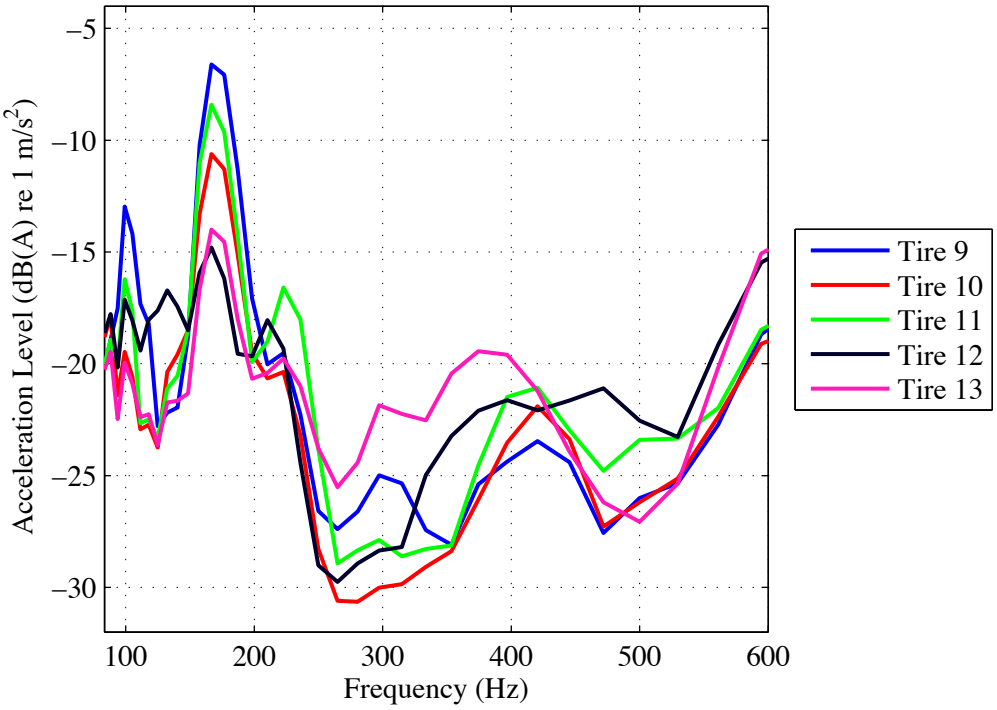

Figure 5.20. Acceleration in the tire's direction of travel (X-axis) for the five tires.

Figure 5.21 shows the measured out-of-plane acceleration. As with the X-axis acceleration, the spectral content has multiple similarities. However, the peak around 200 Hz - 300 Hz is not the same for all the tires. The original set of eight tires were all tested with the same rim model. The second set of five tires had several different rims. It would appear that the out-of-plane acceleration levels have spectral contributions resulting from the tire-rim relationship.

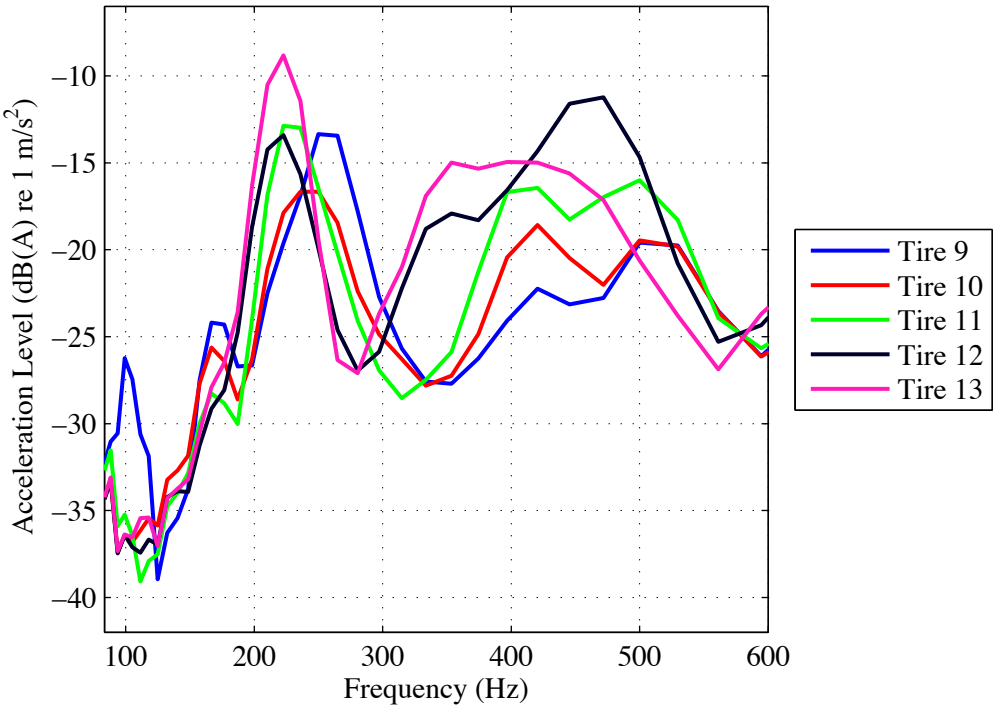

Figure 5.21. Out-of-plane acceleration (Y-axis) for the five tires.

As expected, the normal acceleration, shown in Figure 5.22, also has features similar to the original eight tires. The peak around 160 Hz that was assumed to be related to noise has a larger range in magnitude than the previous test results. It can be assumed that this difference is related to a rim-tire interaction that is the source of the noise or excites a TPTA related noise source. The acoustic mode appears quite clearly around 210 Hz - 220 Hz, and the ring frequency shifts in both level and range for each tire.

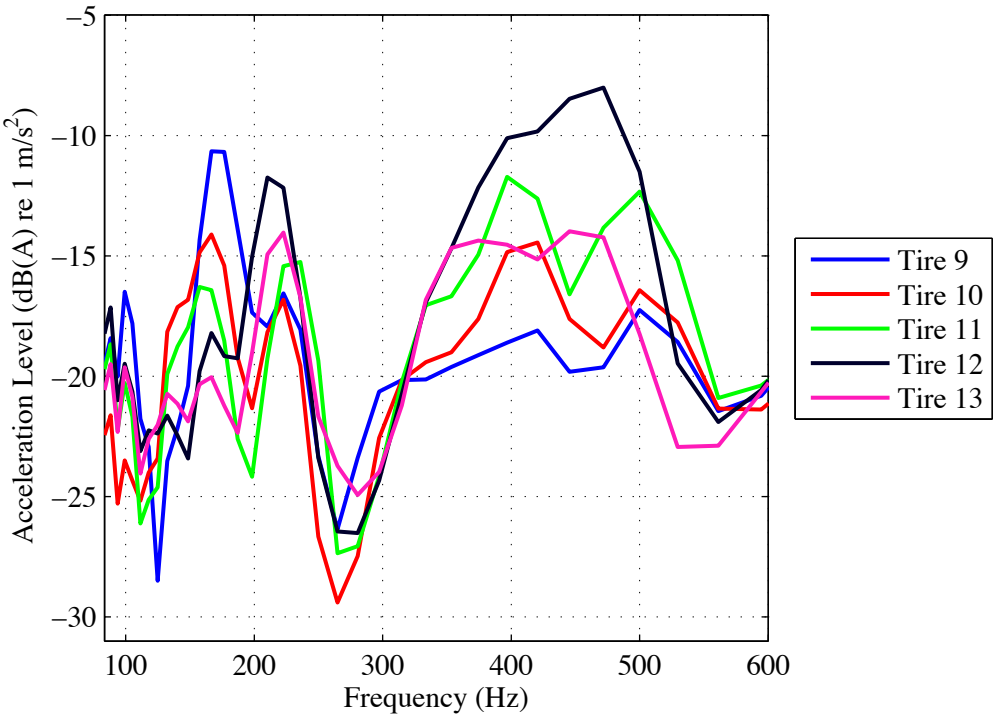

Figure 5.22. Normal acceleration (Z-axis) for the five tires.

Figure 5.23 shows that the overall level comparison for the frequency range of 60 Hz - 300 Hz has poor correlation between the interior cabin noise levels and TPTA results. However, this is including the unidentified noise source around 160 Hz that shows no similarities to the spectral content from the automobile OEM's test. By calculating an overall level from the acoustic mode frequency range to 300 Hz, the

d_{error} decreases from 2.61 to 0.63. Since the acoustic mode is the main contributor to the structure-borne noise level in the interior cabin, it can be assumed that this is a feature that should be focused on for predicting tire related noise, especially given the speed independence of the acoustic mode.

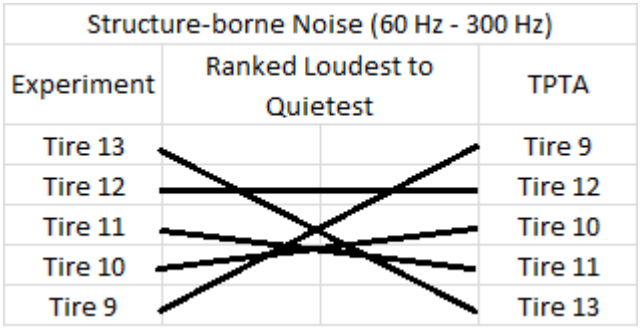

Figure 5.23. Overall airborne noise level comparison between automobile OEM experimental data and TPTA results.

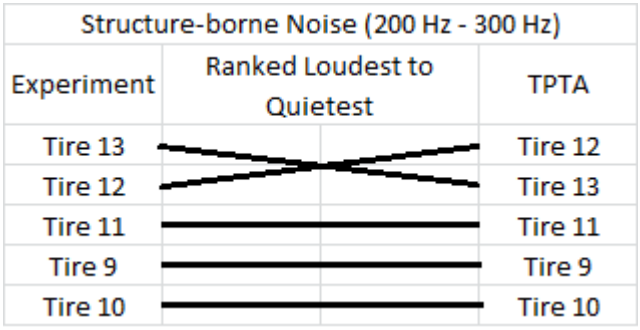

Figure 5.24. Overall airborne noise level comparison between automobile OEM experimental data and TPTA results.

By changing the speed of the moving input function, the vibration potential of each tire varies from the higher speed model. Figure 5.25 shows the prediction up to 600 Hz since this is where the pattern noise showed significance when compared with the TPTA results from the initial set of tires. While the vibration potential spectrum shows strong similarities to the TPTA spectrum, the levels of the content vary significantly as evidenced by the overall level comparison in Figure 5.26. Tire

12 is ranked completely incorrectly and the $d_{error} = 2.10$. By examining the 200 Hz - 300 Hz range as done previously, the acoustic mode rankings appear to be incorrect as well. Since speed was found to not affect this frequency range significantly, the vibration potential without the moving input, Figure 5.10, was re-examined. The acoustic mode ranking was found to be different from both the automobile OEM test results and the TPTA data. Further analysis found that the acoustic mode ranks appeared to be based on tire width unlike the other tests. Because the same beam was used for patch excitation, it is suggested that the forcing method did not efficiently excite the acoustic mode on the wider tires as it did with the narrower ones.

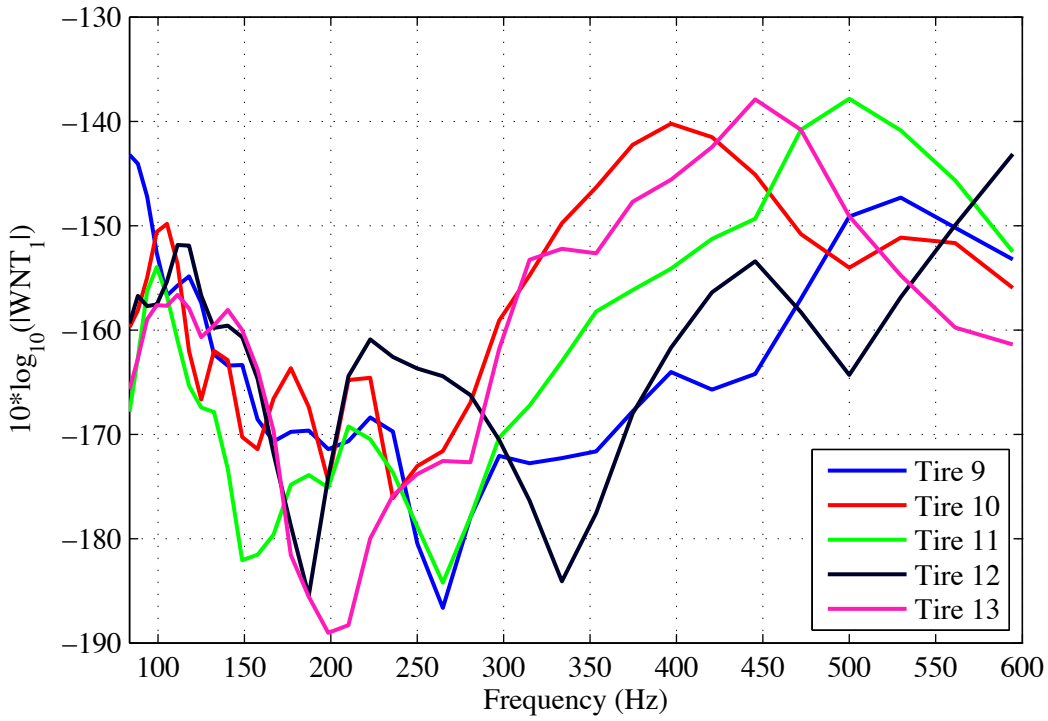

Figure 5.25. Structure-borne noise potential for five tires from patch excitation modified by the moving input function at 30 mph.

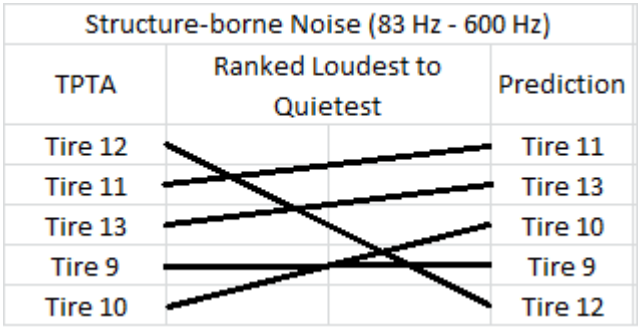

Figure 5.26. Overall airborne noise level comparison between TPTA results and prediction with the moving input method.

5.5.3 Acoustic Mode Noise Reduction

Mohamed and Wang recently found that the strength of the acoustic mode could be reduced by installing sound absorbing material within the tire cavity [17]. The experiment was performed using a traditional tap test where the tire is unloaded and stationary. Since the acoustic mode has been identified as a major source of structure-borne noise, a verification of this reduction in noise level was examined using the TPTA. Glass fiber was glued to the interior of Tire 5, shown in Figure 5.27. The tire was remounted to the rim and tested on the TPTA.

Figure 5.27. Tire 5 with glass fiber chemically attached to the inside diameter of the carcass.

The OBSI results, plotted in Figure 5.28 , showed little change. The X-axis and Y-axis acceleration measurements had slight decreases in level around the acoustic mode frequency, but the magnitude of normal acceleration significantly dropped. Figure 5.29 shows the effect the glass fiber material has on the acoustic mode. This

suggests that the acoustic mode can be effectively damped to reduce the structure-borne noise experience in the vehicle's cabin.

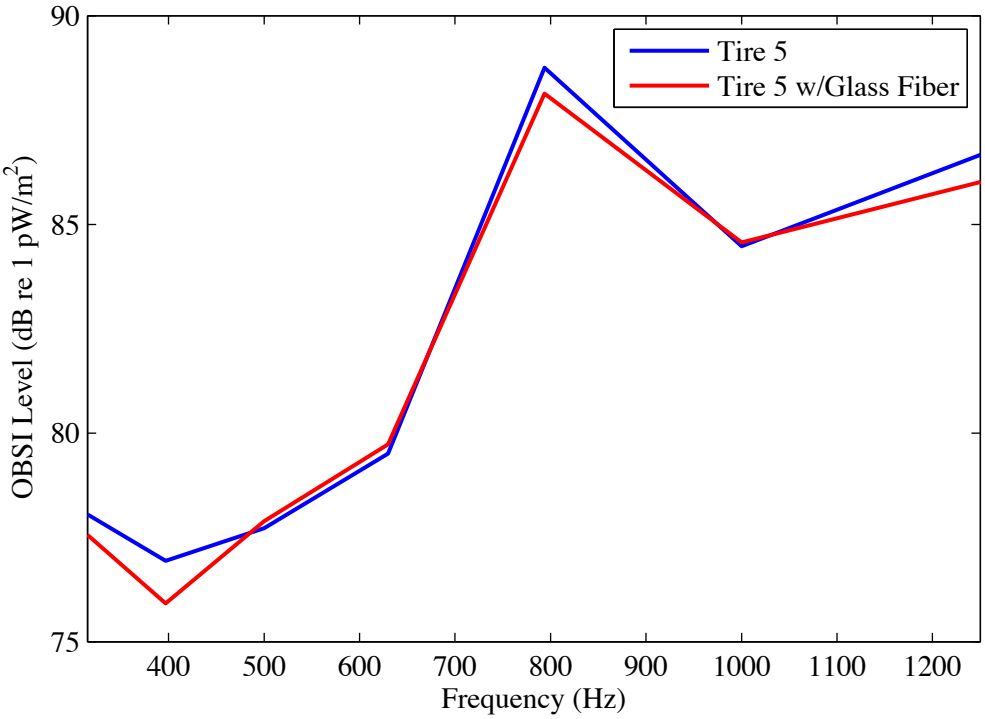

Figure 5.28. Averaged sound intensity level for tire 5 with and without the glass fiber.

5.6 Summary of Relative Tire Noise Potential Model

The prediction model and two experimental results had similarities and differences between them. The airborne potential from the model ranked the tires relative to each other with a small amount of error when compared against the automobile OEM data. By identifying that the major source of airborne noise occurs above 800 Hz, the efficiency filter was not required since the moving input adjusted the spectrum accordingly. This would suggest that the noise effect of the tread pattern moves

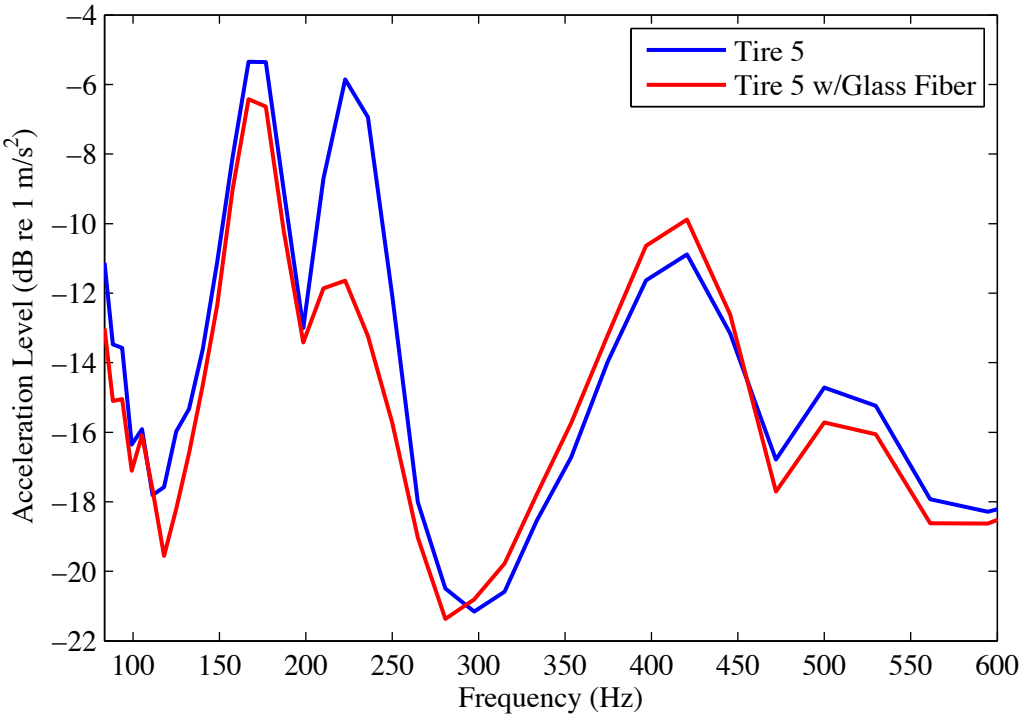

Figure 5.29. Normal acceleration (Z-axis) for tire 5 with and without the glass fiber.

through frequency with speed and has a greater impact on the airborne noise at higher speeds, such as the 80 km/h at which the automobile OEM conducted tests. The structure-borne noise potential comparison of the model and OEM data had poor correlation and the frequency range of interest appears to be below the effect of the moving input function.

By comparing the TPTA results with the automobile OEM data, an analysis of the effects of speed on a tire's airborne and structure-borne noise could be reviewed. The rankings for airborne noise showed that speed does have an effect on level when comparing tires. For the structure-borne noise, an extremely accurate ranking was found when examining the acoustic mode frequency range, which appeared to be a major contributor in both tests. This would suggest that structure-borne noise in the lower frequency ranges is independent of speed.

The TPTA data comparison with the relative tire noise potential model had some success again with the airborne noise potential. Even though a majority of the pattern noise appeared to shift to lower frequencies, the model still predicted the rankings well. Concerning structure-borne noise, the ineffective prediction led to the conclusion that the patch excitation forcing method needs to be refined in order to collect a tire's dynamic response more similar to what it experiences on a road surface.

6. CONCLUSIONS AND RECOMMENDATIONS FOR FUTURE WORK

6.1 Conclusions

The goal of this research was to determine if an off-vehicle stationary tire test could rank tires relative to each other in terms of airborne and structure-borne noise. This would allow further experiments to be run selectively with a subset of the numerous tires in existence. Creating this subset would decrease the cost associated with traditional tire noise measurements and allow automobile OEM's to select and recommend tires to increase passenger comfort and decrease noise pollution in driving environments.

The beginning of this research focused on identifying differences in airborne and structure-borne noise between a sample set of tires. This analysis was carried out by conducting a experiment with the Tire Pavement Test Apparatus (TPTA) in Herrick Laboratories at Purdue University. On-Board Sound Intensity (OBSI) and tri-axial acceleration measurements were taken and processed for comparison. Features, such as the 800 Hz peak unrelated to speed, for the sound intensity calculation were verified and expected vibrational characteristics, for example, the first acoustic mode around 200 Hz and the ring frequency around 400 Hz, were shown in the results.

In Chapter 3, the focus was on the stationary tire test. Two excitation methods were used to compare the dynamic characteristics in the presence of different forces. The wavenumber decomposition of the circumferential point mobilities revealed the differences in waveguide behavior for each tire. The airborne noise potential of a tire was assumed to be related to features with phase speeds above the speed of sound. These supersonic components were summed across the wavenumber domain and did not appear to have much correlation below 800 Hz for the point excitation. The patch excitation reduced the presence of higher order transverse modes, but did not

adequately reduce the airborne noise prediction levels in the required range. This disagreement in the data was assumed to be due to a radiation efficiency and is addressed later. The cut-on frequencies for flexural waves were located at the first circumferential mode, which applies a net force to the hub. The spectral content of the mode showed some similarities to the normal acceleration from the TPTA measurements, especially with the patch excitation method.

The moving input function was developed in Chapter 4 as a result of the variance in noise related to speed found with TPTA measurements. The use of the tread pattern as an excitation in combination with the vehicle velocity was assumed to be beneficial in modifying the stationary tire test data to more accurately predict tire noise. Experimental results with a tire showed some spectral similarities relating to peak location and change with speed. The airborne components had a linear level vs. logarithmic speed relationship found with all tires. The structure-borne noise contained spectral shapes very close to the data from the TPTA experiment. Theoretical tread patterns were developed and proved that some merit exists with the method as far as speed related excitation.

The focus of chapter 5 was the use of the relative tire noise potential model, a combination of the stationary tire test and moving input function. A functional test stand was manufactured and five tires were provided that had varying airborne and structure-borne levels according to tests by an automobile OEM. The relative tire noise potential model was able to rank the airborne noise for the five tire with almost no error. The structure-borne noise prediction was quite inaccurate, and testing using the TPTA was conducted to identify differences between the prediction model and experimental results. The results of all three helped conclude that speed and tread pattern have a strong effect on relatively ranking the airborne noise of tires. The structure-borne noise below 300 Hz appeared to be unaffected by speed between the two experiments and the ineffective ranking by the model suggests that the patch excitation method needs to be improved. The 300 Hz - 600 Hz range had strong correlation between the moving input spectrum and TPTA results since 30 mph places

tread pattern noise in this frequency range. However, incorrect magnitudes, which could also be related to the inefficient patch excitation, limited the verification of the model in this range. The acoustic mode was determined to be a major component of the structure-borne noise and an attempt to reduce its level was very successful.

6.2 Future Work

Concerning the stationary tire test, future research should focus on improving the patch excitation method. Multiple beams could be created based on tire widths to apply a similar force to any tire. Ideally, the tire would be put under a load to mimic supporting a vehicle and excited. This would create a measurement difficulty since a laser vibrometer would be unable to measure circumferentially, but this could be overcome using an accelerometer mounted between treads or inside the tire cavity.

The moving input function appears to offer an effective way of modifying the tire's dynamic characteristics to predict airborne noise potential based on speed. If a tire could be made with a completely periodic tread pattern, the theoretical analysis could be verified. The current method of obtaining the tread pattern is quite crude so analyzing an accurate tread pattern from a tire manufacturer might help in proving the validity of the method concerning production tires.

LIST OF REFERENCES

LIST OF REFERENCES

[1] David S. Michaud, Stephen E. Keith, and Dale McMurchy. Annoyance and disturbance of daily activities from road traffic noise in Canada. *Journal of the Acoustical Society of America*, 123:784–792, 2008.

[2] Ta-Yuan Chang, Chiu-Shong Liu, Bo-Ying Bao, Su-Fei Li, Tzu-I Chen, and Yen-Ju Lin. Characterization of road traffic noise exposure and prevalence of hypertension in central taiwan. *Science of The Total Environment*, 409(6):1053 – 1057, 2011.

[3] Ulf Sandberg and Jerzy Ejsmont. *Tyre/Road Noise Reference Book*. Informex, SE-59040 Kisa, Sweden, first edition, 2002.

[4] M. Heckl. Tyre noise generation. *Wear*, 113(1):157 – 170, 1986.

[5] W. Kropp. Structure-borne sound on a smooth tyre. *Applied Acoustics*, 26(3):181 – 192, 1989.

[6] R.J. Pinnington. A wave model of a circular tyre. part 1: belt modelling. *Journal of Sound and Vibration*, 290(12):101 – 132, 2006.

[7] R.J. Pinnington. A wave model of a circular tyre. part 2: side-wall and force transmission modelling. *Journal of Sound and Vibration*, 290(12):133 – 168, 2006.

[8] J. Stuart Bolton, Heuk Jin Song, Yoon Ki Kim, and Yeon June Kang. The wave number decomposition approach to the analysis of tire vibration. *INTER-NOISE and NOISE-CON Congress and Conference Proceedings*, 1998(1):97–102, 1998.

[9] Patrick Sabiniarz and Wolfgang Kropp. A waveguide finite element aided analysis of the wave field on a stationary tyre, not in contact with the ground. *Journal of Sound and Vibration*, 329(15):3041 – 3064, 2010.

[10] Tyler Dare. *Generation Mechanisms of Tire-Pavement Noise*. PhD thesis, Purdue University, August 2012.

[11] Measurement of Tire/Pavement Noise Using the On-Board Sound Intensity (OBSI) Method. Technical Report AASHTO TP 76-13, American Association of State Highway and Transportation Officials, 2013.

[12] Klaus Schaaf and Dirk Rooneberger. Noise radiation from rolling tires - sound amplification by the "horn-effect". *INTER-NOISE and NOISE-CON Congress and Conference Proceedings*, 1982(2):131–134, 1982.

[13] Wolfgang Kropp, François-Xavier Bécot, and Stéphane Barrelet. On the sound radiation from tyres. *Acta Acustica united with Acustica*, 86(5):769–779, 2000.

[14] R.A.G. Graf, C.-Y. Kuo, A.P. Dowling, and W.R. Graham. On the horn effect of a tyre/road interface, Part I: Experiment and computation. *Journal of Sound and Vibration*, 256(3):417 – 431, 2002.

[15] D. de Klerk and A. Ossipov. Operational transfer path analysis: Theory, guidelines and tire noise application. *Mechanical Systems and Signal Processing*, 24(7):1950 – 1962, 2010.

[16] Rui Cao and J. Stuart Bolton. Effect of rotation on the natural frequencies of coupled tire structural-acoustic modes. *INTER-NOISE and NOISE-CON Congress and Conference Proceedings*, 246(1):1109–1117, 2013.

[17] Zamri Mohamed and Xu Wang. A study of tyre cavity resonance and noise reduction using inner trim. *Mechanical Systems and Signal Processing*, 2014.

APPENDICES

A. ADDITIONAL PLOTS: NOISE RADIATION AND VIBRATION OF A RADIAL TIRE

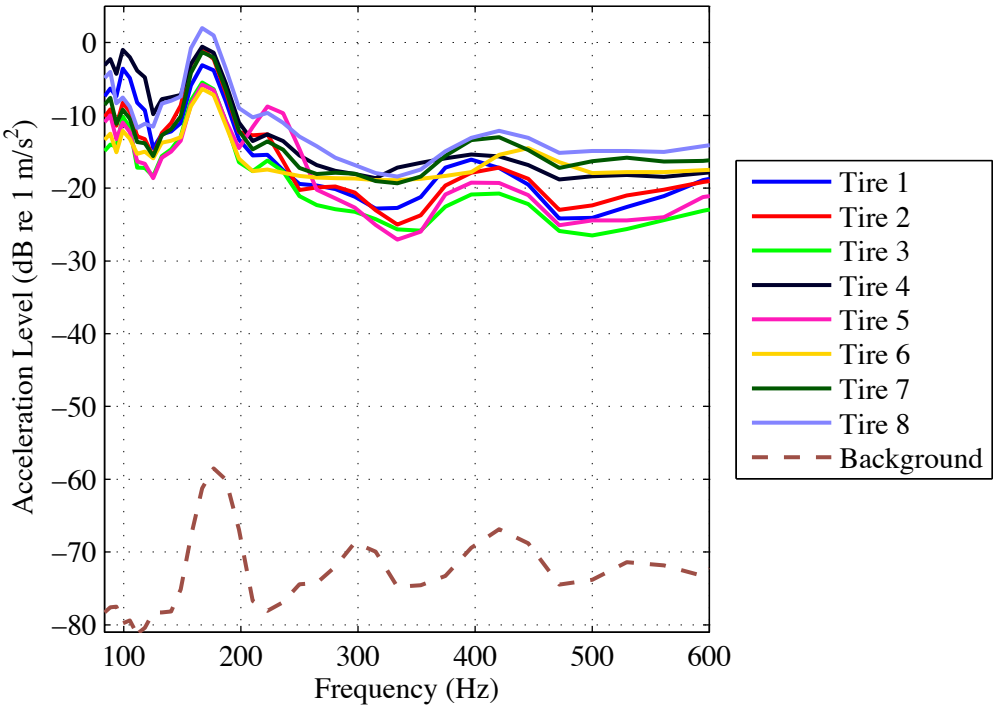

Figure A.1. Acceleration in the tire's direction of travel (X-axis) averaged over the 5 pavements for each tire compared with an unloaded tire's measurements.

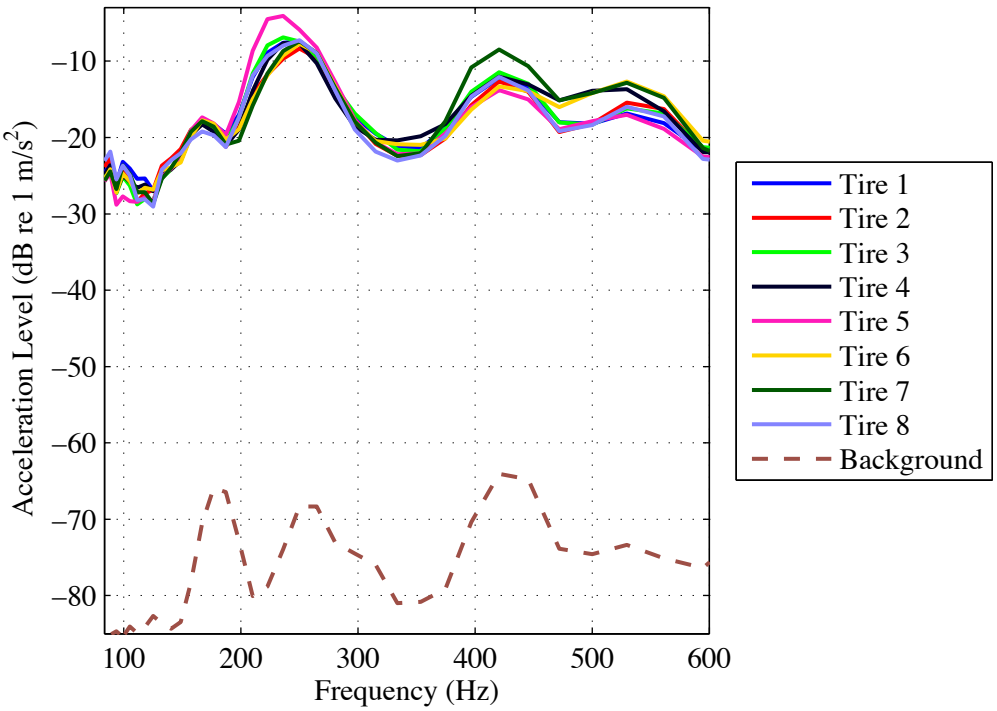

Figure A.2. Out-of-plane acceleration (Y-axis) averaged over the 5 pavements for each tire compared with an unloaded tire's measurements.

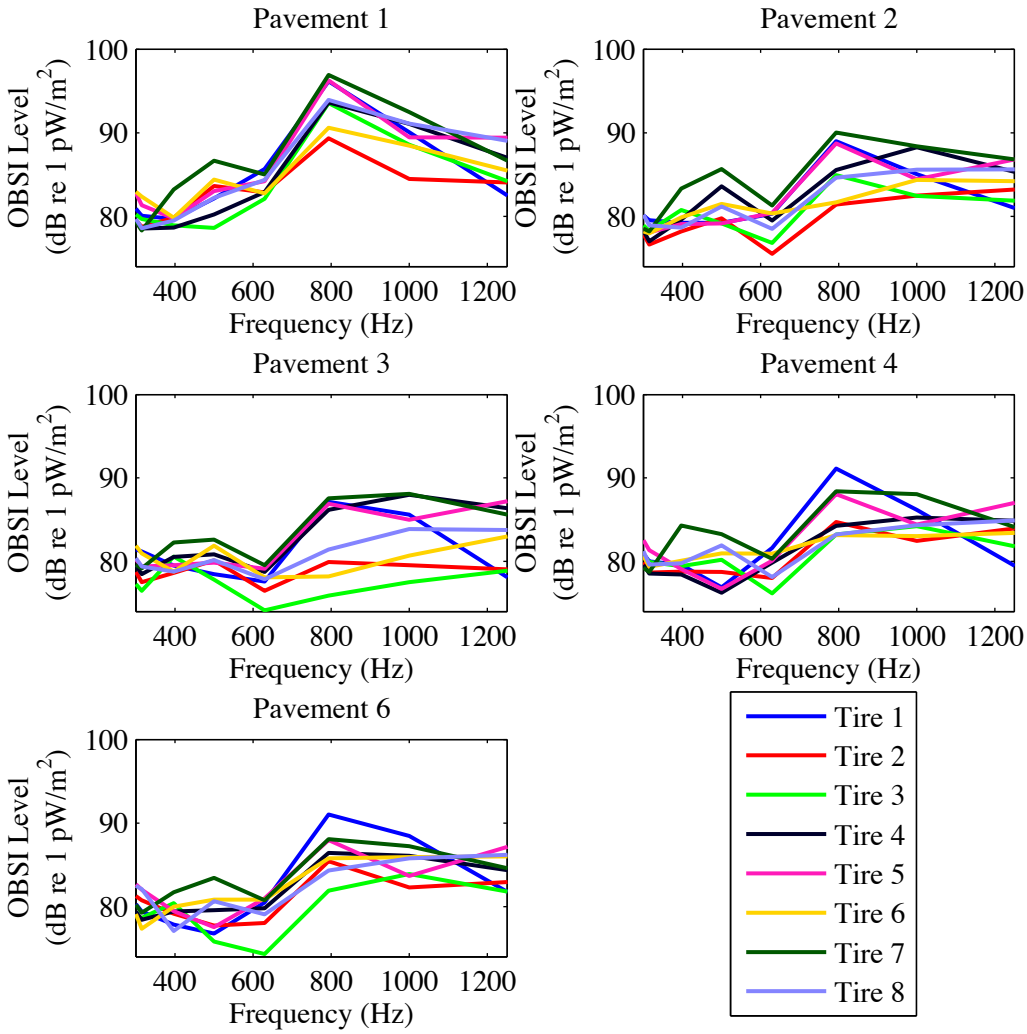

Figure A.3. Sound intensity level for each tire per pavement sample.

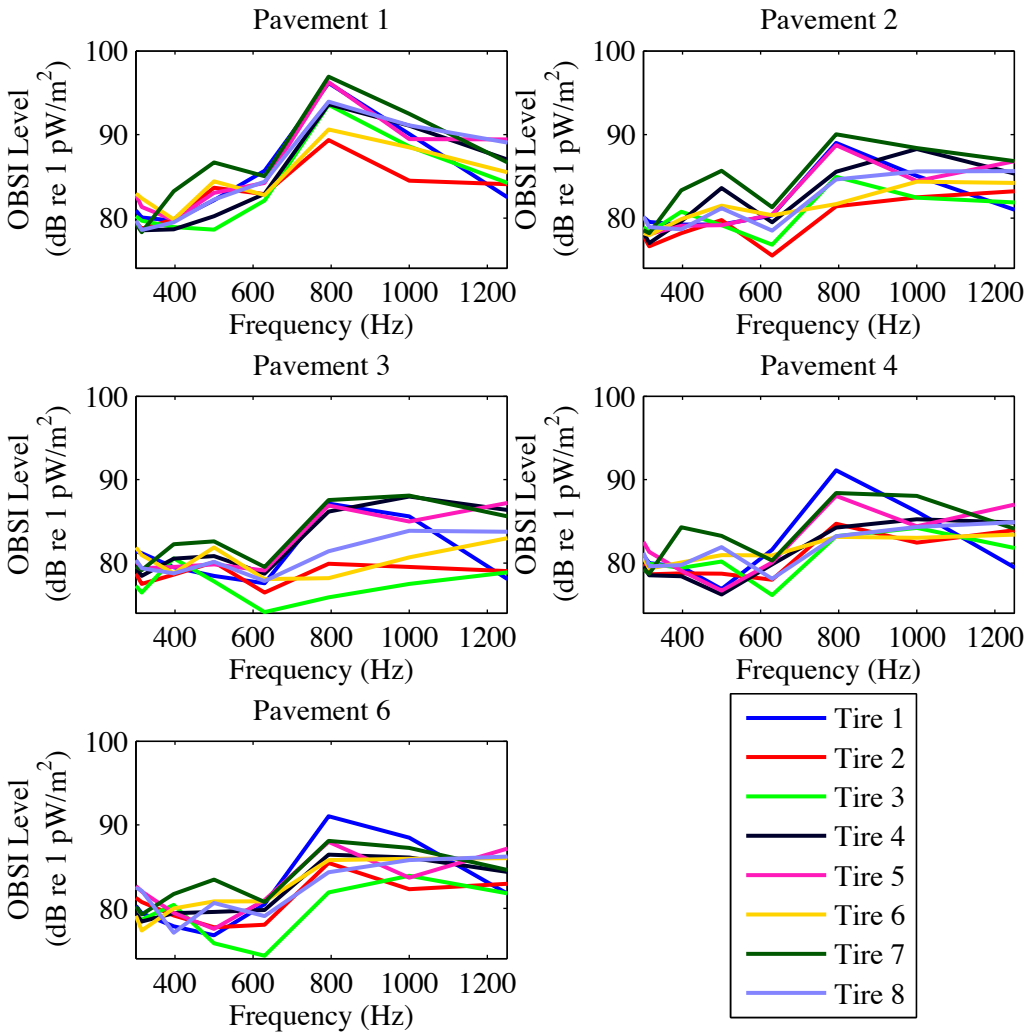

Figure A.4. Sound intensity level for Tire 7 per pavement sample for a range of speeds.

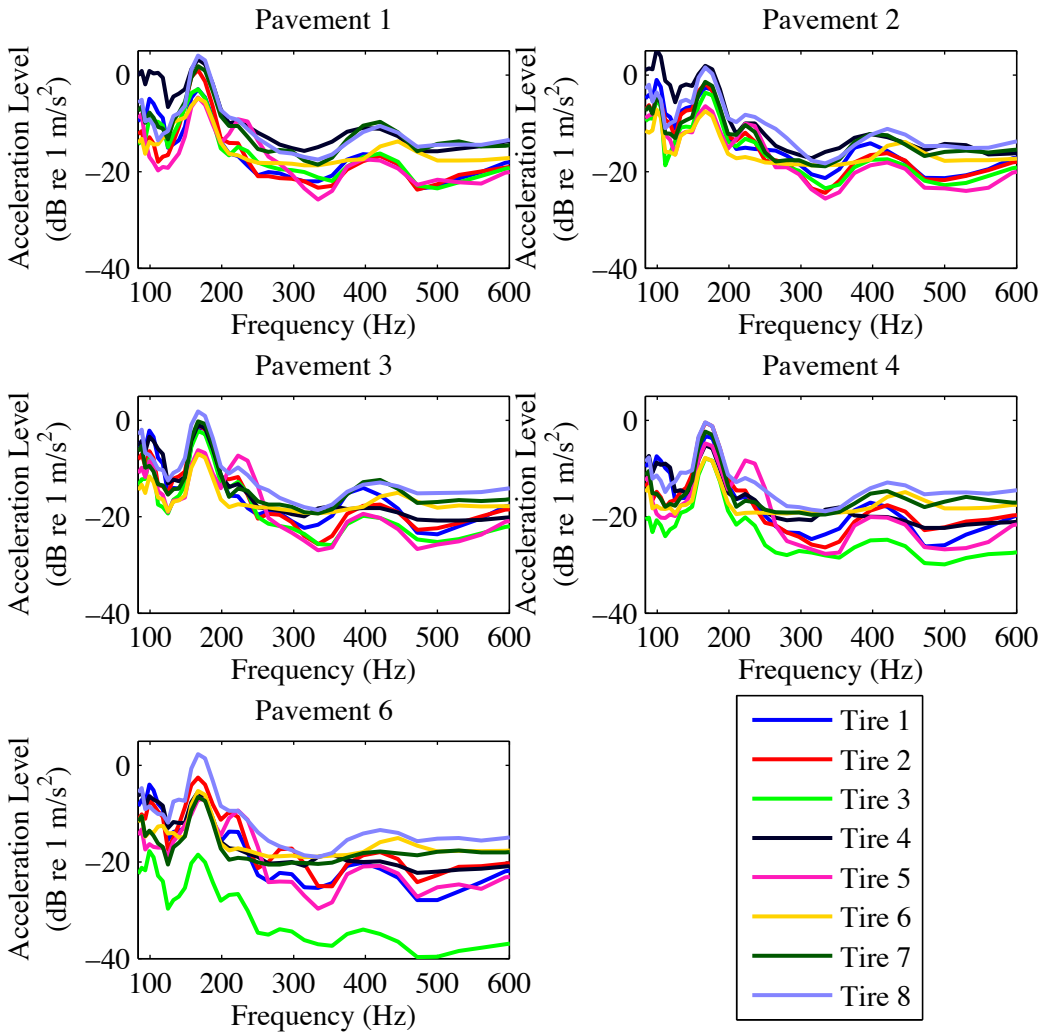

Figure A.5. Acceleration in the tire's direction of travel (X-axis) recorded for each tire per pavement.

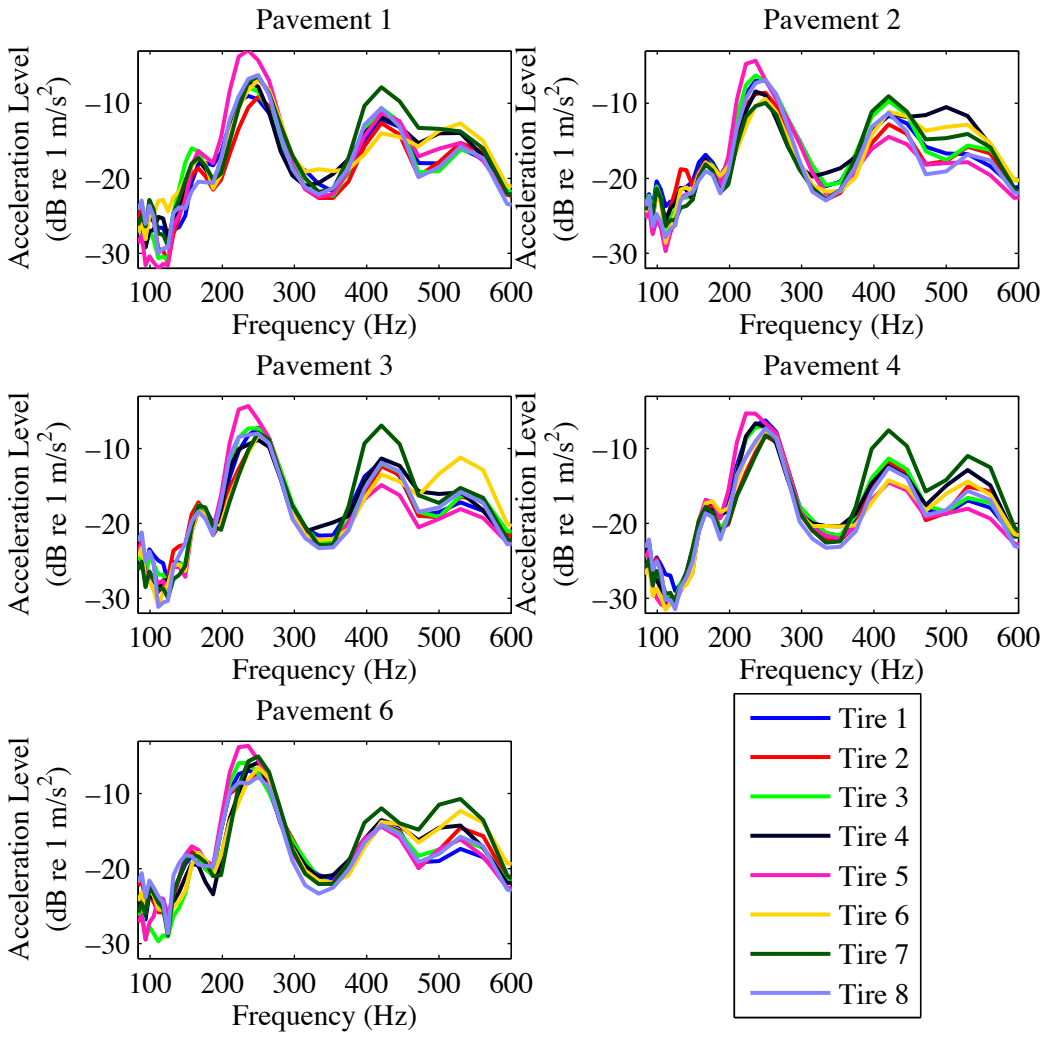

Figure A.6. Out-of-plane acceleration (Y-axis) recorded for each tire per pavement.

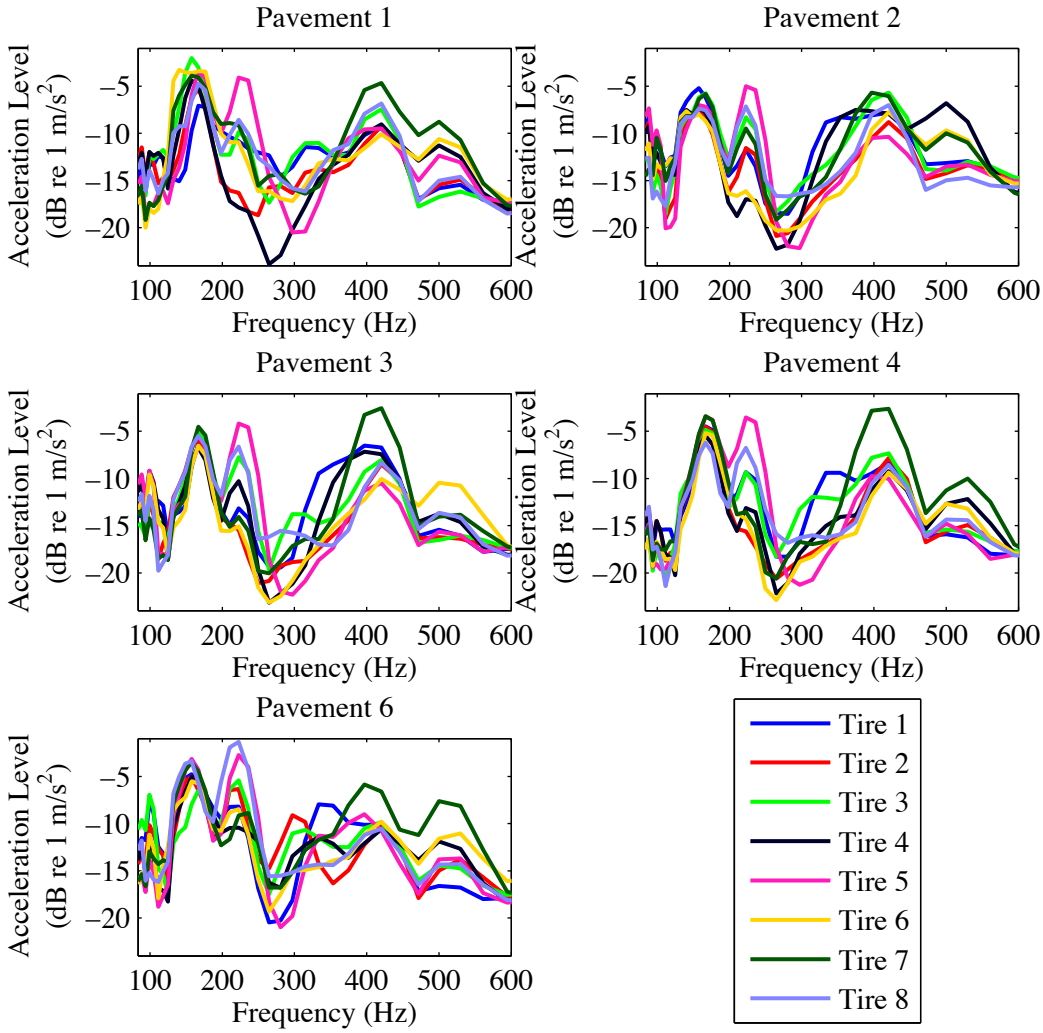

Figure A.7. Normal acceleration (Z-axis) recorded for each tire per pavement.

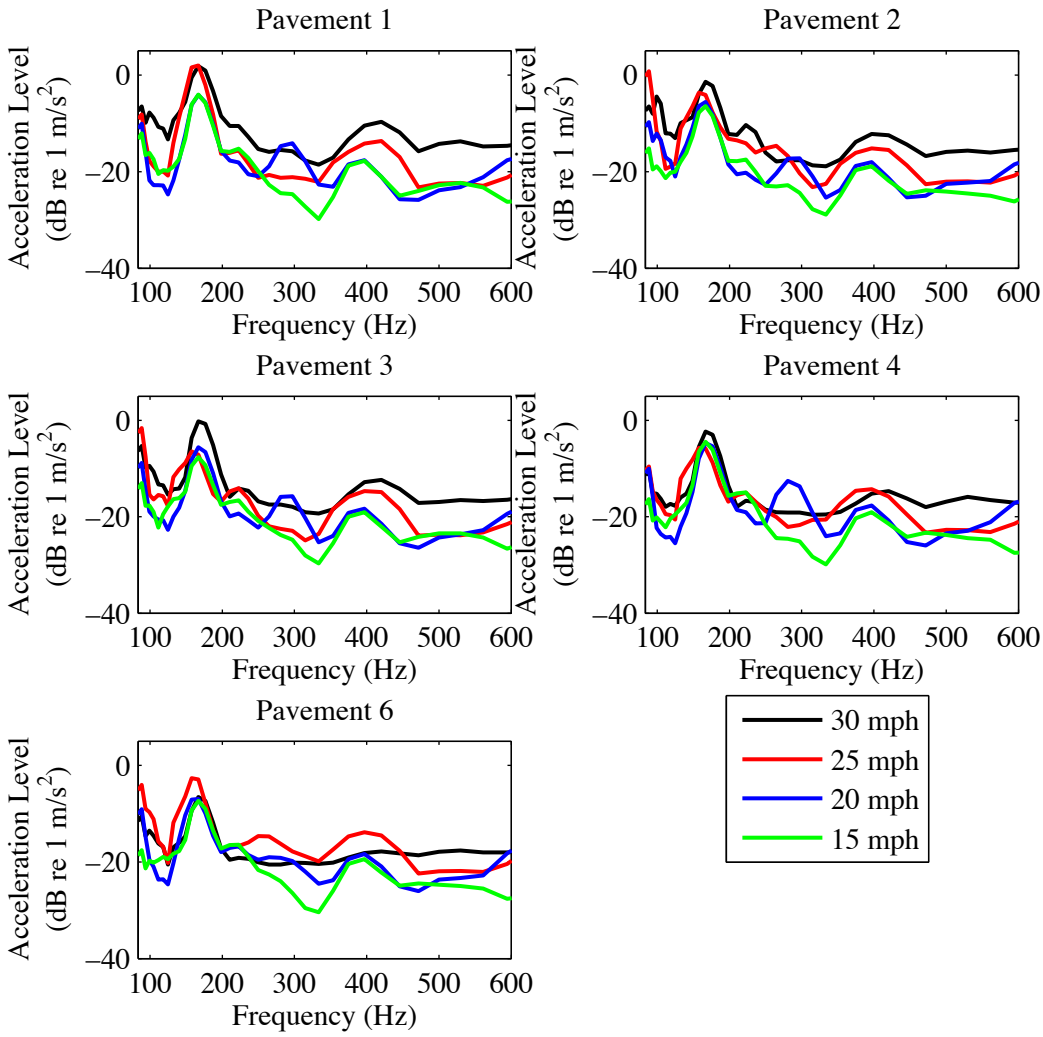

Figure A.8. Acceleration in the tire's direction of travel (X-axis) for Tire 7 per pavement sample for a range of speeds.

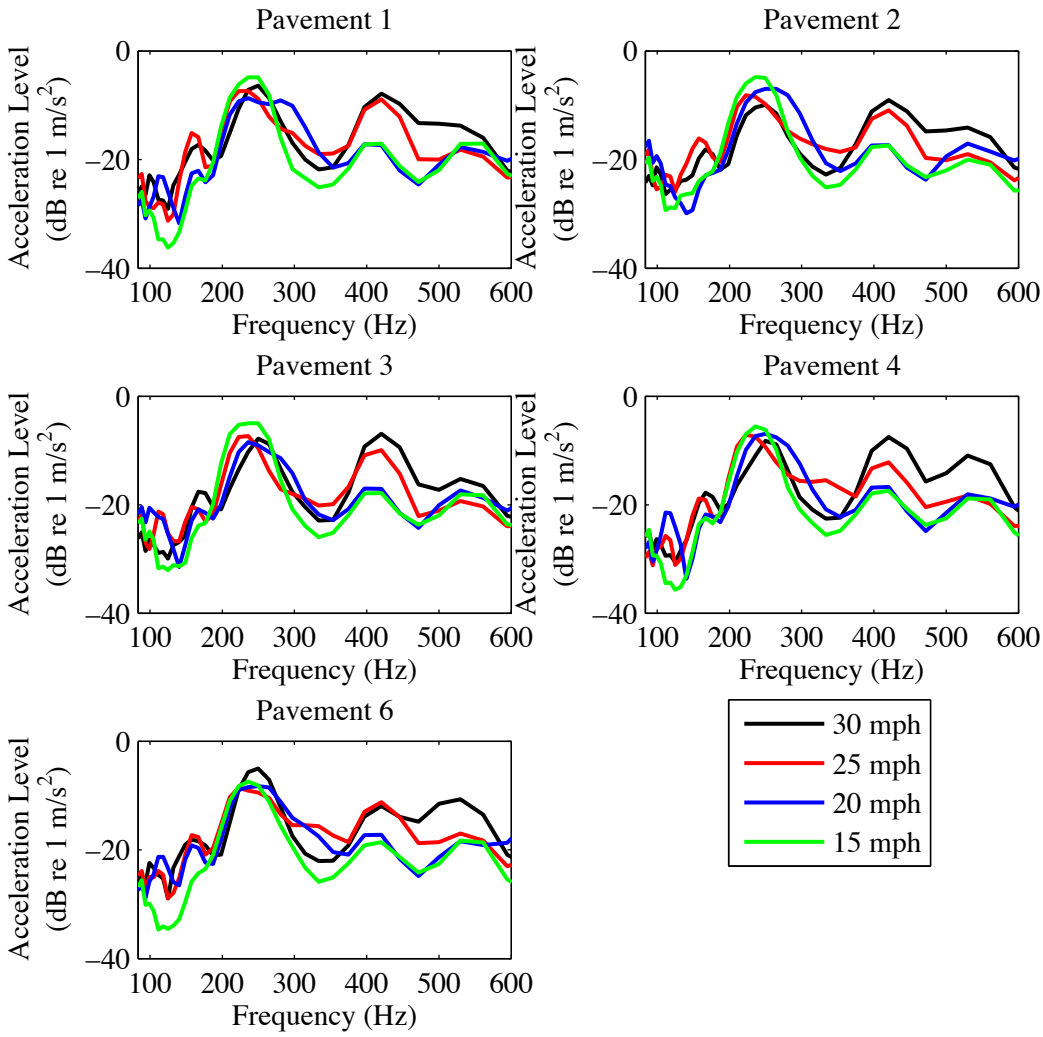

Figure A.9. Out of plane acceleration (Y-axis) for Tire 7 per pavement sample for a range of speeds.

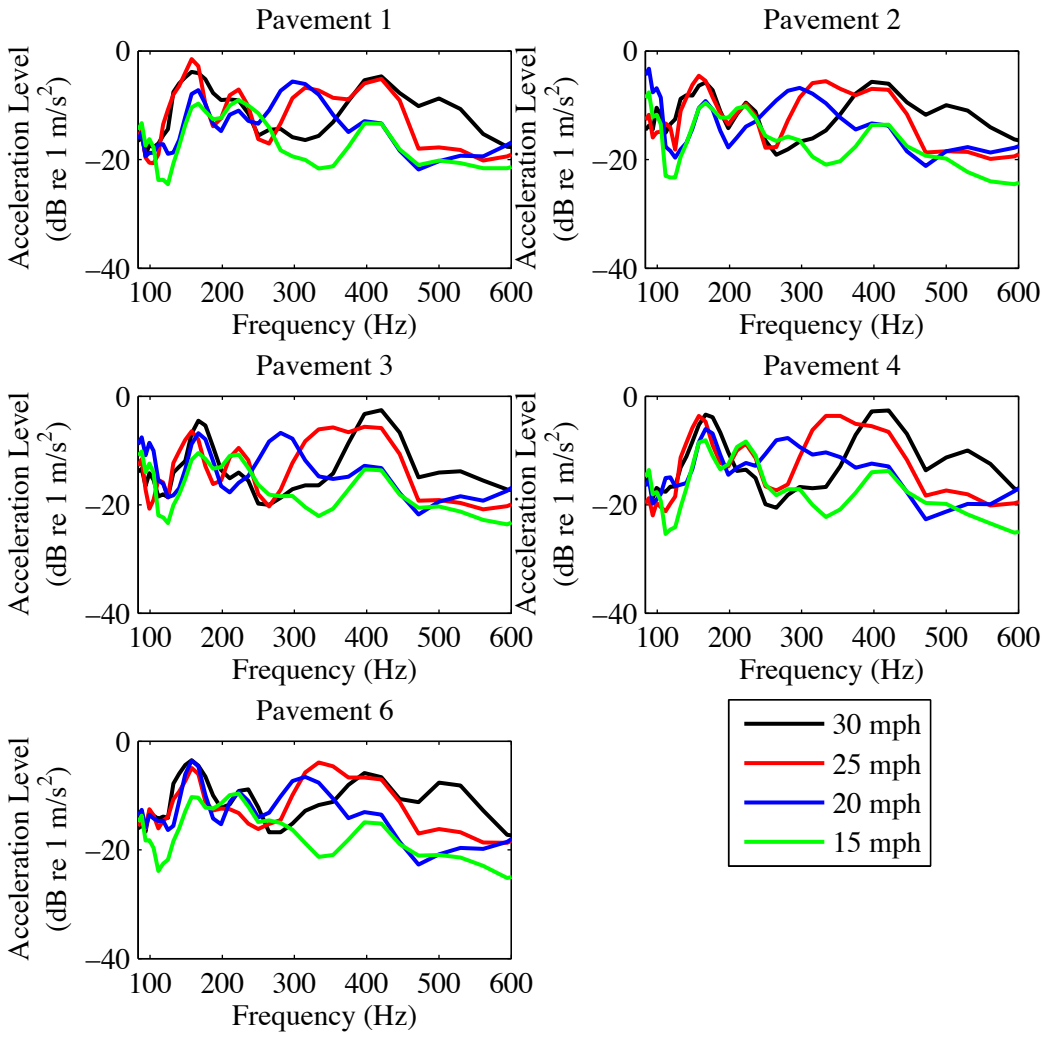

Figure A.10. Normal acceleration (Z-axis) for Tire 7 per pavement sample for a range of speeds.

B. ADDITIONAL PLOTS: STRUCTURAL WAVE PROPAGATION ON A RADIAL TIRE

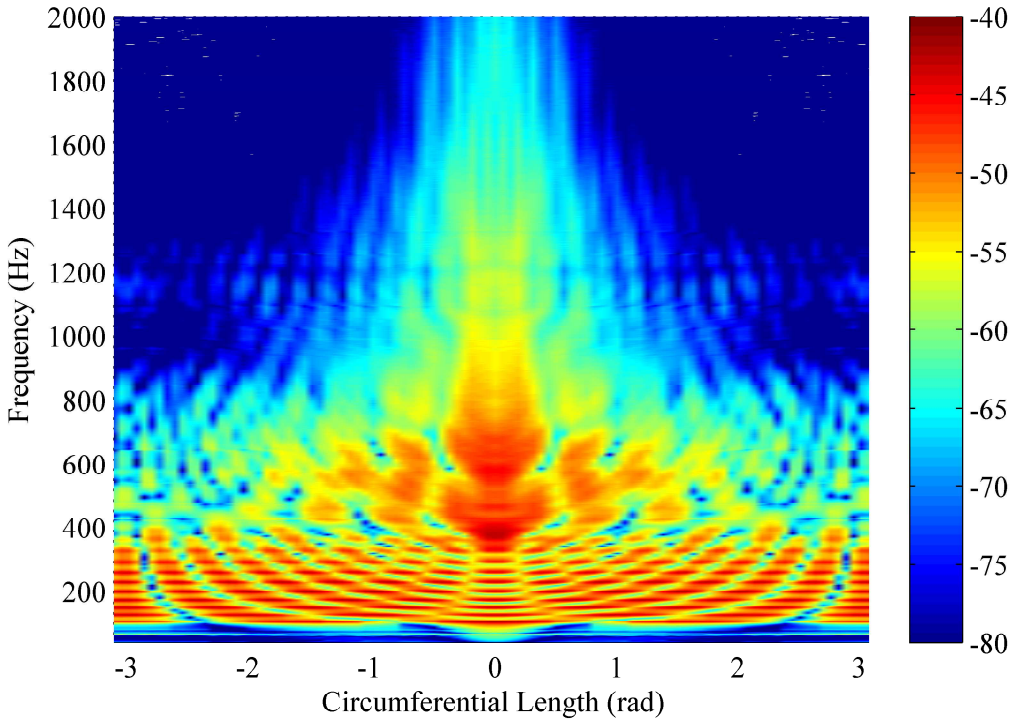

Figure B.1. Circumferential spectral plot for Tire 1.

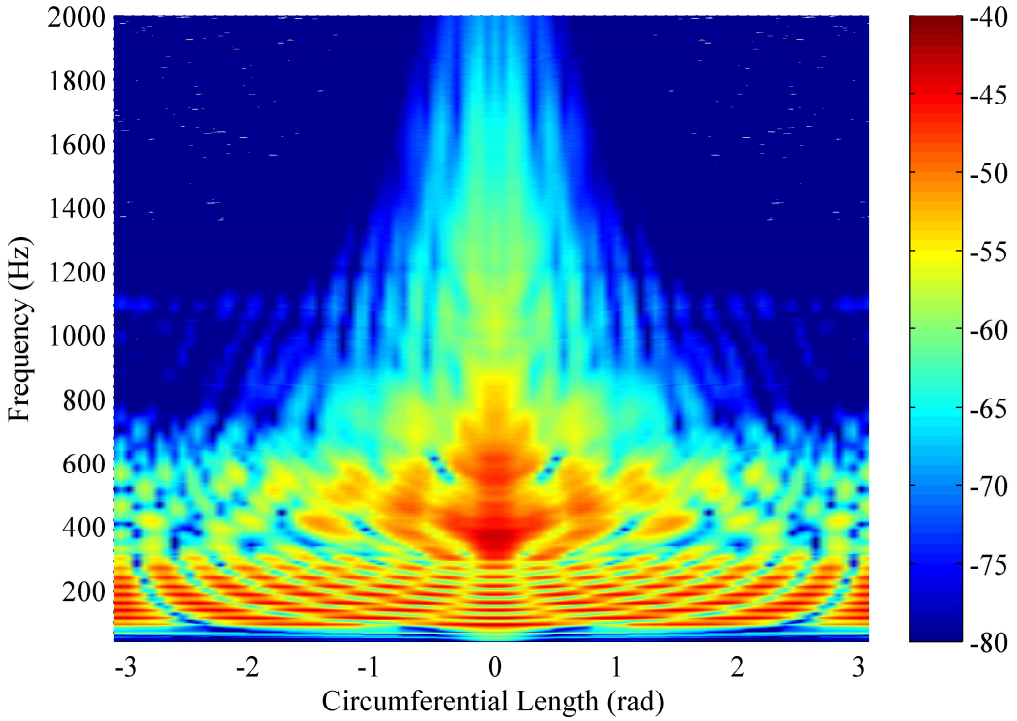

Figure B.2. Circumferential spectral plot for Tire 2.

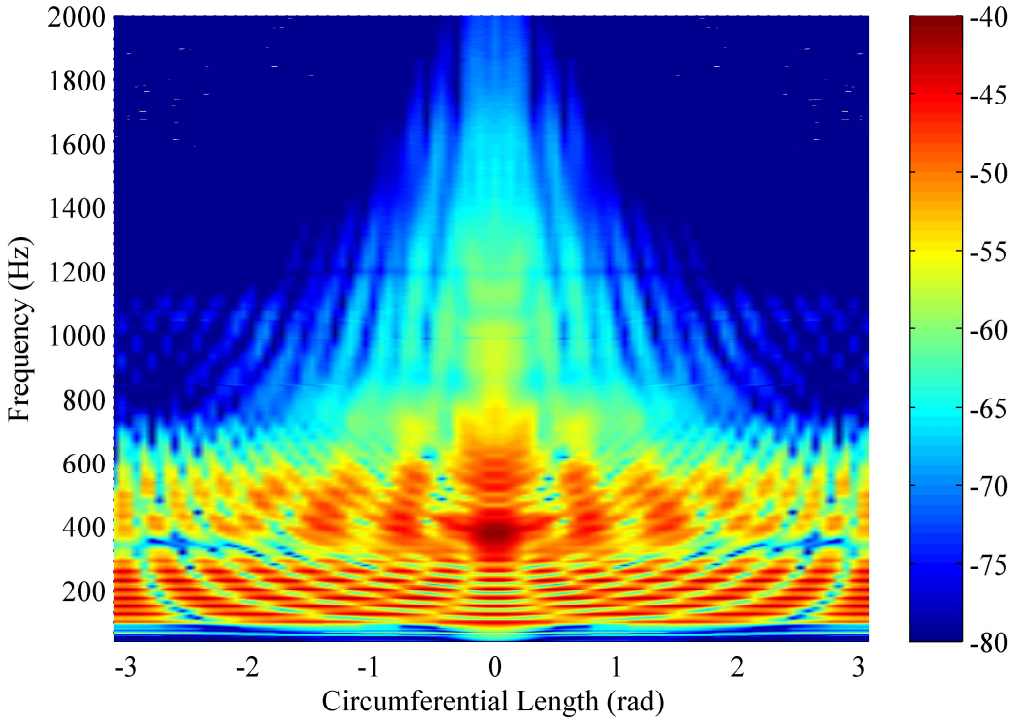

Figure B.3. Circumferential spectral plot for Tire 3.

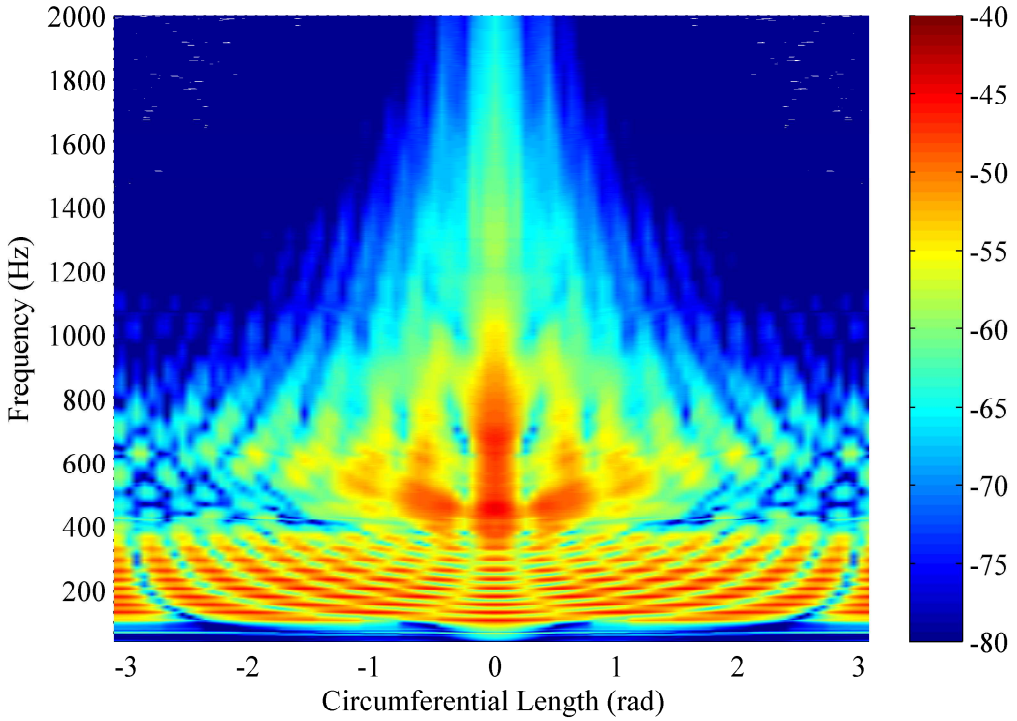

Figure B.4. Circumferential spectral plot for Tire 4.

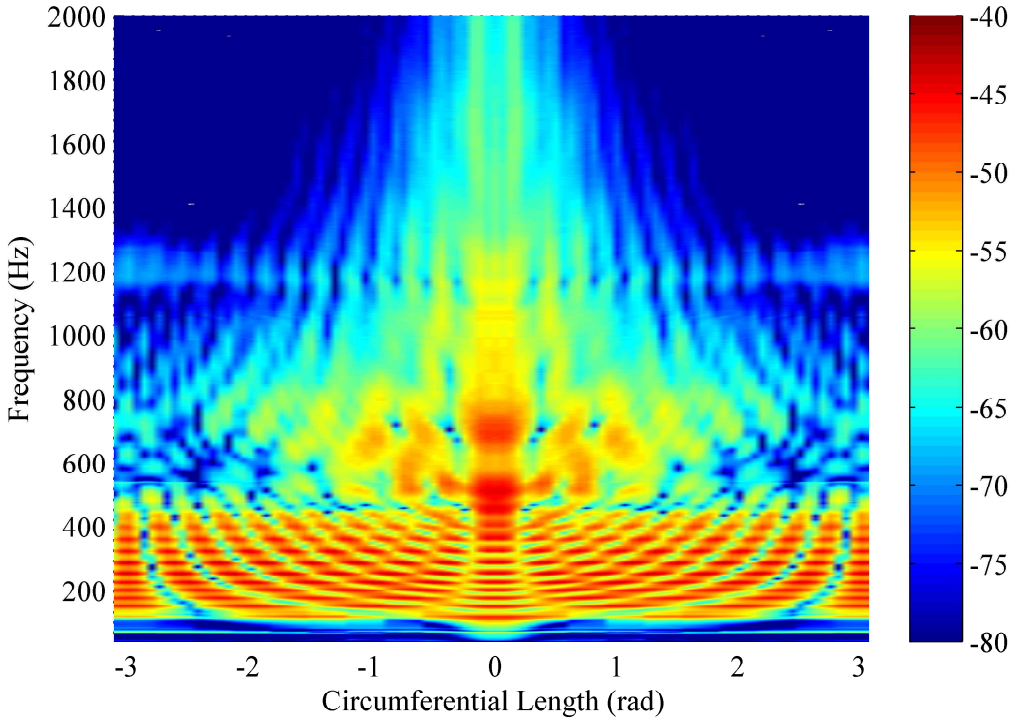

Figure B.5. Circumferential spectral plot for Tire 5.

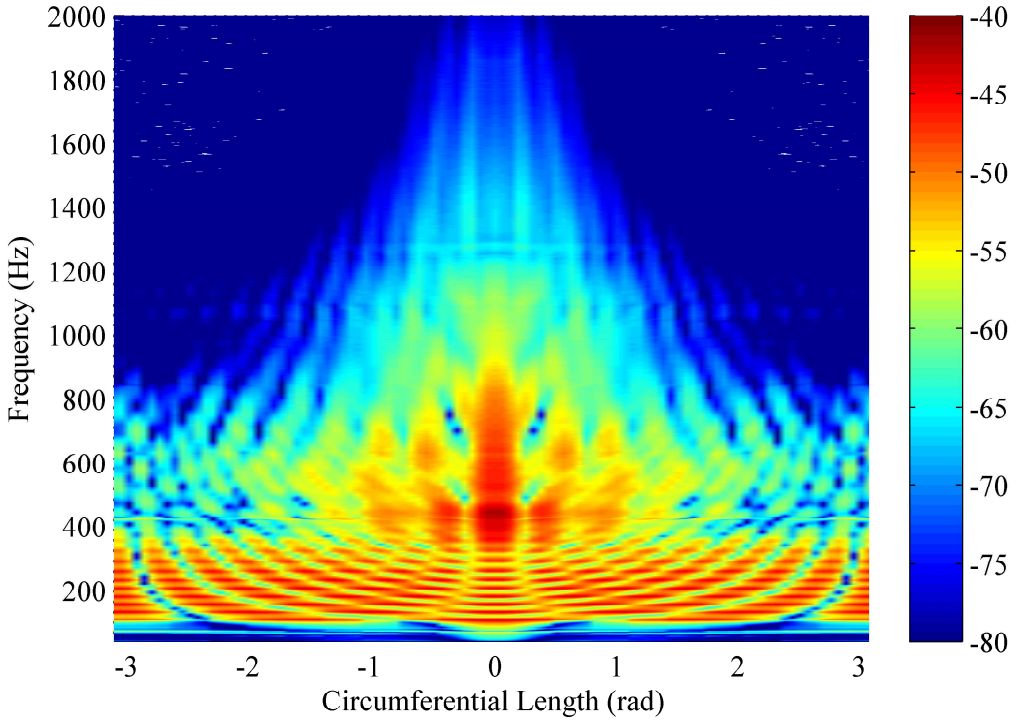

Figure B.6. Circumferential spectral plot for Tire 6.

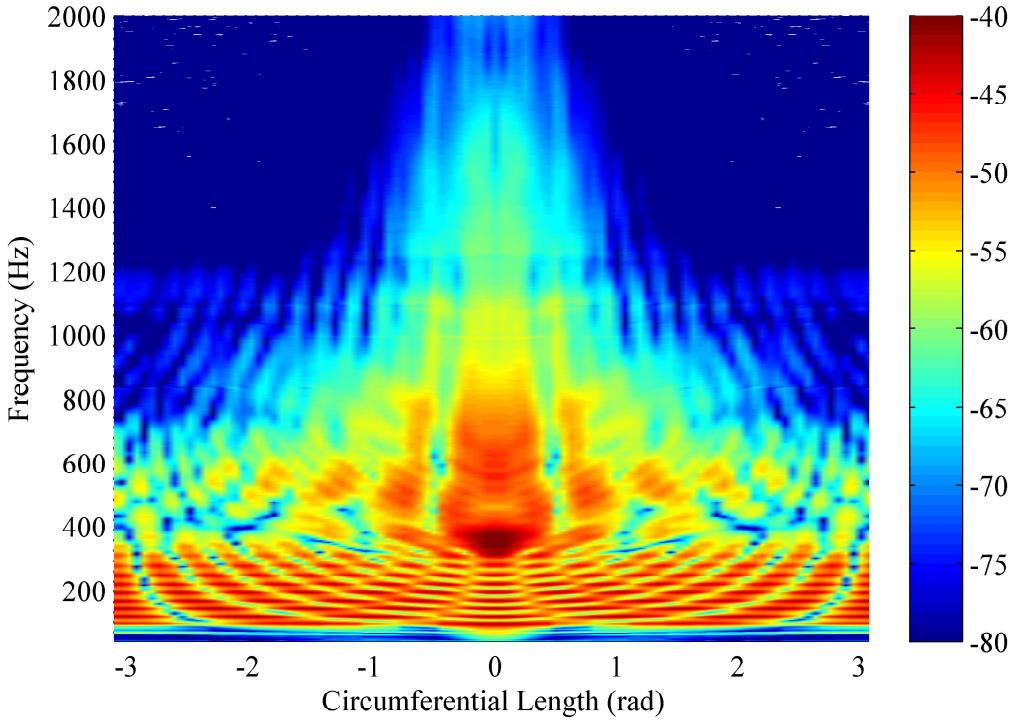

Figure B.7. Circumferential spectral plot for Tire 7.

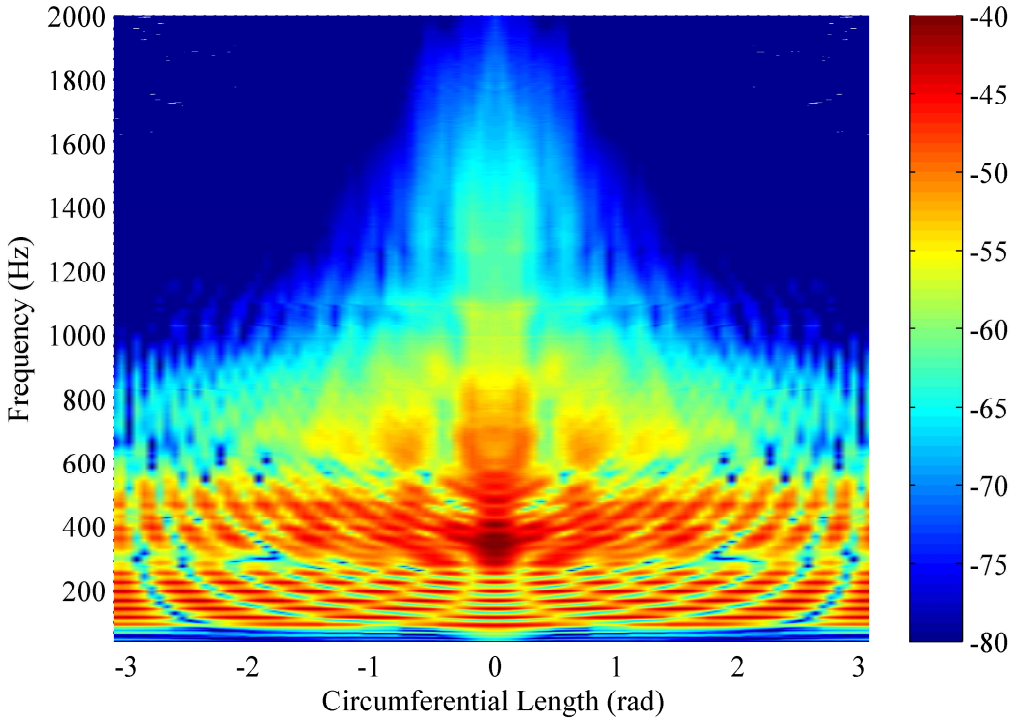

Figure B.8. Circumferential spectral plot for Tire 8.

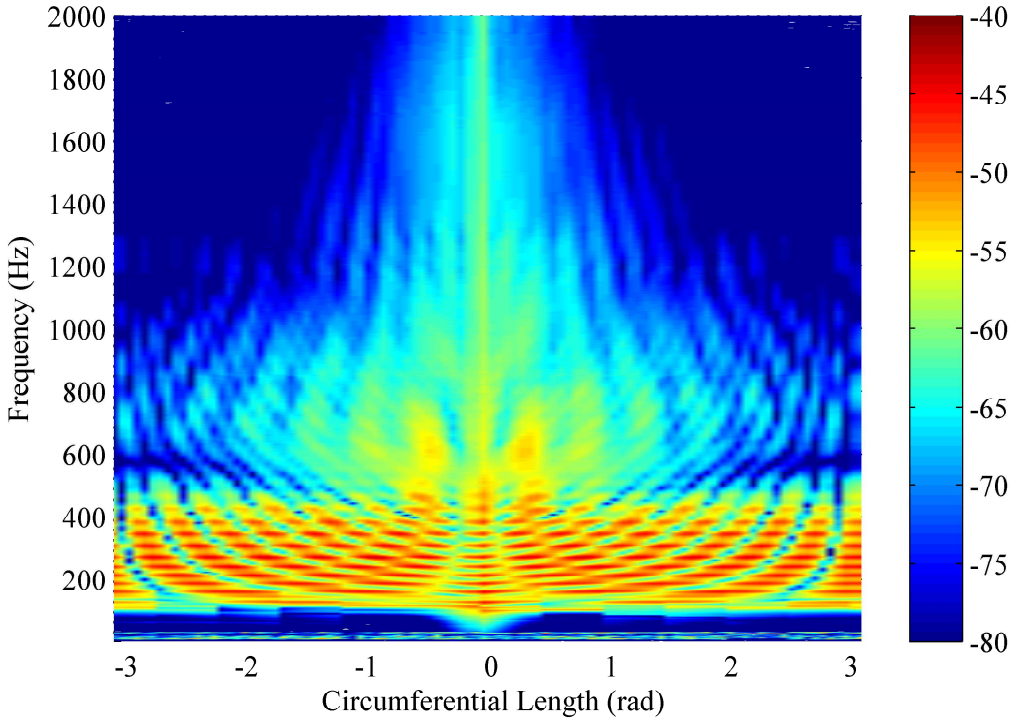

Figure B.9. Circumferential spectral plot for Tire 5 from patch excitation.

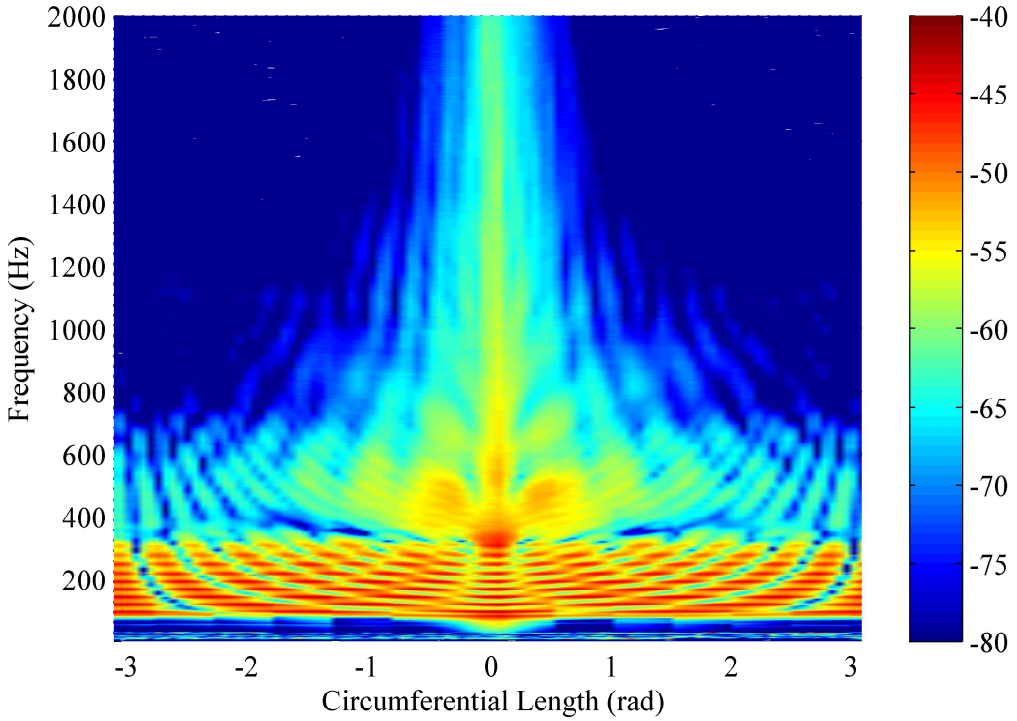

Figure B.10. Circumferential spectral plot for Tire 7 from patch excitation.

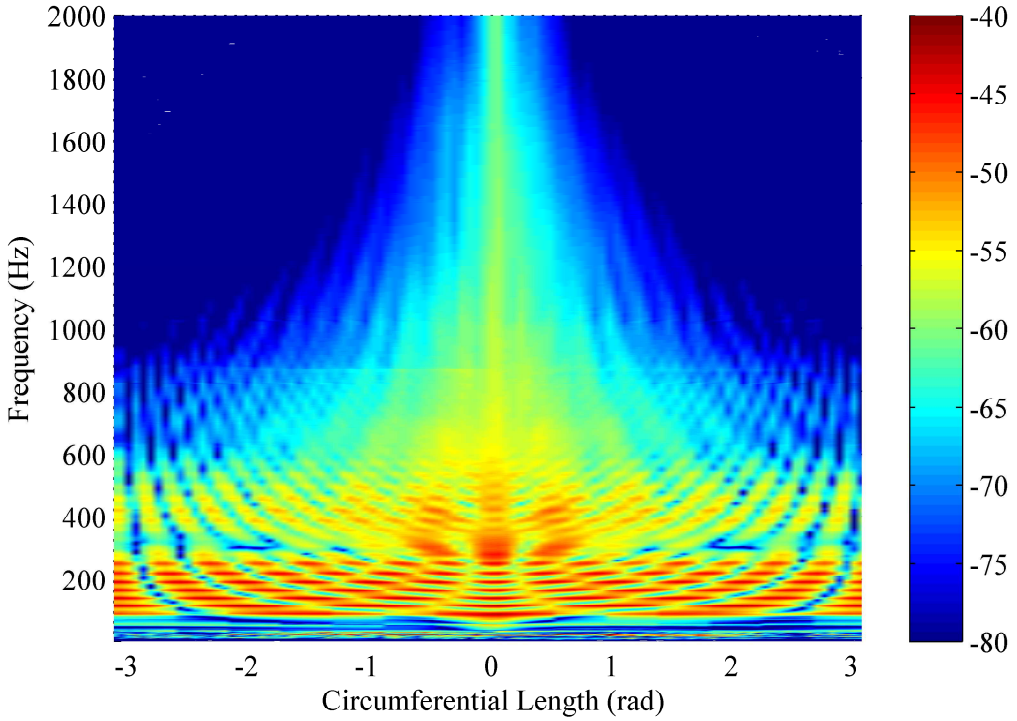

Figure B.11. Circumferential spectral plot for Tire 8 from patch excitation.

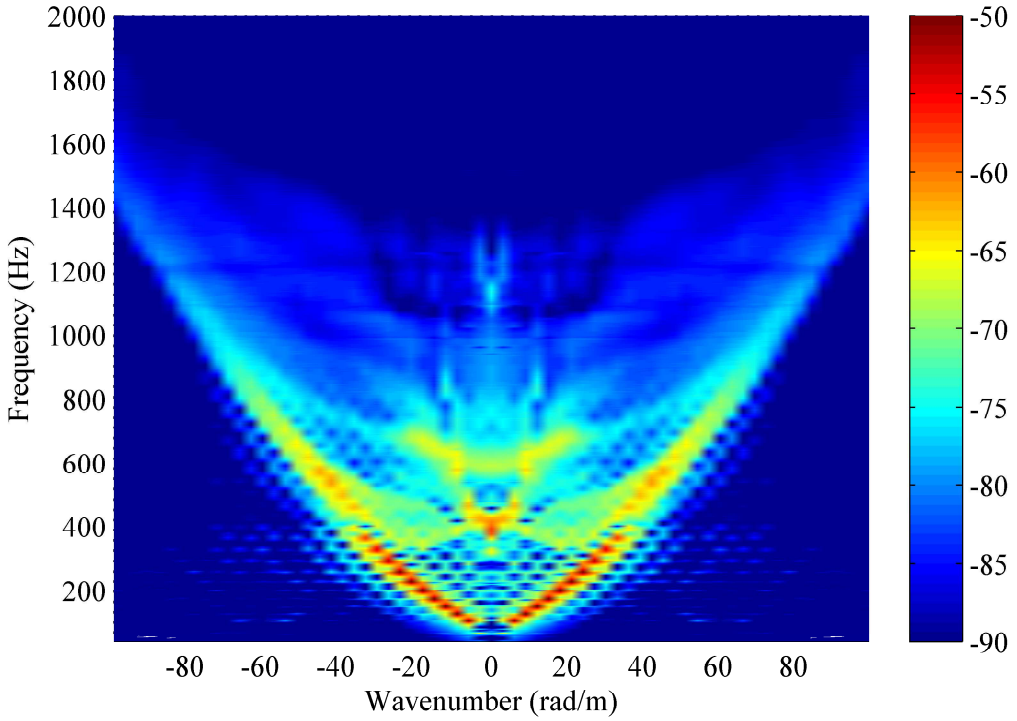

Figure B.12. Frequency-wavenumber plot for Tire 1.

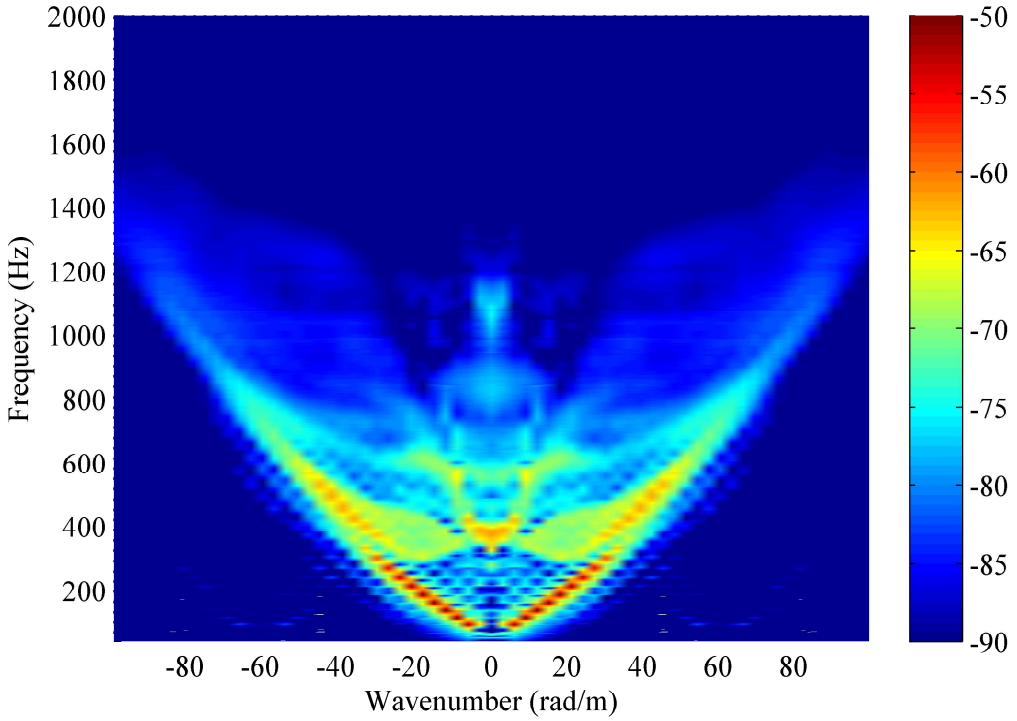

Figure B.13. Frequency-wavenumber plot for Tire 2.

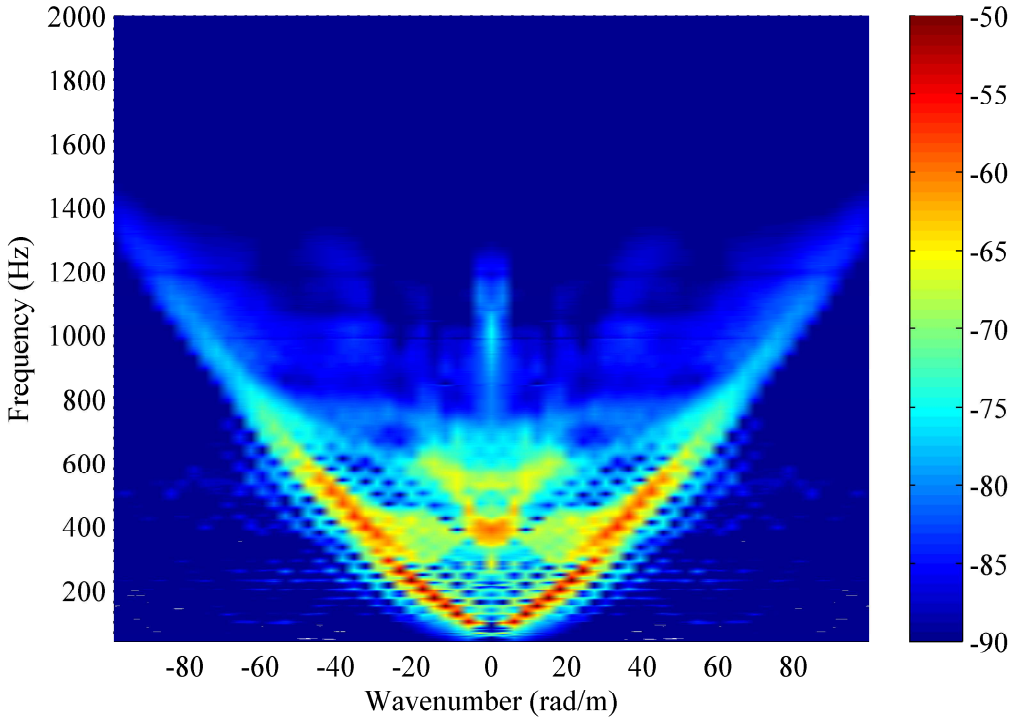

Figure B.14. Frequency-wavenumber plot for Tire 3.

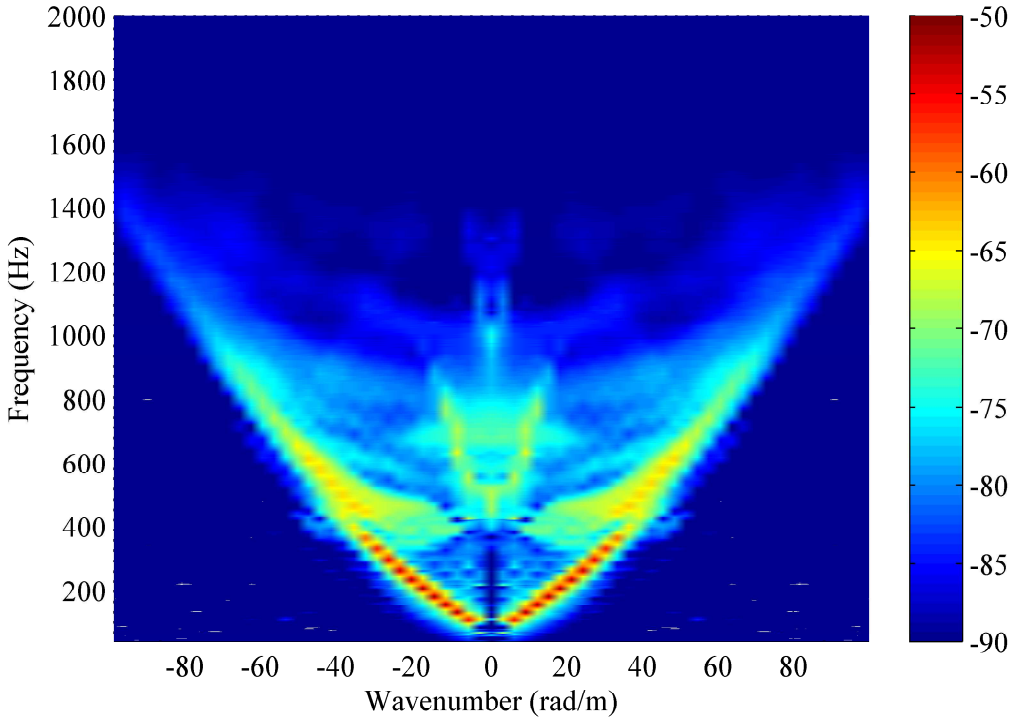

Figure B.15. Frequency-wavenumber plot for Tire 4.

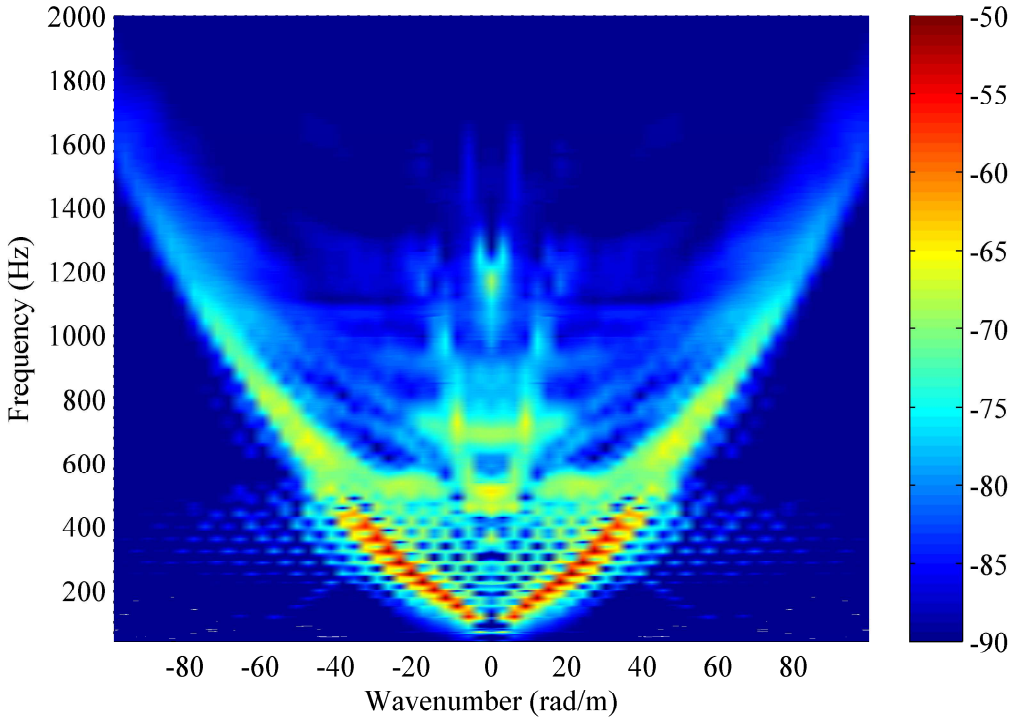

Figure B.16. Frequency-wavenumber plot for Tire 5.

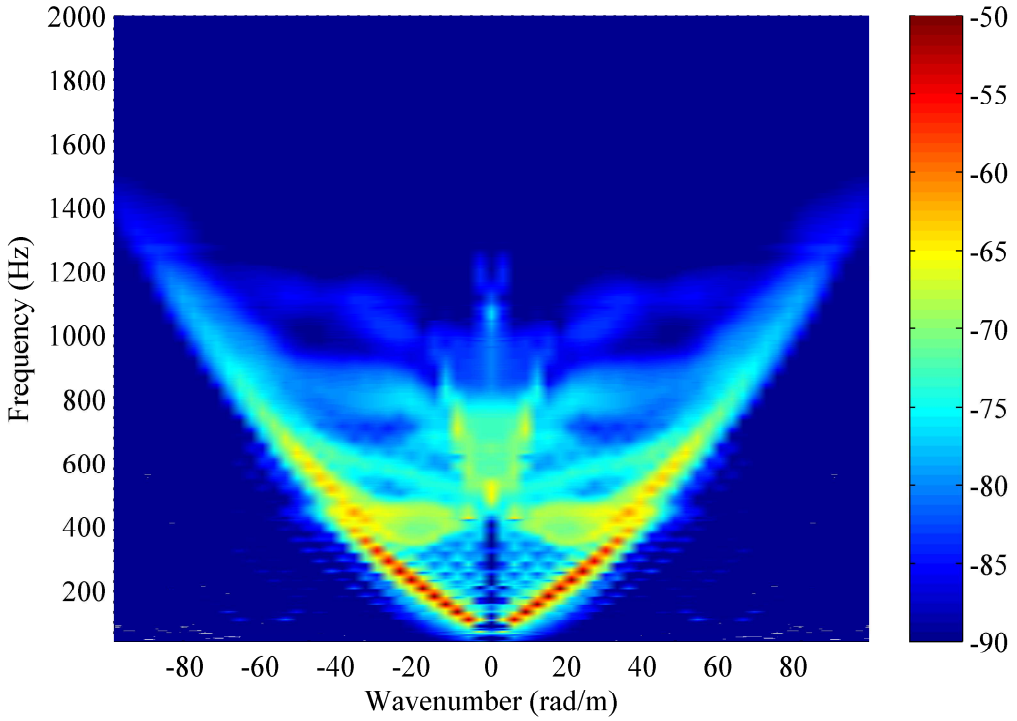

Figure B.17. Frequency-wavenumber plot for Tire 6.

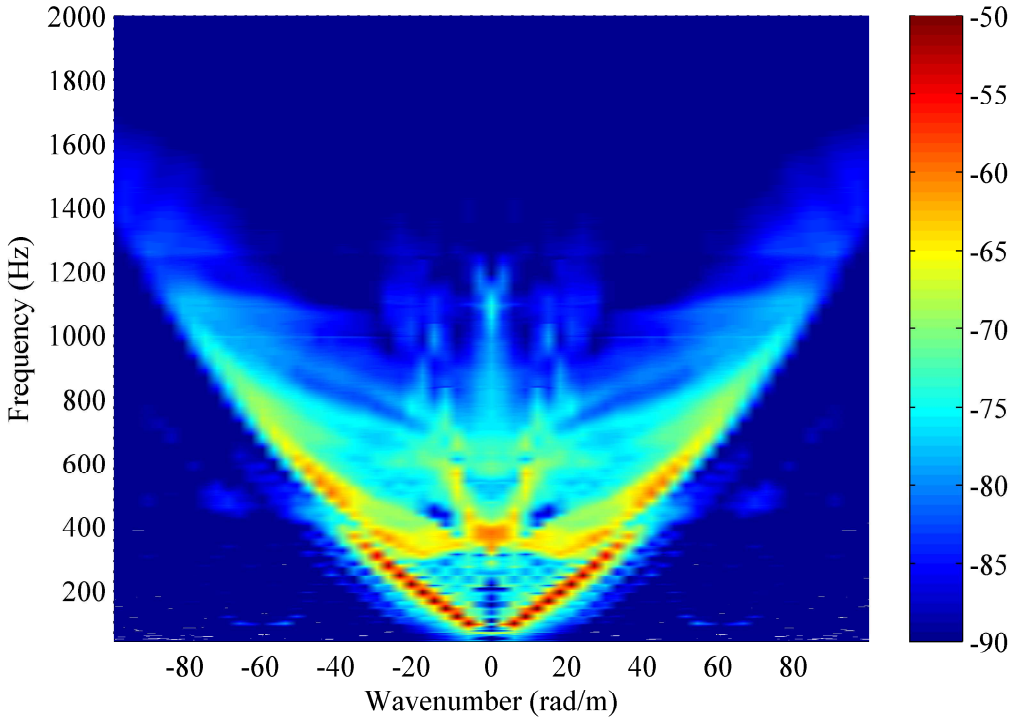

Figure B.18. Frequency-wavenumber plot for Tire 7.

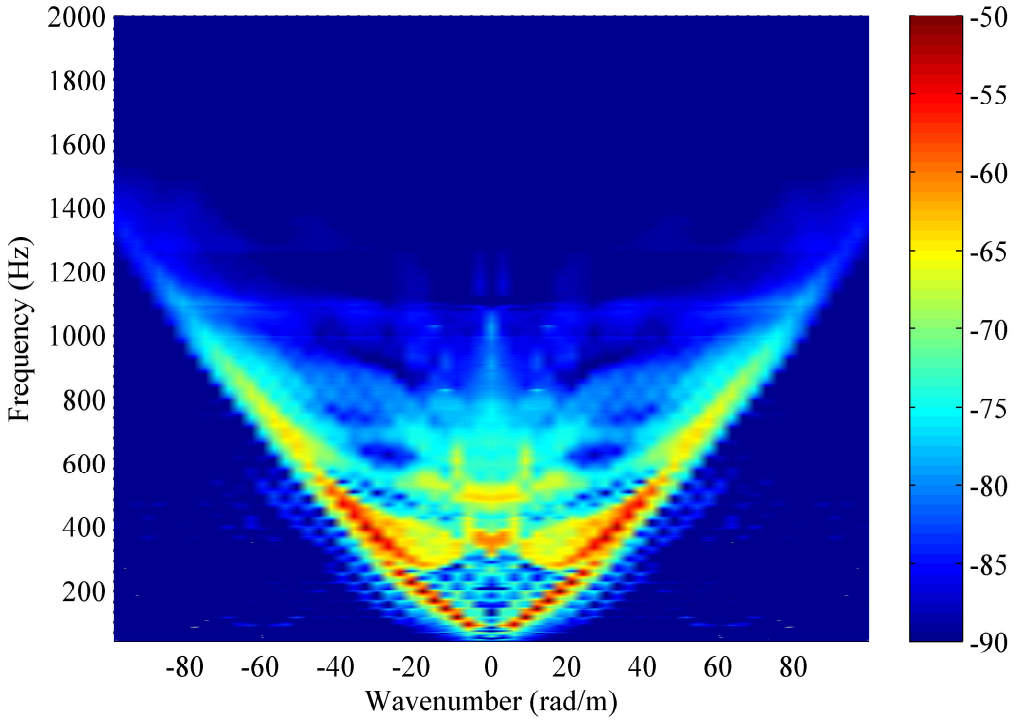

Figure B.19. Frequency-wavenumber plot for Tire 8.

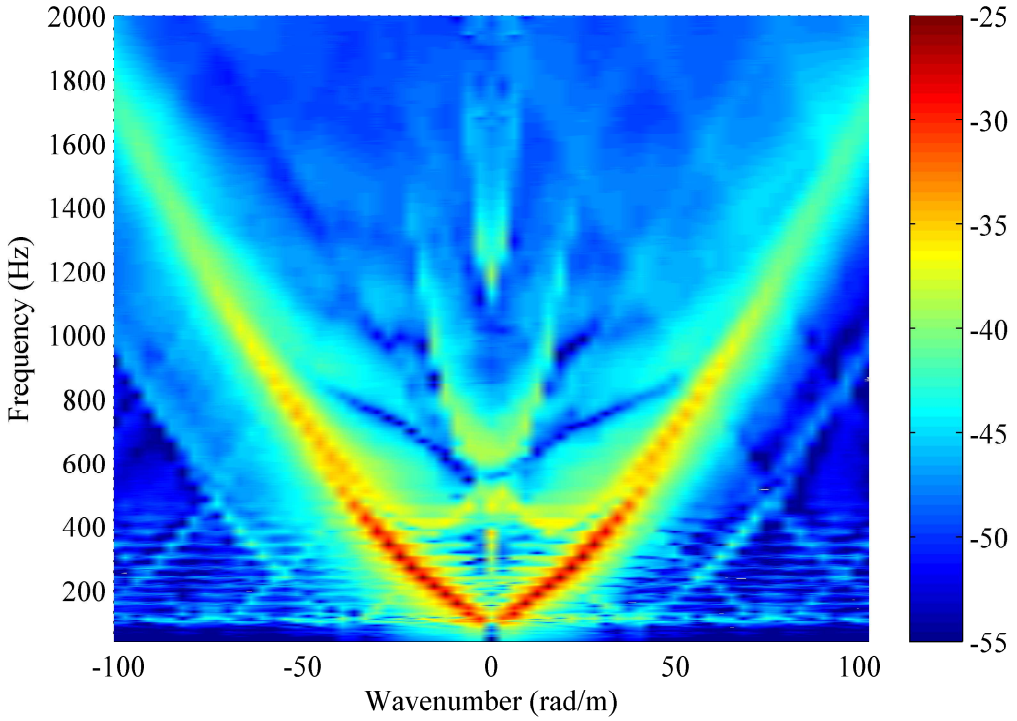

Figure B.20. Frequency-wavenumber plot for Tire 5 from patch excitation.

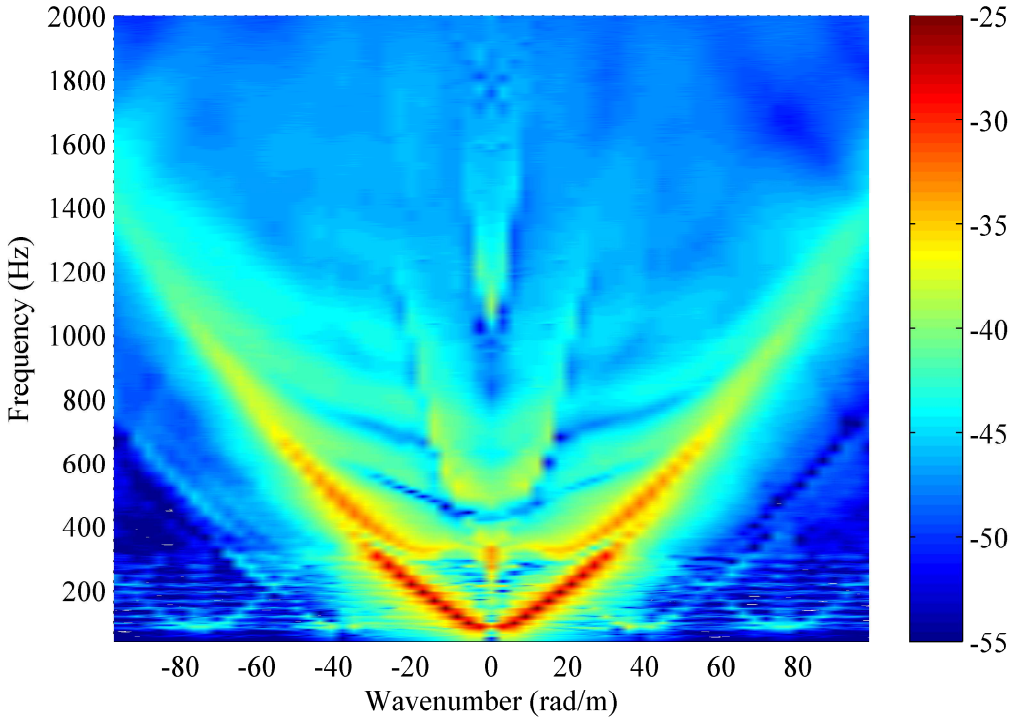

Figure B.21. Frequency-wavenumber plot for Tire 7 from patch excitation.

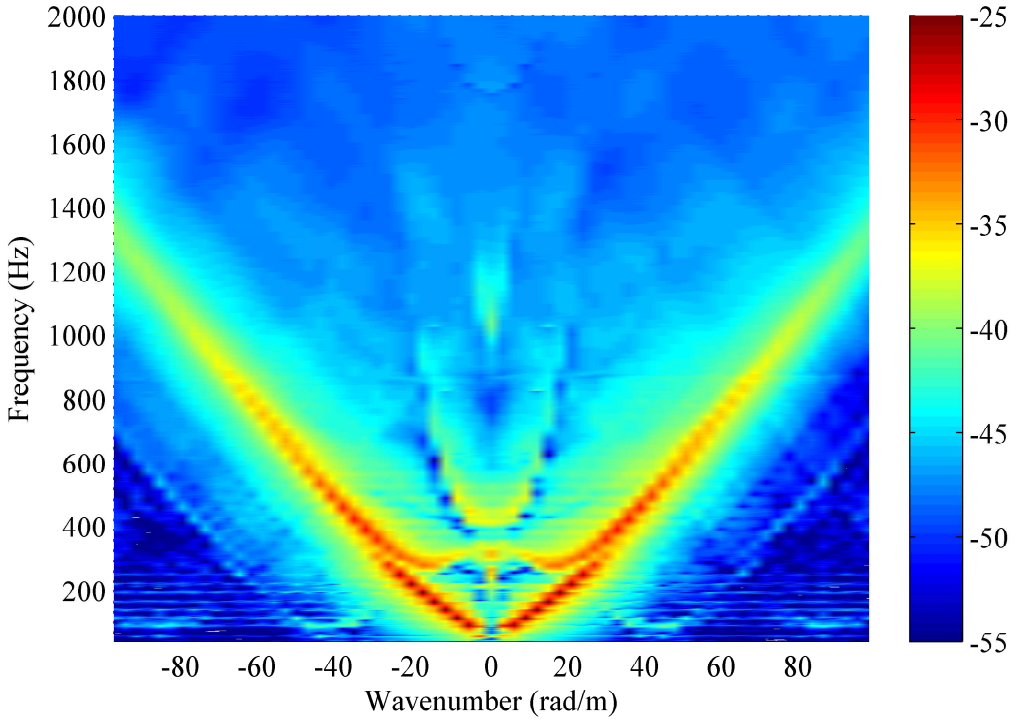

Figure B.22. Frequency-wavenumber plot for Tire 8 from patch excitation.

C. ADDITIONAL PLOTS: RELATIVE TIRE NOISE POTENTIAL MODEL

Table C.1. Tire A-weighted Airborne Noise Ranks.

Rank	Tire
1 (Loudest)	13
2	12
3	9
4	11
5 (Quietest)	10

Table C.2. Tire A-weighted Structure-borne Noise Ranks.

Rank	Tire
1 (Loudest)	13
2	12
3	11
4	10
5 (Quietest)	9

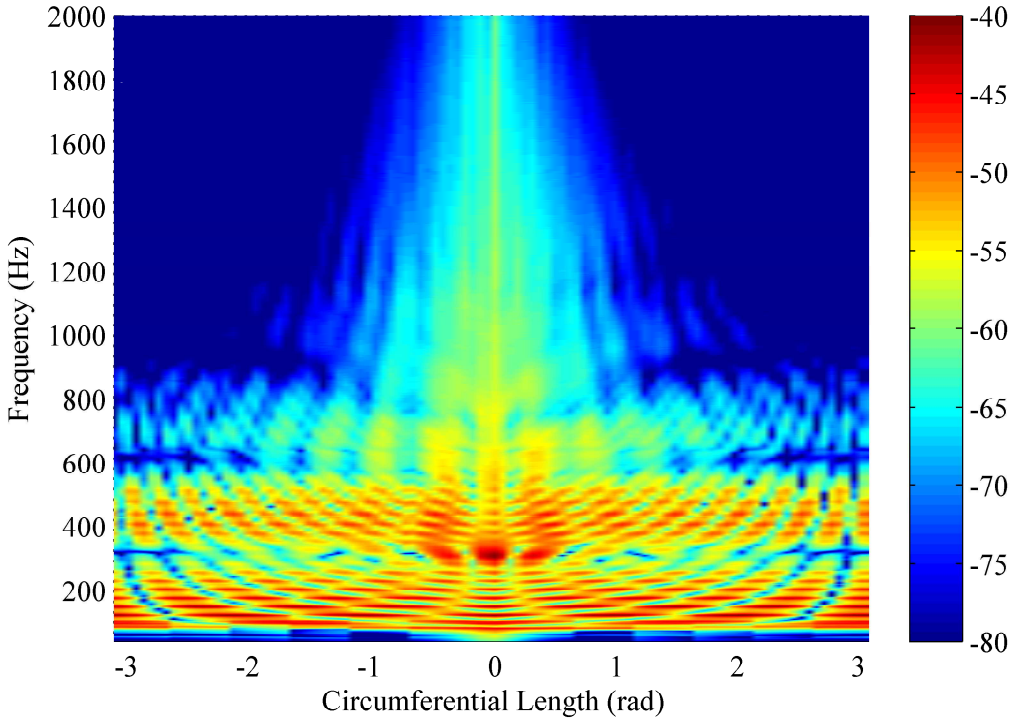

Figure C.1. Circumferential spectral plot for Tire 9.

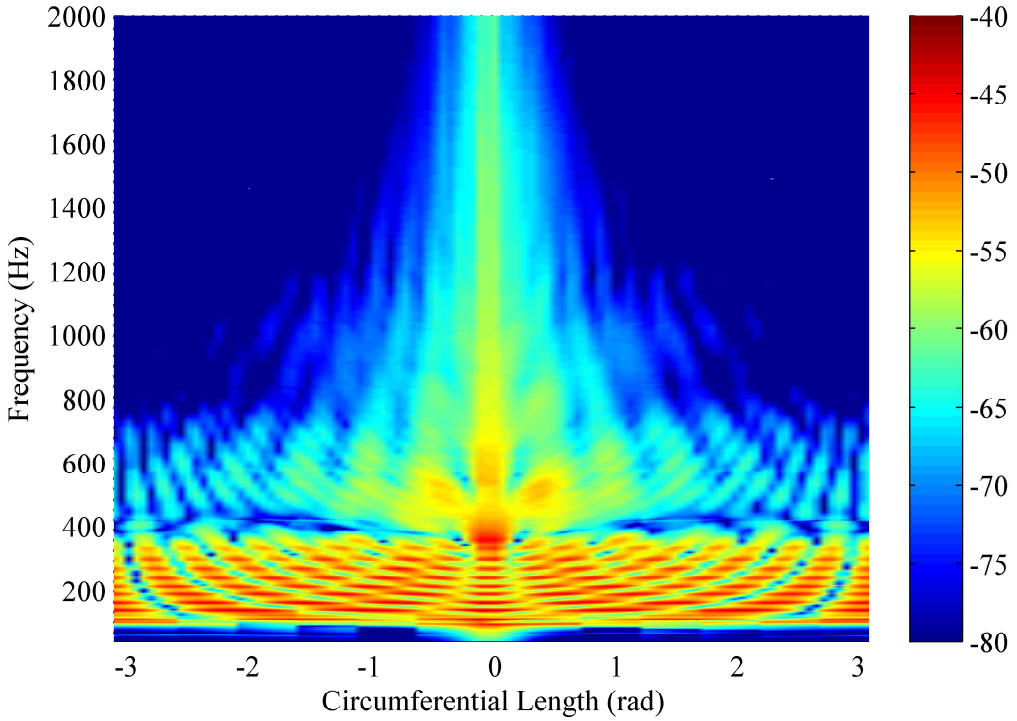

Figure C.2. Circumferential spectral plot for Tire 10.

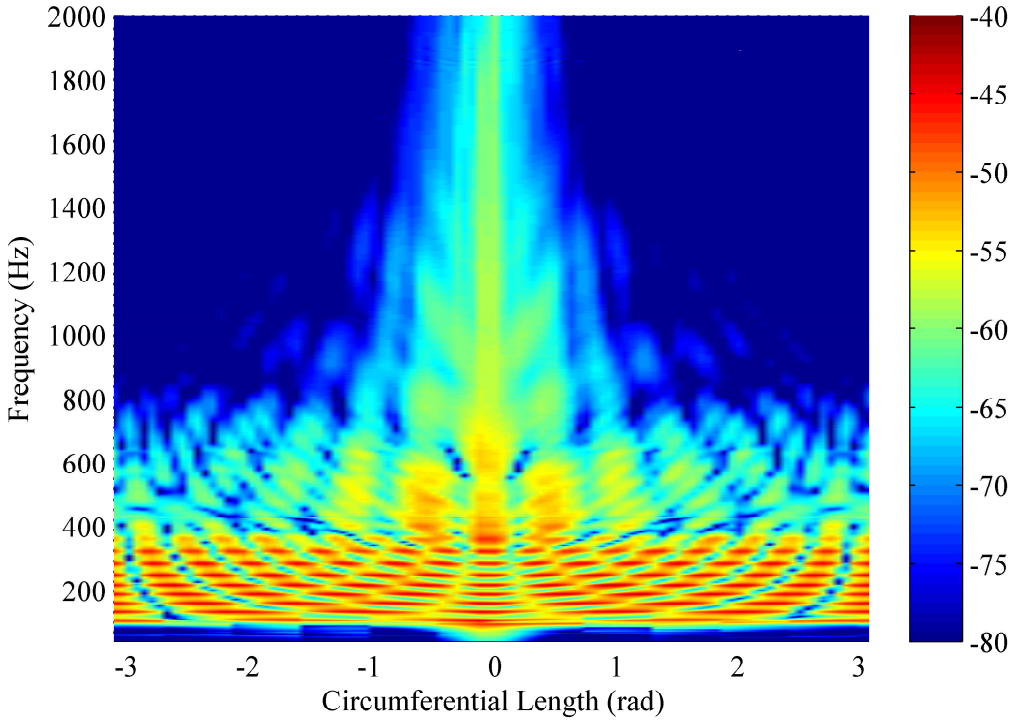

Figure C.3. Circumferential spectral plot for Tire 11.

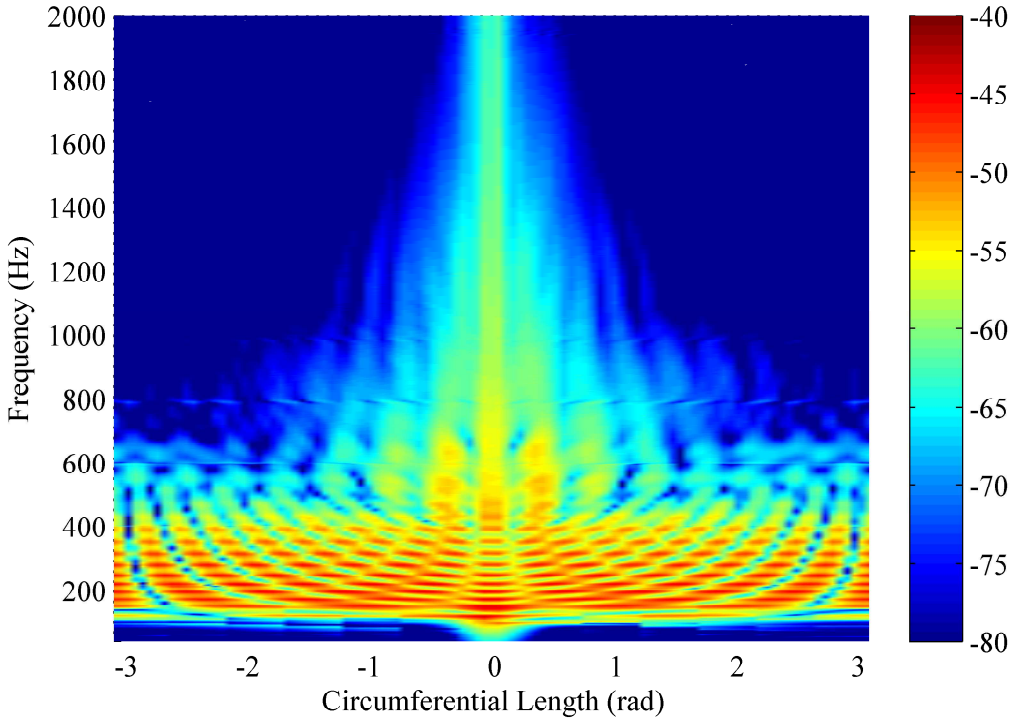

Figure C.4. Circumferential spectral plot for Tire 12.

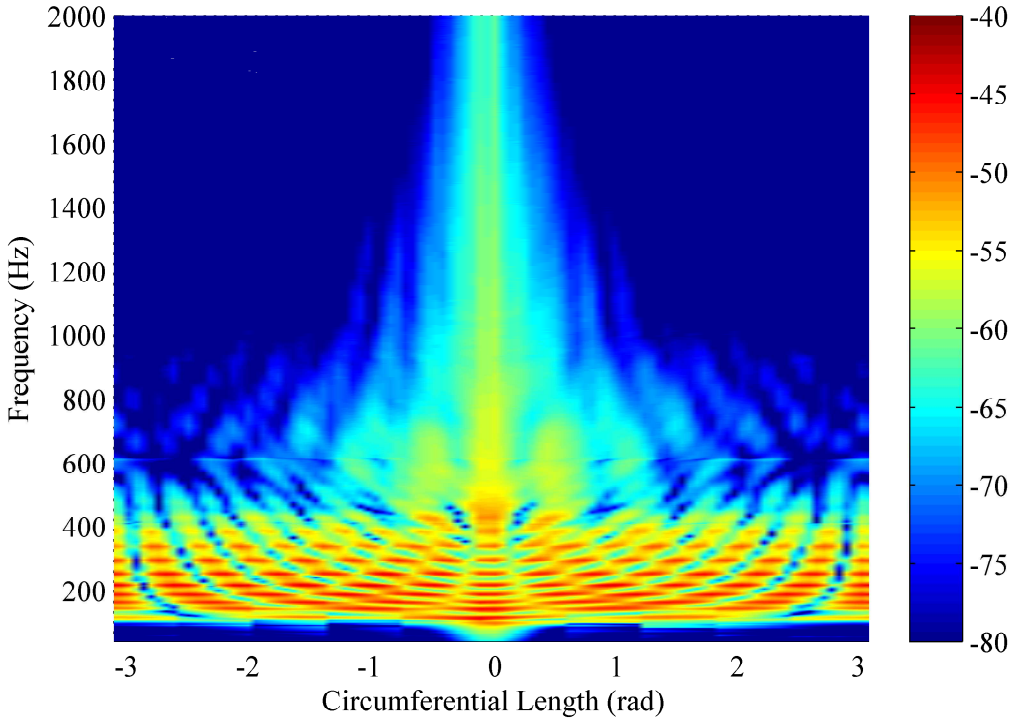

Figure C.5. Circumferential spectral plot for Tire 13.

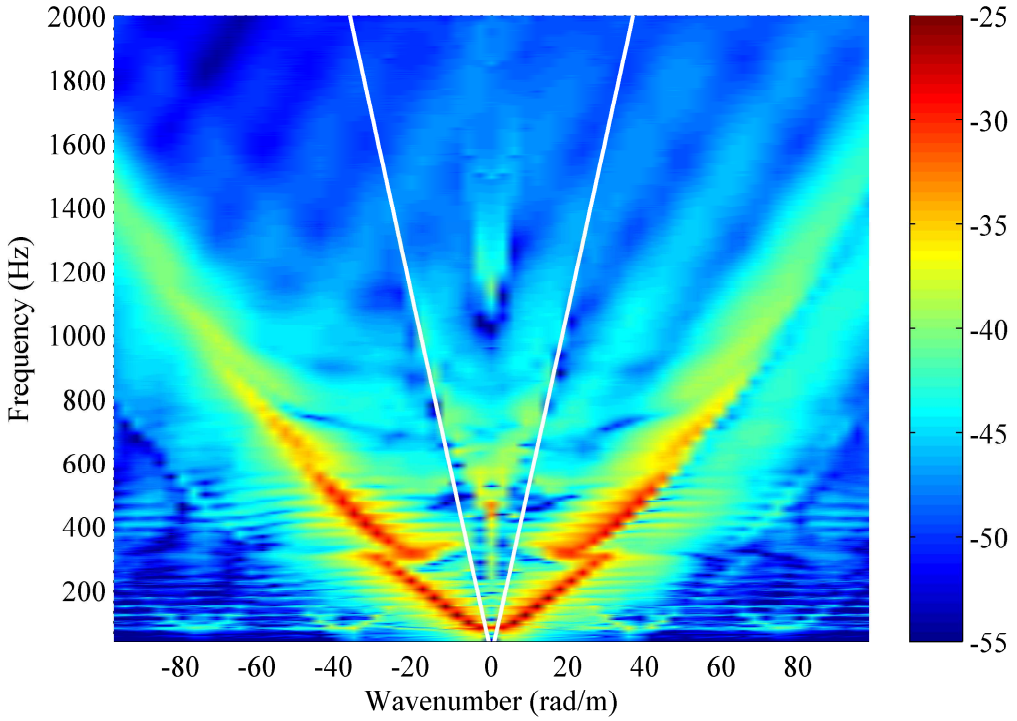

Figure C.6. Frequency-wavenumber plot for Tire 9.

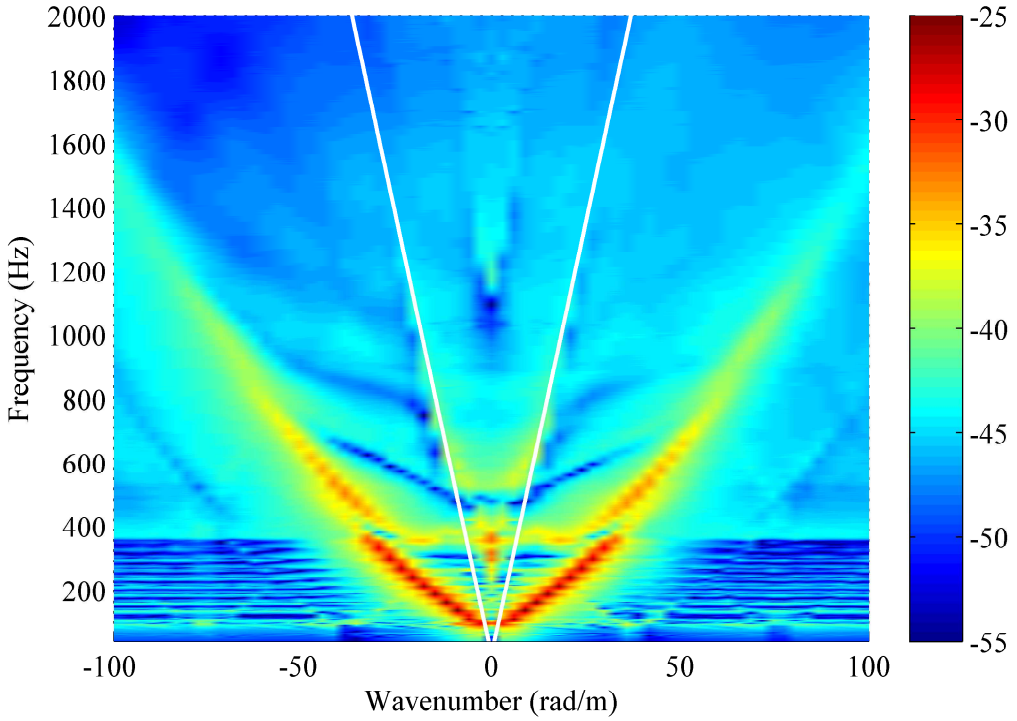

Figure C.7. Frequency-wavenumber plot for Tire 10.

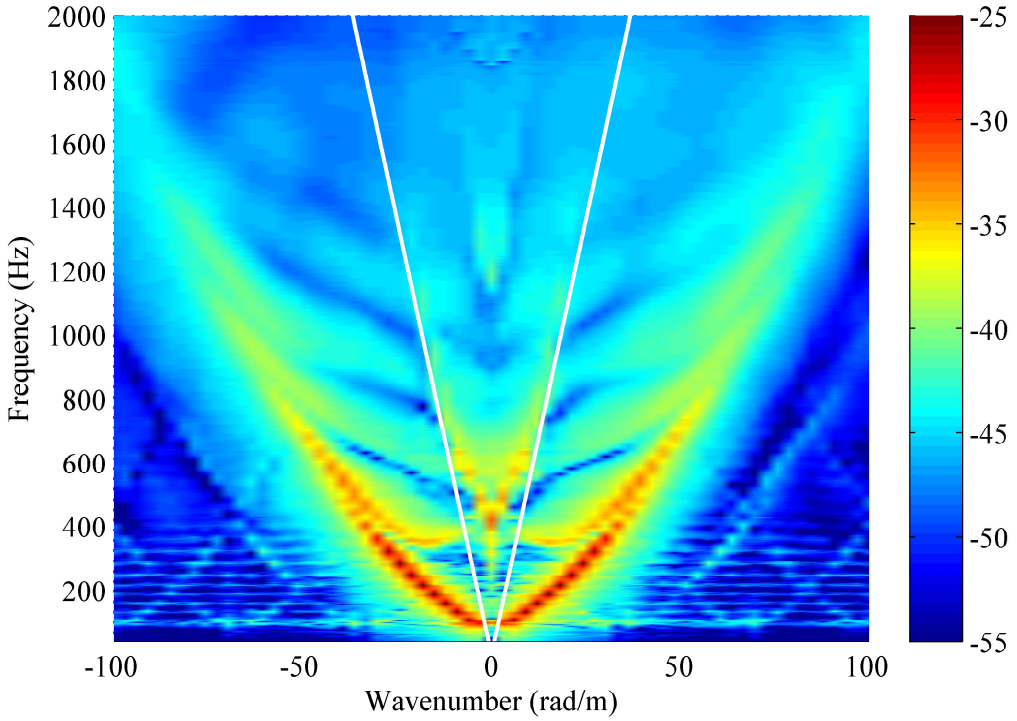

Figure C.8. Frequency-wavenumber plot for Tire 11.

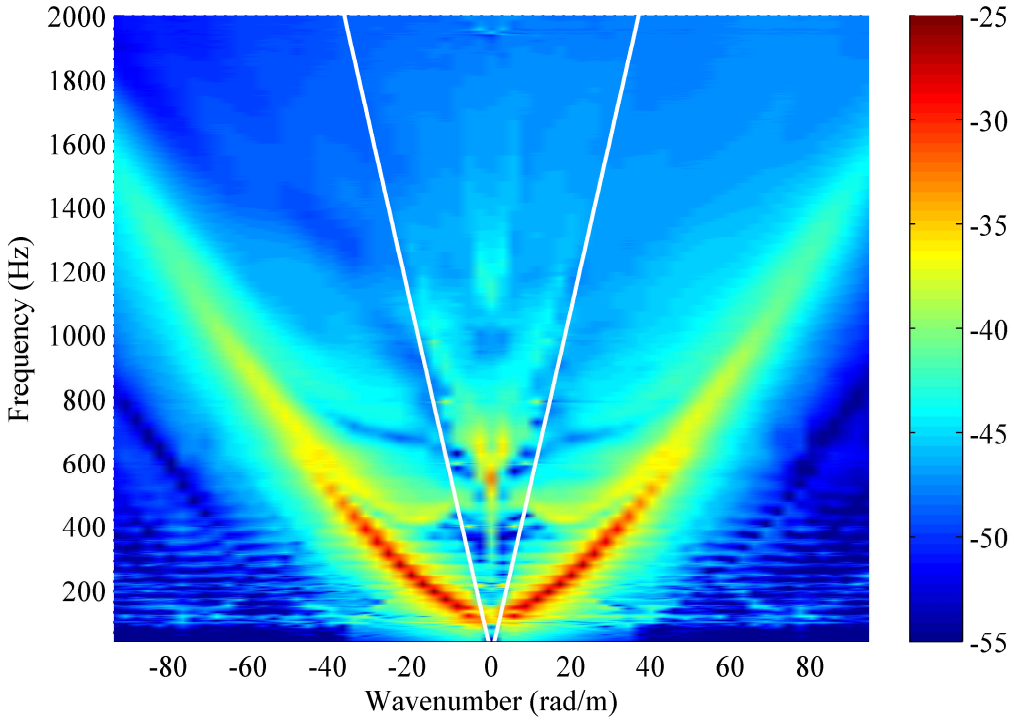

Figure C.9. Frequency-wavenumber plot for Tire 12.

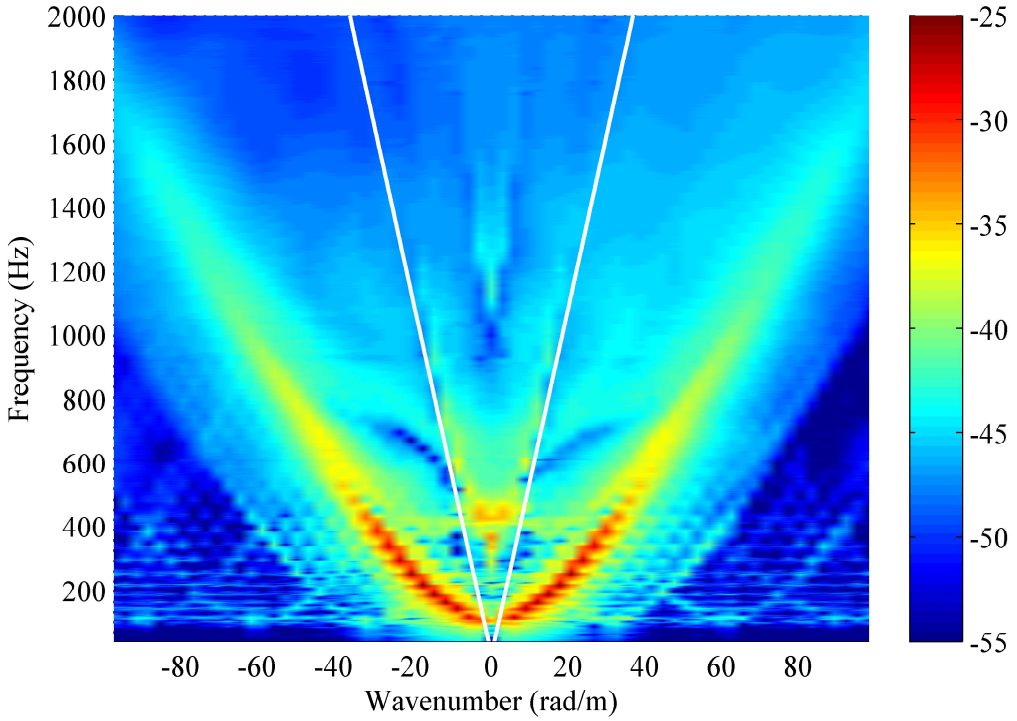

Figure C.10. Frequency-wavenumber plot for Tire 13.

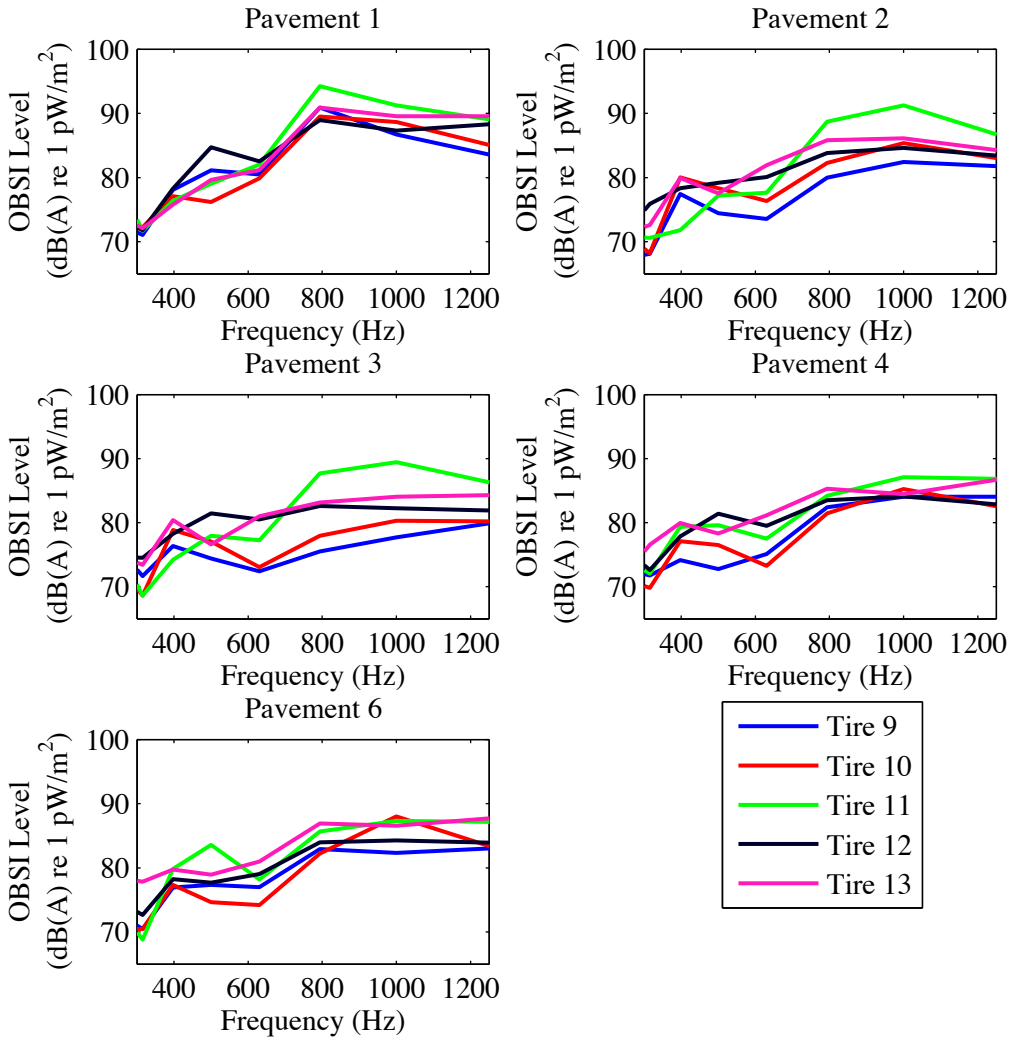

Figure C.11. Sound intensity level for each tire per pavement sample.

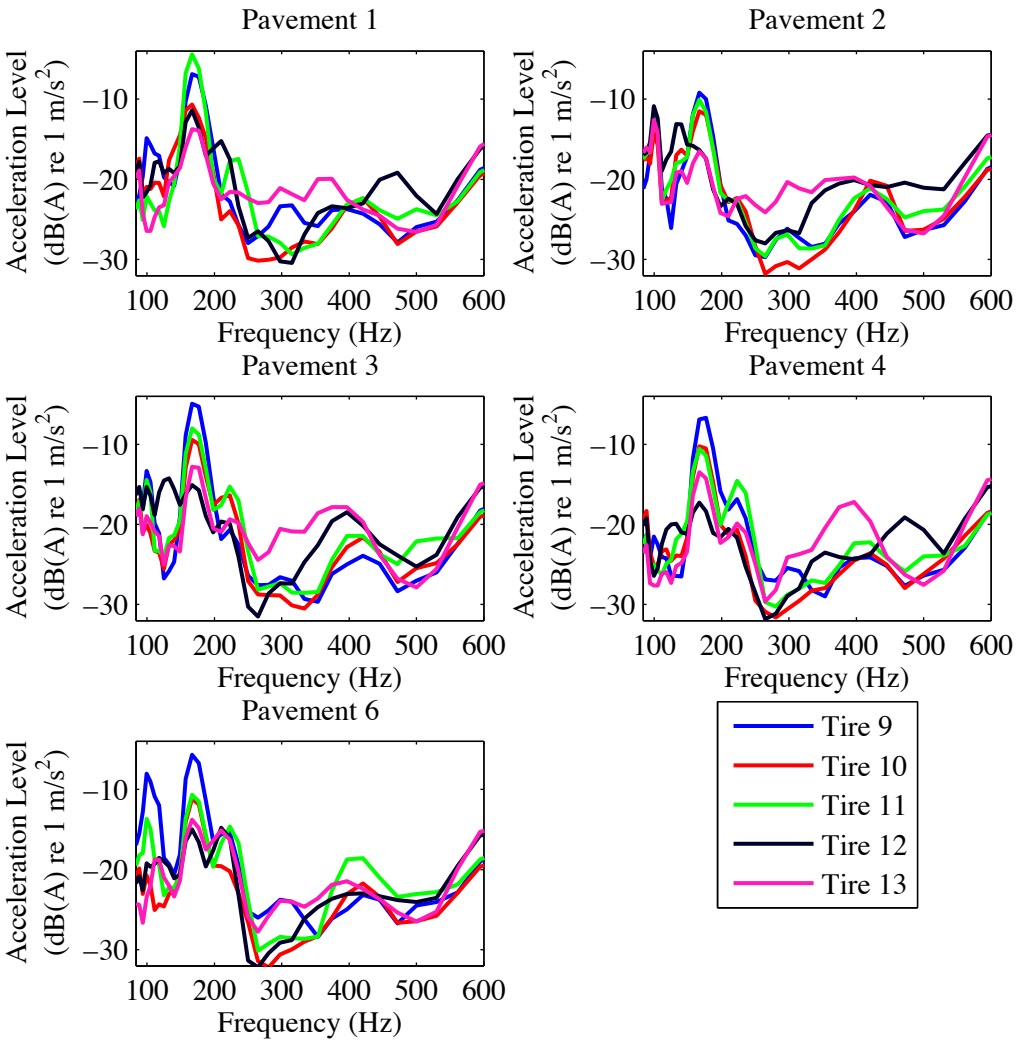

Figure C.12. Acceleration in the tire's direction of travel (X-axis) recorded for each tire per pavement.

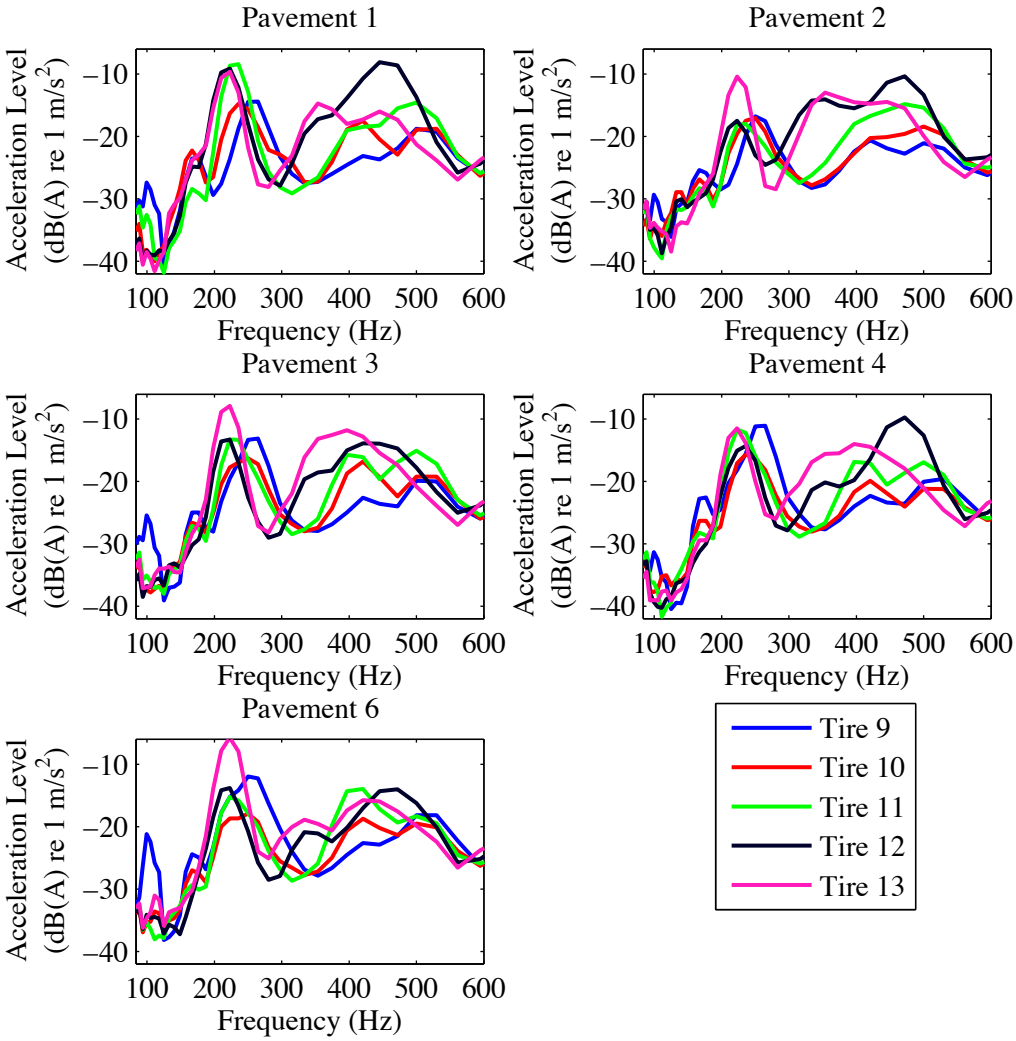

Figure C.13. Out-of-plane acceleration (Y-axis) recorded for each tire per pavement.

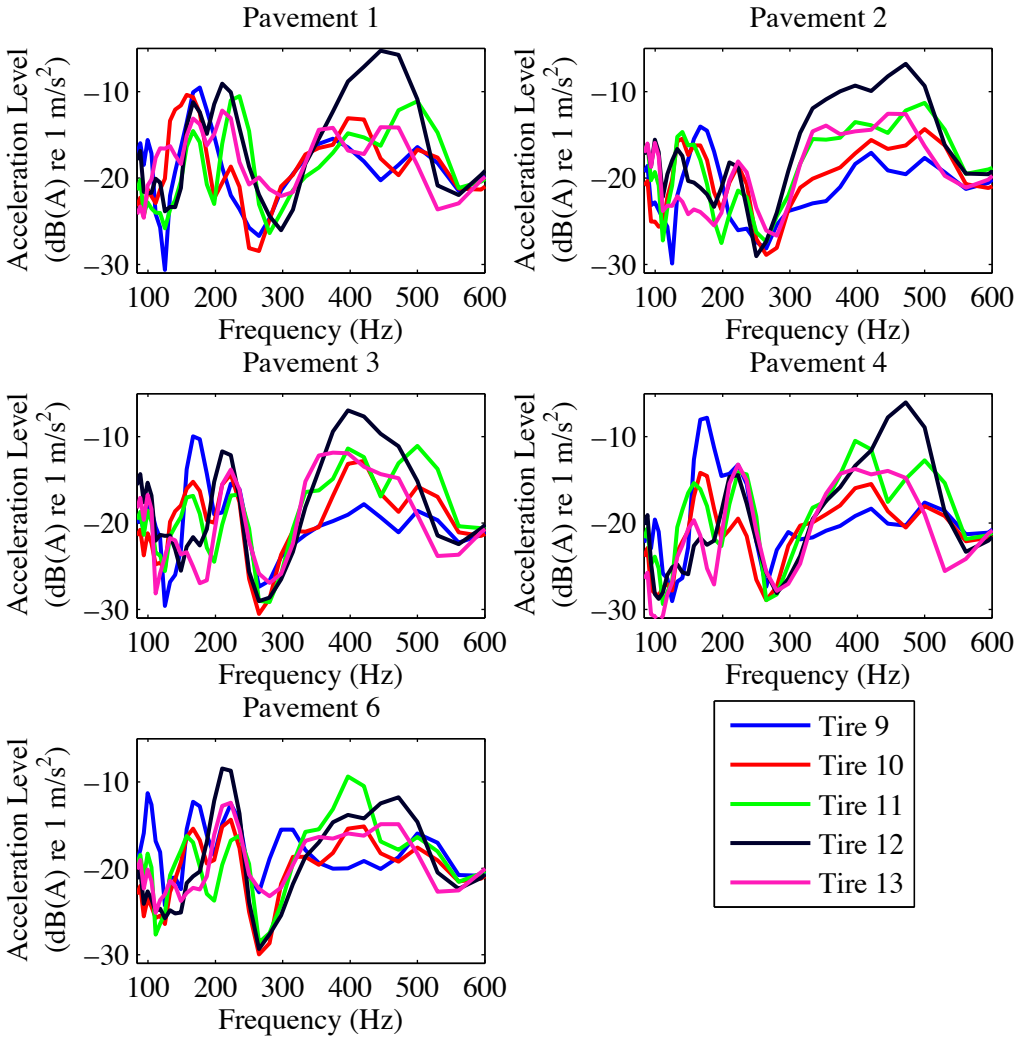

Figure C.14. Normal acceleration (Z-axis) recorded for each tire per pavement.

VITA

VITA

I was raised in Mission Viejo, CA and attended Mission Viejo High School. In 2009, I graduated from California State Polytechnic University of Pomona with a Bachelor of Science in Mechanical Engineering. For three years, I worked at a window and door manufacturer designing and testing high-end fenestration products. In 2012, I came to Purdue University and have studied acoustics, materials, and vibrations. I was awarded the National Science Foundation East Asia and Pacific Summer Institutes for U.S. Graduate Students fellowship in 2013 and spent 10 weeks studying the Finite Difference Time-Domain method at Kansai University in Osaka, Japan.